openNIRS Documentation

www.openNIRS.org
info@openNIRS.org

M.Sc. A. von Lühmann

This file is an unaltered excerpt of the Master's Thesis "'Design and Evaluation of a System for Mobile Brain Activity Measurements using Functional Near-Infrared Spectroscopy"' by A. von Lühmann, Institute of Biomedical Engineering (Supervisor: Prof. Olaf Dössel) Cognitive Systems Lab (Supervisors: Prof. Tanja Schultz, Dipl. Inf C. Herrf, D. Heger), Karlsruhe Institute of Technology, 2014.

Contents

1

Introduction

At the outset of this thesis, a brief introduction to functional Near-Infrared Spectroscopy and its advantages will be given for motivation and an objective will be formulated.

1.1 Motivation

Functional Near-Infrared Spectroscopy (fNIRS) is a relatively new technology pioneered by Jöbsis in 1977 [1] that allows non-invasive and continuous measurement of cerebral oxygenation levels using near-infrared light.
The possibility of retrieving spatial functional information of the brain while using non-invasive, comparatively low-cost, compact and hazard-free technology motivated an increasing number of researchers to further investigate the technical as well as the physiological aspects of fNIRS. After Jöbsis' proof of concept, research in the late 1980s and in the 1990s focused on enhancing the understanding of the physiology of the signal, NIRS instrumentation and mathematical concepts. In 1988, Delpy et al. provided a mathematical way to relate the measured NIRS signal to relative oxygenation levels by taking light scattering into account [2]. After this, several NIRS instruments were built with the aim to enhance instrumentation and find ways to obtain absolute oxygenation values [3–6]. In 1993, four research groups independently demonstrated the feasibility of non-invasive brain activity investigation using fNIRS [7–10], followed by an increase of publications using NIRS technology for brain activity studies. From the 2000s until today, the next major step was the design of imaging instruments for brain activity mapping from topographic information: functional Near-Infrared Imaging (fNIRI).
Today, fNIRS and fNIRI have entered neuroscience as a research tool and it has been shown that they are reliable and trustworthy for research based on investigating groups of subjects [11]. This research into NIR based brain activity monitoring is motivated by several potentials as an alternative or addition to functional Magnetic Resonance Imaging (fMRI) and Positron Emission Tomography (PET):

- fNIRS provides (complementary) information about physiological parameters that are not available in other modalities, e.g. oxygenation information [12] or cytochrome oxidase as marker of metabolic demands [13]
- fNIRS has a higher temporal resolution than both fMRI and PET.
- The equipment is low-cost, small, bed-side applicable, can be made portable and is in general less restraining and therefore

- makes it possible to conduct brain activation studies in clinical offices and under more realistic conditions and is usable for subjects who cannot use fMRI, e.g. are not able to stay sufficiently still [14].
- The equipment can easily be combined with other modalities such as EEG [15].
- fNIRS is electrically isolated and non-ionizing and therefore does not limit the number of scans one can undergo [13].
- fNIRS is robust to motion artifacts.

Other than offering potentially complementary information and new areas of application compared to fMRI and PET, fNIRS seems to be a promising alternative or multimodal expansion to EEG-based Brain Computer Interfaces (BCI) [12, 16–19] with the advantage of being much less sensitive or non-sensitive at all to electrical artifacts in the body.

The increasing interest in fNIRS technology led to the design of several instruments from research groups and first commercial devices on the market. While most of the instruments are static and tabletops, old devices mostly using lasers, high-voltage photo-amplifiers and optical fibers for signal transmission, new technology has become available that allows the instruments to become more compact, safe and even mobile.
Only very few of the devices in up-to-date publications are truly mobile in the sense of being completely worn on the body, enabling free movement. Furthermore, an often reported issue that seems not to be resolved satisfactorily so far is the optode attachment to the head guaranteeing both stable optical contact, sufficient light levels and comfortable wearing [13, 20] as the stable fixation of optodes to the head is one major limitation on accuracy [21].

1.2 Objective

The aim of this work is the design and evaluation of a compact, modular, fully mobile (wireless) multichannel functional Near-Infrared Spectroscopy system for brain activation studies in the field of brain computer interfaces.
At the same time, a mechanical design for optode attachment and system housing is to be designed that allows a comfortable fixation on a subject's head while ensuring robustness of the signal and user mobility.
For instrument analysis and verification, the hardware design is to be characterized and the physiological value of the measured data is to be evaluated by performing standard tests and BCI classification trials.

2

State of the Technology

In this chapter, the current state of the technology will be reviewed, beginning with a brief overview of NIRS history. Afterwards, the current understanding of NIRS signals and physiology will be summed up, followed by an overview of methods for tissue interrogation as well as theoretical and mathematical models. Then, the literature on NIRS technology will be reviewed, aiming to extract the most critical aspects for a new and next-level design. Finally, current fields of application for fNIRS instruments in research and medicine will be briefly discussed.

2.1 Brief Overview of History

The use of continuous light for the non-invasive investigation of human tissue by transmitting it through parts of the body is a method known for at least a century. While W. C. Röntgen discovered the non-visible spectral range of electromagnetic waves, today known as X-rays, and its benefits for medical diagnosis in 1895, other scientists used transillumination with visible light as an aid in the diagnosis of breast tumors [22] or diseases of the testis [23].
Along with the research on transillumination for anatomical insights, discoveries in the fields of spectroscopy and oximetry laid the foundations of modern physiological diagnosis: Mathematical work on the absorption of light in probes by Lambert (Switzerland) in 1760 and its extension to the Beer-Lambert Law by Beer (Germany) in 1852 [24] provided a description of the absorption of light in homogeneous media. Further research focused on the spectroscopic retrieval of physical and chemical information about the blood and especially hemoglobin in tissue. The works on oxy-hemoglobin spectra (Hoppe-Seyler 1862), hemoglobin as oxygen carrier in blood (Stokes 1864), spectral changes of light penetrating tissue (Vierordt 1876) and others led to the field of medical oximetry: An optical technique for invasive and non-invasive measurement of blood oxygenation. In 1894, Hüfner was the first to conduct spectroscopic in vitro determination of the absolute and relative amounts of oxy-hemoglobin (HbO) and deoxy-hemoglobin (HbR). In 1938, Matthes and Gross performed the first non-invasive clinical absorption measurements for spectroscopic HbO and HbR concentration determination in the ear [25–27]. Further research, e.g. on the optical absorption spectra of HbO and HbR, and the application of the Beer-Lambert Law by Horecker in 1943 led to the first commercial oximeter. In 1970, Hewlett-Packard introduced the first device for clinical oxygen saturation derivation using 8 wavelengths in the ear [28]. Soon after, in 1974, Aoyagi proposed the new approach of pulse-oximetry, which is widely used nowadays [29].

While non-invasive clinical (pulse-)oximetry focused on the global oxygen saturation of the body's arterial blood measured in the ear or in the fingertips, Jöbsis pioneered the field of non-invasive optical methods in 1977 by no longer considering the skull - and bones in general - to be a natural border for light. By using near-infrared light, he proved the feasibility of non-invasive local spectroscopy of cortical tissue oxygenation through the intact skull [1] and is therefore considered to be the initiator of modern functional Near-Infrared Spectroscopy (fNIRS).
Following his publications, research in the late 1980s and in the 1990s mostly aimed to enhance the understanding of the physiology of the signal, NIRS instrumentation and mathematical concepts. This was accompanied by a general growth in development and use of optical instruments for biomedical applications driven by a growing understanding of fundamental optical processes applied to biological materials and the emergence of new optical technologies [30]. In 1988, Delpy provided a modification of the Beer-Lambert Law (BLL) by taking light scattering into account [2]. This so-called "Modified Beer-Lambert Law"' (MBLL) permitted the calculation of relative oxygenation levels from the measured NIRS signal. Several fNIRS instruments were then built with the goal to enhance instrumentation and find ways to obtain absolute values [3–6]. In 1993, four research groups independently demonstrated the feasibility of non-invasive brain activity investigation using fNIRS [7–10], followed by an increase of publications using NIRS technology for brain activity studies. From the 2000s until today, the next major step was to increase the number of optodes and lead to the design of imaging instruments for brain activity mapping from topographic information: functional Near-Infrared Imaging (fNIRI). Today, instruments are introduced that combine fNIRS with EEG [15].

2.2 NIRS Principle and Signals

Functional Near-Infrared Spectroscopy is a diffuse optical method for the measurement of local oxygen-dependent metabolism. fNIRS, Diffuse Optical Tomography (DOT) and Near-Infrared Imaging (NIRI) are all based on the same concept [13]:
Near-Infrared (NIR) light is emitted into the head at one specific position and undergoes random scattering and absorption processes in the tissue attenuating it by 7-9 orders of magnitude. A fraction propagates through the tissue on a banana-shaped path back to the surface where it is then detected by a NIR-sensitive photodetector (see fig. 2.1).

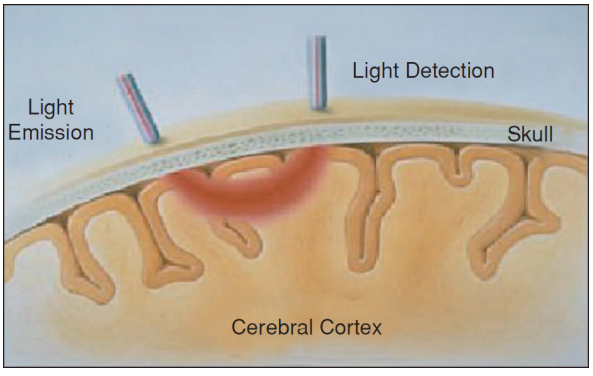

Figure 2.1: Principle of NIRS, fig. taken from [14].

As most parts of the tissue, largely water, are relatively transparent to light in the NIR range, the emitted light can penetrate the cranium and reach sufficient depth [31]. This characteristic optical range of approx. $600 - 900\,nm$ in which tissue is relatively transparent to light is often referred to as *optical window* in literature (see fig. 2.2). While absorption and scattering by components of the tissue (e.g. collagen, proteins, fat ...) remain fairly constant, some chromophores such as oxy-hemoglobin (HbO), deoxy-hemoglobin (HbR) and cytochrome oxidase are strong absorbers for NIR light with their concentrations changing with metabolism and blood flow.

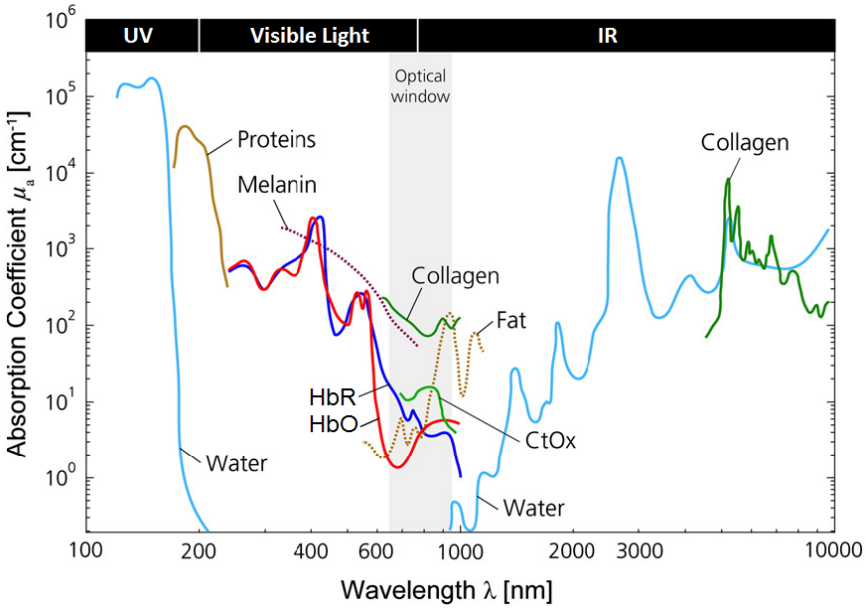

Figure 2.2: Optical window for NIR light, fig. taken from [11].

If two different wavelengths are chosen so that absorption by HbR and HbO is maximal, changes in concentrations of the two chromophores result in measurable attenuation changes that can be quantified, e.g. with the Modified Beer-Lambert Law (see next section). This oxygen-dependent optical absorption is also key to (pulse) oximetry. However, there are certain differences between the two methods:

- Pulse oximetry only monitors changes in the optical density of tissue during pulse intervals, calculating arterial hemoglobin oxygen saturation
- fNIRS measures tissue oxygenation and local hemoglobin oxygen saturation through a cross section of tissue volume including capillaries, arterioles and venules and is referred to as next generation of tissue oxygenation monitors [32].

Some works also use cytochrome oxidase (cytochrome aa3) as a chromophore for the indication of intracellular oxidative processes with cytochrome aa3 being the terminal enzyme of the intracellular respiratory chain [30]. Since this approach is done rarely, it will not be taken into further account in this work.

The interaction between local oxygenation changes measured with fNIRS and electrical brain activity are still subject to research. However, a correlation between local blood oxygenation and neuronal activation (*hemodynamic response*) exists. Three main factors

affecting local HbR and HbO concentrations in the brain were identified by Wolf et al. [33]:

- local cerebral metabolic rate of oxygenation (CMRO2),
- regional cerebral blood flow (rCBF) and
- cerebral blood volume (CBV).

These factors generally occur at the same time during neuronal activation and are summarized as *neurovascular coupling*. During local brain activation, an increase in rCBF disproportional to the increase in oxygen metabolism results in a focal hyperoxygenation [34]. This is reflected in a decrease in HbR concentration accompanied by an increase in HbO concentration of typically 2-3-fold magnitude and thus results in an increase of total hemoglobin [35].
This hemodynamic signal can usually be observed with a latency of approx. 5-8 seconds after the begin of a stimulus/task [18] and is called *slow response* (see fig. 2.3). Focal decrease in HbO along with an increase in HbR is consequently interpreted as deactivation.

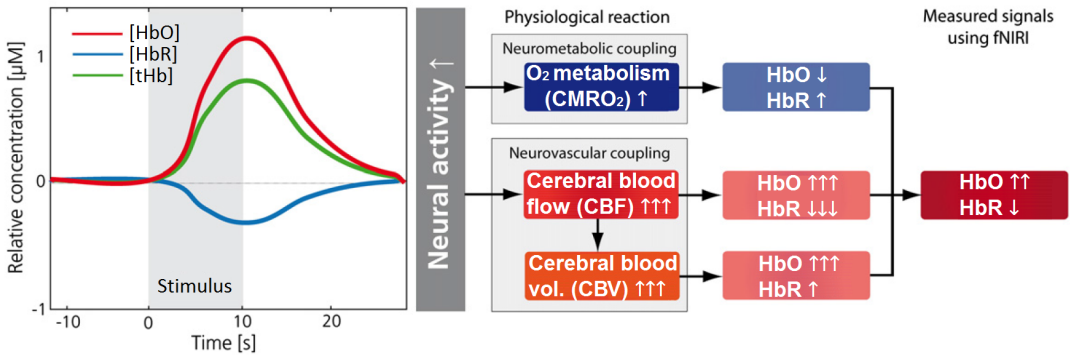

Figure 2.3: Typical NIRS response. HbO: oxy-hemoglobin, HbR: deoxy-hemoglobin, tHB: total hemoglobin, fig. taken from [11].

Since in the *slow response* the oxy-Hb-change is usually larger, it is preferred to the change of deoxy-Hb as a single indicator of brain activity changes. Obrig et al. criticized this, arguing that the decrease in deoxy-Hb is more valid as parameter because of its high negative correlation with the fMRI BOLD signal [35]. This correlation was investigated by several work groups and confirms the theoretical ideas about the nature of the BOLD response ([36], for further references see [12]) but was found to be highly variable between subjects [36].
Another *fast response* signal (latencies in the order of milliseconds) was documented and named Event Related Optical Signal (EROS) [33, 37]. It is thought to appear due to changes in scattering properties of the neuronal membranes during firing. Several research groups suggest that the EROS may correlate with evoked potentials commonly used in EEG [18, 20].
While in the optical NIRS signal the slow response is represented with about 1-2% changes in the signal's DC amplitude [20, 38], the fast response is much smaller and is represented with only 0,05% change in light intensity, requiring averaging techniques with several hundred to a thousand trials [18].

Non-stationary fNIRS signals based on HbO and HbR concentration changes are a combination of several components on which Scholkmann et al. gave a résumé [11]. They consist of:

- Evoked neurovascular coupling by a stimulus or task
- Non-evoked (spontaneous) neurovascular coupling
- Physiological/systemic interference: Evoked and non-evoked processes that are not included by neurovascular coupling.

The following table 2.1 gives a brief overview of the classification of the main components present in fNIRS signals:

		Cerebral	**Extracerebral**
Evoked	**Neuronal**	**Functional brain activity (neurovascular coupling)**: Directly related to functional brain activity. Small changes in relation to the overall variability of the fNIRS signals.	
	Systemic	**Systemic activity type 1**: Changes in blood pressure, $PaCO_2$, CBF / CBV. Strongest parameter affecting CBF/CBV: $PaCO_2$ - Hypocapnia (leads to decrease), hypercapnia (leads to increase)	**Systemic activity type 2**: Changes in blood pressure, skin blood flow/volume
Non-ev.	**Neuronal**	**Spontaneous brain activity (neurovascular coupling)**: Non-evoked, can be used to assess the "resting state functional connectivity" of the brain.	
	Systemic	**Systemic activity type 3**: Heart rate, respiration, Mayer waves, very low frequency oscillations. Hemodynamics or vasomotion associated with spontaneous hemodynamic oscillations - not stimulus evoked.	**Systemic activity type 4**: Heart rate, respiration, Mayer waves, very low frequency oscillations.

Table 2.1: Classification of main components present in fNIRS signals, based on [11].

Systemic activities type 3 and 4 are mostly periodic artifacts in the signal such as

- Heartbeat with $\approx 1 - 2\,Hz$
- Respiration with $\approx 0.3 - 0.1\,Hz$
- Mayer waves with $\approx 0.1\,Hz$

Mayer waves are spontaneous low-frequency blood pressure variations with resulting oscillations in both vascular and metabolic responses [39]. Their origins are not fully understood to this day.
To remove these artifacts or separate the signal components, several approaches were proposed. Univariate Methods: Band-pass and low-pass filtering to remove non-evoked components such as heartbeat and respiration (cut-off frequency of e.g. $0.2\,Hz$) and conventional averaging of fNIRS signals that are time-locked to the trials are commonly used. Further approaches are Hilbert spectral analysis / eigenvalue decomposition [40],

adaptive filtering techniques [41], Wiener filtering, discrete wavelet filtering [17], sliding window motion artifact rejection [42] and least squares regression (for more references see [11] and [12]).
Other approaches use multivariate methods such as several fNIRS signals from different source detector distances to identify and reduce the effects from extracerebral tissue such as scalp and skull.

2.3 NIRS Interrogation Approaches

There are three different functional Near-Infrared Spectroscopy interrogation techniques, each of which having their advantages and disadvantages:

- Continuous Wave NIRS (CW NIRS)
- Frequency Domain NIRS (FD NIRS) and
- Time Domain NIRS (TD NIRS).

In the following, all three techniques will be briefly described.

2.3.1 Continuous Wave NIRS

In the CW method (see fig. 2.4) continuous, slowly (kHz) chopped or modulated light at constant amplitude I_0 is used to transilluminate the tissue. The attenuation of the amplitude over time and the relative absorption are measured and evaluated.

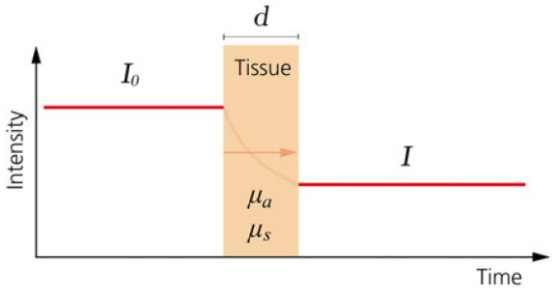

Figure 2.4: Continous Wave NIRS principle, fig. taken from [11].

Due to slow or no modulation of the light, its time changing component (e.g. phase shifts) cannot be resolved in this method. Consequently, it is not possible to differentiate between light scattering μ_s and absorption μ_a effects. Thus, only relative concentration changes of the chromophores based on a baseline can be determined.
The advantages of the method are nevertheless big: The technology is relatively low-cost, it can be integrated and miniaturized, it is lightweight and also works with mobile applications using wireless technology.

2.3.2 Frequency Domain NIRS

In the FD method (see fig. 2.5), first suggested by Gratton [43], light is intensity-modulated at radio frequencies in the range of several $10 - 100\,MHz$ and then sent

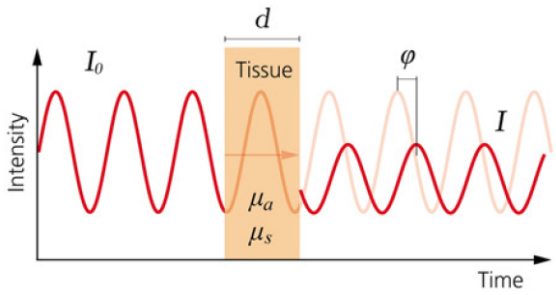

Figure 2.5: Frequency Domain NIRS principle, fig. taken from [11].

through the tissue. Photomultiplier tubes or fast photodiodes detect the signal, which now shows attenuation as well as a phase shift ϕ with respect to the incident signal. The measurement of ϕ allows the calculation of the optical path length and thereby differentiation between scattering and absorption effects. Thus, absolute chromophore concentrations can be determined. This method provides a higher SNR and is generally faster and less expensive than TD-systems [12] and uses narrower bandwidth. On the other hand, costs, complexity and volume of the instruments are considerably higher than in CW systems.

2.3.3 Time Division NIRS

TD methods (see fig. 2.6) introduce short picosecond pulses of light, which are broadened (scattering) and attenuated by the various tissue layers such as skin, skull, cerebrospinal fluid and brain [13]. The temporal point spread function of the photons leaving the tissue is then used for the determination of changes in attenuation and the optical path length.

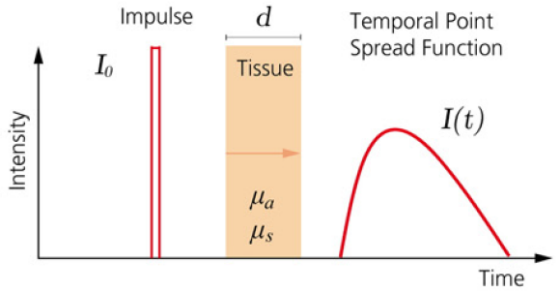

Figure 2.6: Time Domain NIRS principle, fig. taken from [11]

While TD systems can detect ballistic and diffusely scattered photons, they are expensive, require significant averaging times to improve SNR [44] and are often large and not directly suited to clinical monitoring [30].

Since quantification of absolute values is not as important in neuroscience as to detect brain activity changes with statistic significance, up to today most fNIRS and fNIRI systems in research as well as those commercially available on the market are based on Continuous Wave technology [11]. With respect to scope, expenses and mobility, this work focuses on the design of a CW system for neuroscience and BCI research.

2.4 Theoretical Background

To approach the widely used Modified-Beer Lambert Law (MBLL), the unmodified Beer-Lambert Law (BLL) will be briefly introduced and then expanded.
The original BLL describes a simplified case in which light is sent through a volume filled with only one absorbing compound dissolved in a non-absorbing solvent, as is the case in an in vitro spectrophotometric analysis.

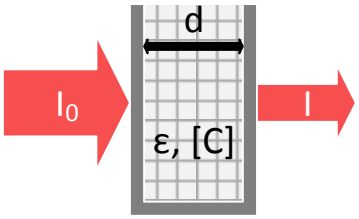

Figure 2.7: Cuvette model for Beer-Lambert Law for in vitro spectrophotometric analysis.

For such a *cuvette model* (see fig. 2.7), the BLL states that the attenuation A of an interrogating monochromatic energy with incident intensity I_0 is proportional to the product of the compound's concentration c in mol, its molar extinction coefficient ϵ_λ, and the optical path length d

$$I = I_0 \cdot 10^{-\epsilon_\lambda cd} \Leftrightarrow A = -\log_{10}\left(\frac{I}{I_0}\right) = \epsilon_\lambda cd. \tag{2.1}$$

In practice, samples have usually more absorbers than one. To determine the concentration of each of the i chromophores, measuring at i wavelengths and setting up a system of equations is necessary. Furthermore, chromophore concentrations are time-dependent and as in case of fNIRS optodes, the optical path length is not straight and equal to the distance d between light emitter and receiver but often assumed to be banana-shaped (see [12] for further investigation of the light path) and has to be corrected by the *Differential Pathlength Factor - DPF*:

$$A(t,\lambda) = -\log_{10}\left(\frac{I(t,\lambda)}{I_0(t,\lambda)}\right) = \sum_{i=1}^{n} \epsilon_{i\lambda} c_i(t) DPF(\lambda) d \tag{2.2}$$

Since this law does not take scattering into account, it is still solely applicable to interrogated volumes in which only absorption takes place, and can thereby not be used for tissue interrogation. To improve this, Delpy et al. modified the BLL by adding a *scattering dependent light intensity loss parameter* G [2].

$$A(t,\lambda) = -\log_{10}\left(\frac{I(t,\lambda)}{I_0(t,\lambda)}\right) = \sum_{i=1}^{n} \epsilon_{i\lambda} c_i(t) DPF(\lambda) d + G(\lambda) \tag{2.3}$$

With G in the equation, chromophore concentrations cannot be calculated without knowing the scattering influence. Instead, Delpy et al. proposed to calculate the chromophore concentration changes by building the difference of two measurements from an initial time

point t_0 and a consecutive timepoint t_1 using the modified Beer-Lambert Law, thereby removing the scattering influence G from the equation and also canceling out the emitted intensity I_0, which is constant:

$$\Delta A(\Delta t, \lambda) = -\log_{10}\left(\frac{I(t_1, \lambda)}{I(t_0, \lambda)}\right) = \sum_{i=1}^{n} \epsilon_{i\lambda} \Delta c_i(t) DPF(\lambda) d \tag{2.4}$$

When oxy-hemoglobin and deoxy-hemoglobin are evaluated at two wavelengths and two consecutive points in time, the resulting system of equations can easily be solved for the changes in concentrations Δc_i. The concentration changes of HbO and HbR are then given by

$$\begin{bmatrix} \Delta[HbR] \\ \Delta[HbO] \end{bmatrix} = \frac{1}{d} \cdot \begin{bmatrix} \epsilon_{HbR,\lambda_1} & \epsilon_{HbO,\lambda_1} \\ \epsilon_{HbR,\lambda_2} & \epsilon_{HbO,\lambda_2} \end{bmatrix}^{-1} \begin{bmatrix} \frac{\Delta A(\Delta t,\lambda_1)}{DPF(\lambda_1)} \\ \frac{\Delta A(\Delta t,\lambda_2)}{DPF(\lambda_2)} \end{bmatrix} \tag{2.5}$$

Using the MBLL for the determination of relative chromophore concentrations in the brain, several assumptions have been made which were identified and discussed by Obrig and Vilbringer [35] and Boas [45].

1. **The change in scattering is small compared to the change in absorption**: This permits to disregard G in the step of equation 2.4 and allows to assume the DPF at certain wavelengths to be constant. This assumption is generally assessed plausible.
2. **The medium in which changes are monitored is homogeneous:** Being clearly a wrong assumption, this is seen to be one reason for the low spatial resolution of non-invasive NIRS compared with invasive optical techniques.
3. **The change of parameters of interest (especially chromophore concentration) is homogeneous within the sampling volume:** Related to the assumption above, this is also wrong: Besides the cortical region, the sampling volume consists of scalp and skull. Therefore, the region of hemoglobin change is relative to the entire sampling region. This introduces an additional source of error stemming from the wavelength dependence of the DPF in the signal.

Despite the MBLL being only a reasonable first approximation, almost all CW approaches so far are based on it [35]. This is predominantly justified by the focus of interest in brain research being much more on the trend of the signals than on its quantification [11]. So far, its "validity [...] has tested favorably against several other monitoring modalities and theoretical studies suggest that any resulting errors can be limited to less than 10%" [13].

To use the MBLL, several parameters have to be specified and were subject to theoretical and experimental research predominantly in the 90s. The extinction coefficients of the chromophores were determined in vitro using laboratory spectrophotometers and can be looked up in tables such as in [21]. For CW technology, which does not enable the direct measurement of optical path lengths such as in FD and TD systems, particularly the DPF was both experimentally and numerically investigated. Findings were that the DPF is age, gender- and wavelength-dependent, varying up to 15% between subjects with a mean value of 6.53 ± 0.99 [46, 47].

Okada et al. compared experimental measurements on phantoms with mathematical predictions by Monte Carlo Method and Finite Elements Method on four models [31] to

determine sensitivity profiles dependent on the partial optical path lengths in the different types of tissue and source-detector spacing (see fig. 2.8).

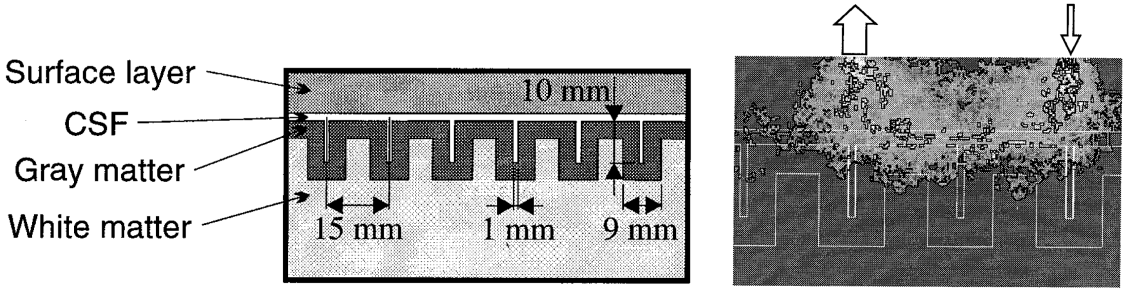

Figure 2.8: Model and spatial sensitivity profile for a source-detection distance of 30mm, fig. taken from [31].

They found that

- at small detection positions ($\leq 15\,mm$), the mean optical path length is approximately equal to the partial mean optical path length of the surface layer (skin, skull) resulting in the spatial sensitivity profile being confined to this surface layer.
- at intermediate positions ($\geq 15\,mm, \leq 25\,mm$), the partial mean optical path lengths of both cerebrospinal fluid (CSF) and gray matter (GM) layers increase with detection position.
- at large detection positions ($\geq 25\,mm$), the partial mean optical path lengths of surface and GM layers remain approximately constant while that of the CSF layer increases with source-detector spacing.

They concluded that for a source-detector spacing of 50mm, light spends approximately 65% of its path in scalp and skull, approximately 35% in the CSF and only approximately 5% in the gray matter of the cortex. Nevertheless, the contribution of the gray matter layer was estimated to be at least 20-30% of the absorption change in the NIRS signal.
In literature, commonly used source-detector distances resulting in a clear brain activity signal are between $3 - 4\,cm$ with the rule of thumb for frequency domain and continuous measurements that the depth of maximum brain sensitivity is approximately half the source-detector separation distance [13].

2.5 Review of existing fNIRS Technology

As a preparation for the CW fNIRS system design, the literature on NIRS instrument development approaches was reviewed. Tab. A.1 and A.2 (see Appendix A) summarize some of the important and comparable features of instruments developed by work groups around the world.
As can be seen, almost all instruments are based on CW technology, about two-thirds using lock-in approaches for improvement of the signal-to-noise ratio [18–20, 30, 44, 45, 48–53]. While some instruments use Time-Division Multiplexing (TDM) techniques, activating only one NIRS channel at a time [15, 32, 38, 45, 49, 52–55], others use frequency-encoded simultaneous emission and band-pass filter extraction or software based demodulation schemes [19], enabling the continuous measurement of all channels.

It should be pointed out that many work groups use external desktop lock-in amplifiers such as from the Ametek series [18, 50] or external ADC/Data Acquisition instruments, e.g. National Instruments or Keithley DAQ USB or PCI devices [18, 19, 49, 50, 53]. Such NIRS instruments dot not work stand-alone and are usually not portable.
Only two stand-alone instruments were found that provide wireless data transmission for mobile deployment [15], [56].

In a review on CW functional Near-Infrared Spectroscopy and Imaging instrumentation and methodology by Scholkmann et al. [11], a comparison of the first commercial instruments on the market can be found (see fig. A.1, Appendix). The variety of these instruments ranges from

- systems with few sources/detectors suitable for local detection of certain brain areas to systems covering the whole head
- a few instruments using sensor patches with integrated components to the majority of instruments using optical fibers and flexible head caps
- most fNIRI devices being larger in size and static to very few being attached to the subject providing wireless data transmission
- some 10,000 USD to several 100,000 USD for whole-head imaging systems

In the following, some of the key components of NIRS instrumentation will be discussed.

2.5.1 NIR Light Emitters

The ideal light source provides multiple monochromatic wavelengths in the near-infrared range, each at relatively high power for higher penetration depth [13]. At the same time, the radiation variance should be minimal: If there is no additional monitor for the intensity of the interrogation beam, fluctuations in the radiation intensity cannot be discriminated from changes in absorption due to changes in chromophore concentration in the tissue. At last, the radiation spectrum of the light source should be as sharply peaked as possible, ideally being monochromatic. However, if the emission spectrum is known, weighted averaging approaches can be used to correct the extinction coefficients [11]. Collimation of the input light is less important for the intensity at the detector than the power of the incident light itself, as scattering processes in the first millimeters of the tissue rapidly make the collimated interrogating beam diffuse [21].
For near-infrared light emission into tissue, mainly three types of sources are possible:

- Laser Diodes (LD)
- Light Emitting Diodes (LED)
- White Light Sources (e.g. Xenon flash tube or quartz halogen light) with monochromators/interference filters

The use of white light sources has so far not been documented, as they require filters, they are large and most importantly dissipate much heat. This makes them not suitable to fNIRS instrument applications. The two other options - laser diodes and light emitting diodes - are both often used in NIRS instruments, each having their advantages and disadvantages (see tab. 2.2).
Laser Diodes that have been used for fNIRS instrumentation are, among others, Sanyo DL7140-201 and Hitachi HL8325G [45], Vertical Cavity Surface Emitting Lasers [52] and Laser Diode Labs LA68 and STC LA8 [3]. A table and comparison of commercially available pulsed high-power laser diodes can be found in [21].

LDs	PRO	+ Sharp radiation peak: coherent, almost monochromatic light emission + Pulsatile operation allows ns pulse widths with peak powers of up to 10W [30]
	CON	- Often in large packaging, miniaturizing is more challenging - Higher safety demands to prevent eye damage - Have narrower operating range - Available wavelengths are limited, between $695 - 775\,nm$ expensive [11] - Extreme heating of the semiconductor junction often requires optical fibers to carry light to and from tissue [53]
LEDs	PRO	+ available in packages with 2 or more individually controllable wavelengths + Since the photons are incoherent / uncollimated, a higher emission into tissue is possible than by LD with the same maximum permissible exposure[19] + Easy to adjust, have a broader operating range than LD + Available in greater variations, giving more freedom in wavelength selection + Minimal power consumption and minimal heat dissipation problems
	CON	- Wider emission spectrum: typ. bandwidth $25 - 50\,nm$ - Lower optical power output to consumption ratio than LD

Table 2.2: Comparison of LED and LD for use in fNIRS instrumentation.

Particularly in more up-to-date approaches, Light Emitting Diodes are often used. Work groups chose multi-wavelength LEDs from Epitex [14, 15, 38, 49, 53, 54, 57] such as the Epitex L760/850, different models from Optodiode [19, 20, 58] such as OD-7860, APT-0101 or APT-0010 or from Hamamatsu, e.g. L6112-01 [50] and others.

The selection of the optimal NIR wavelengths is crucial and will be discussed in detail in subsection 3.4.1.

2.5.2 NIR Light Detectors

Mainly three types of detectors can be used to detect the near-infrared light coming from the tissue:

- Photomultiplier Tubes (PMT)
- Silicon p-i-n Photodiodes (SPD)
- Avalanche Photodiodes (APD)

In PMTs, based on the external photoelectric effect, photons free electrons from a photocathode surface, which are then accelerated by a strong electric field, raising their kinetic energy. These high-energy electrons knock out secondary electrons from a cascade of dynodes which themselves are accelerated by the field, thereby multiplying the current which is produced by the incident light by up to 10^6 to 10^7 [11].
In SPDs and APDs free charge carriers are created based on the internal photoelectric effect: Incident photons are absorbed by the semiconductor junction and thereby raise electrons to higher energy, creating drifting electron-hole pairs that result in a detectable photocurrent.
Avalanche Photo Diodes use a similar principle to PMTs: A large electrical field is applied across the APD junction that accelerates free electric charge carriers generated by photon absorption. Those free carriers are again accelerated and generate more carriers through impact ionization, resulting in the so-called avalanche effect. By application of up to several hundred volts, an internal amplification in the range of a few hundred times [11] can be achieved.
Photo diodes have no internal signal amplification. Emerging photocurrents have to be

amplified by external circuitry in one of two possible operation modes: In *photovoltaic mode*, no bias voltage is applied and the generated photocurrent is measured over a large load resistance. The response of the signal to the optical power is logarithmic and much slower than in photoconductive mode but enables a higher dynamic range. In *photoconductive mode*, a reverse voltage is applied over the semiconductor junction, reducing the junction's capacitance, thus the response time, but also increasing dark current. The resulting current is measured across a small load resistance, the output voltage being linear to the incident optical power.
At this point, it should be pointed out that while other photo diode types are available, silicon semiconductors are the most favorable due to their higher sensitivity and better noise characteristics in the NIR spectrum compared to others, e.g. GaAs photo diodes [54].

The detector choice largely determines the resulting sensitivity of the instrument, the maximum sampling rate and the dynamic range [13] and has to include a consideration of the advantages and disadvantages in the context of NIRS application (see tab. 2.3).

PMTs	PRO	+ Gold standard in terms of sensitivity: Allow single photon counting + Large gains up to 10^7 + High speed similar to APDs [11] + Comparable dynamic ranges to APDs, but lower than SPDs
	CON	- Highly vulnerable to ambient light, high light intensities can result in damage to the device - Large, bulky apparatus - Sensitive to magnetic fields - Require high voltage supplies (safety) - Require cooling and voltage stabilization
SPDs	PRO	+ Very small packages + Require only low voltages - can be mounted on the head + Easy to use, no voltage supply stabilization or cooling necessary [13] + Robust to ambient light exposure + Not sensitive to magnetic fields + High dynamic ranges of up to $100\,dB$ [13] + Fast: Support speeds up to $100\,Mhz$ [13]
	CON	- Low sensitivities - Higher trans-impedance gains reduce SNR and bandwidth - No internal amplification, preamplifiers must be low-noise and carefully designed
APDs	PRO	+ Moderate or small packages + Higher sensitivities than PD + Moderate internal gains from 10 to a few 100 + Robust to ambient light exposure + Not sensitive to magnetic fields + Good dynamic ranges of up to $60\,dB$ [13] + Faster than SPDs: Support frequencies $> 100\,Mhz$ [13]
	CON	- Require high voltages of several $100\,V$ (safety) - Require stabilized power supplies - Require cooling due to dependency of internal gain on temperature/bias voltage [13]

Table 2.3: Comparison of PMT, SPD and APD NIR-detectors for use in fNIRS instrumentation.

Photo Multiplier Tubes such as the Hamamatsu R928 or R936 were used mainly in the first publications on fNIRS devices (Cope 1991 [21] and Rolfe et al. 2000 [30]). More recently, PMTs find application in Frequency Division instruments but are all in all rarely

used and have mostly been replaced by Avalanche Photo Diodes.
Avalanche Photo Diodes and Silicon Photo Diodes are both commonly used in today's NIRS instrumentation approaches with the trend of SPDs being preferred. Regarding APDs, most detectors used in literature are fabricated by Hamamatsu, with the Hamamatsu C5460-01 being the most popular [18–20, 45, 50]. For Silicon Photo Diodes, many work groups used Burr Brown sensors such as the OPT101 [14, 53] or OPT209 [44], detectors from Opto Diode Corp. [15, 59] and Siemens [49].

2.5.3 Optical Conduction

While silicon photo diodes and light emitting diodes can be applied directly to the head, white light sources, laser diodes, avalanche photodiodes and photo multiplier tubes traditionally require optical conduction with optical fibers to and from the scalp. Step-index multimode fibers with a core diameter of $\approx 0.5\,mm$ are normally used to guide the light from the light sources to the head. For the conduction from the scalp to the detectors usually fiber optic bundles with larger diameter, e.g. $\approx 2.5 - 3\,mm$ [20, 50] and high numeric aperture maximize the amount of collected light [11].
The fibers have to be attached to the head by fiber holders on straps or caps and add weight, generally decreasing mobility and comfort. Also, good light coupling of the light from the emitting source into the fiber has to be ensured to minimize losses.
When the sources and detectors are placed directly on the head, the geometrical design of the probe is slightly more constrained, and potential heating as well as electric hazards have to be considered. On the other hand, light losses are minimal and the user mobility is less restricted.
As the aim of this work is to design a mobile NIRS instrument, the use of optical fibers and sources/detectors requiring them is not planned and therefore will not be further evaluated at this point.

2.5.4 Signal Amplification

As the functional NIRS signal in the detected optical signal is very weak, low-noise amplification and signal extraction techniques are applied. One often used method is the synchronous (lock-in) detection, which will be discussed in detail in later sections. Using lock-in detection enhances the SNR but also increases system complexity. Using fast light modulation, only photodetectors with an appropriate bandwidth can be used.
To increase the dynamic range of the instrument, variable/programmable gain amplifiers can be used.

2.5.5 Probe Designs

Over the last years, several different approaches for optical probe designs were published. As good coupling of the probes is a significant precondition for high performance and signal quality, many probe designs aim to minimize obstruction of hair and motion effects. Design approaches that were published in literature include

- Conus- and cylinder-shaped single probes for fixation on EEG caps/hair nets and chained patches [15, 49],
- Multiple probes and multidistance probes on flexible PCBs with cushioning material [12, 14, 30, 53, 58, 59],

- Probes integrated into helmets and helmet-like headsets [48, 52] and fixated mechanical mounting structures to sit in [20].

Flexible PCBs with cushioning material bear the disadvantage of laminar resting against the head, thus promoting the obstruction through hair. For this reason, most of the flexible PCB probe designs are applied only to the forehead.

2.6 Fields of Application

The current and future fields of application of NIRS instrumentation for brain activity assessment can be assigned to three overlapping topics: brain research, clinical context and brain computer interface research.

Basic brain research
Brain activation studies were conducted on the visual, the somatosensory, the auditory, the motor and the language system, and on cognitive performance (see [14] for references). In 2003, Izzetoglu et al. conducted functional activity monitoring as a measure of cognitive workload in complex tasks such as aircraft landing situations and warfare management [60]. Psychiatric research is assessed to be still wide open for diffuse optical techniques [13], with the use of fNIRS for brain dysfunction assessment and research [12] and neonatal studies of cognition [48] being further related fields of application. All in all, the interest in the use of fNIRS for basic physiological, biochemical and routine clinical applications has steadily increased since the mid-1970s [30].

Clinical applications
The main clinical interest initially lay in long-term monitoring of cerebral oxygenation in newborn and high-risk infants [3, 21]. More up-to-date neurological applications are the investigation of hemodynamic responses during deep-brain stimulation in Parkinson's patients, brain activation during induced seizures in patients with epilepsy, verbal fluency and cognitive tasks in Alzheimer's patients, prefrontal brain activations of schizophrenic patients (see [14] and [13] for references) and recently inspection of the state in amyotrophic lateral sclerosis (ALS) (see [19] for references). Other potential applications are cortical blood flow monitoring and early diagnosis of cerebral pathologies of vascular origin [51], brain trauma and surgical intervention monitoring [45] and non-invasive monitoring of cerebra ischemia resulting from critical reduction of oxygen and glucose supply [56].

Brain Computer Interfaces
In the last decade, an increasing number of work groups used fNIRS technology for BCI-tasks and proved its applicability in the BCI context (e.g. [20, 50, 61–64]). Experiments were conducted in which motor cortex activity in actual and imagined tasks could be used as BCI control signals for severely paralyzed patients due to stroke, spinal cord injury or ALS [17, 62]. Cognitive workload assessment for the performance output optimization of context-sensitive systems has been done [60] and NIRS technology has been proposed for hybridization with EEG to act as a brain switch for classification performance improvement in hybrid BCIs [16, 64]. The use of fNIRS in BCI applications is promising because of its compact, robust and safe use and long-term applicability. In contrast to EEG, very little training efforts are necessary. As a very young field of research, fNIRS BCIs is assessed as promising new modality [65].

3

System Design

3.1 Preliminary Remarks

The NIRS instrument was developed in three major design steps (see fig 3.1):
First, an evaluation board was designed. Implementing main elements of the later NIRS instrument on a mid-scale PCB enabled easy testing and debugging. As a second step, prototypes were designed and produced. Findings from evaluation and testing were included in succeeding designs. Finally, a compact 4-layer final version was designed and then manufactured by a professional PCB manufacturer.

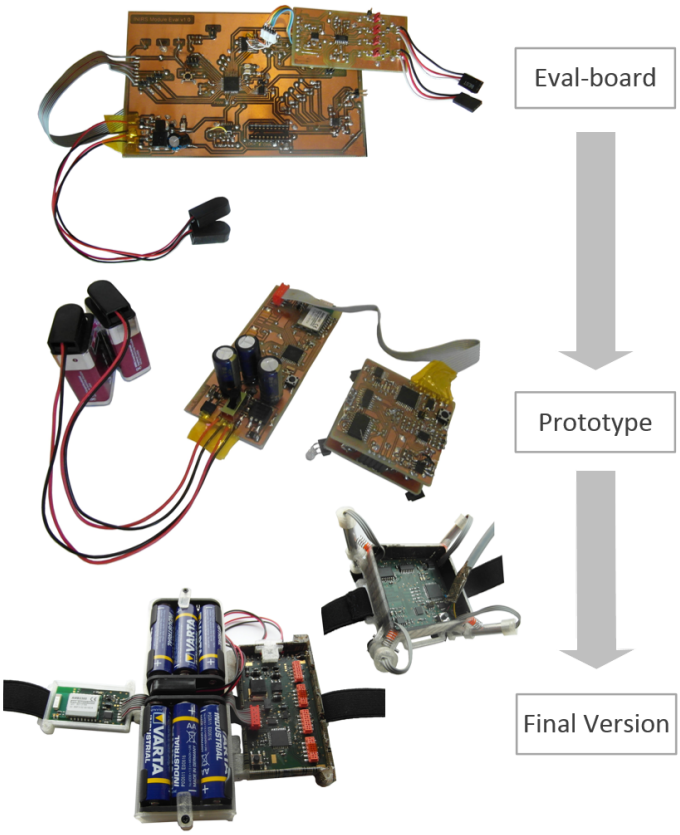

Figure 3.1: Instrument design process.

All evaluation and prototype versions were produced by hand with a standard UV exposure and etching process that is depicted in the Appendix (see fig. A.2).

The following sections of this chapter will provide a detailed description of the system design. For better clarity, the design process was subdivided into thematic sections. The first part revolves around noise, crosstalk and error sources that were taken into consideration during hardware design. Then, the overall system concept and instrument's basic functionality will be depicted. Based on this concept, the hardware design of the instrument is then subdivided into two modules and commented in detail, followed by a short section on user safety design aspects. Finally, the software and mechanical design will be explicated.

For explanation purposes, excerpts of the schematics will be given in the text. The whole schematics can be referred to in the Appendix. The basic software functionality will be described using flow charts and mechanical concepts will be illustrated with 3D renderings. The software code and mechanical drawings are partly depicted in the Appendix and fully supplied on the annexed data carrier.

3.2 Noise, Crosstalk and Error Sources

In this section, noise, crosstalk and other error sources will be examined as preparatory work for the system design.

3.2.1 Noise Errors

There are three main types of noise in photodetector systems:

- *shot noise*,
- *dark current*,
- *thermal noise*.

Shot noise is based on the quantum nature of the photons and cannot be avoided completely by technical means. Being quantized and discrete, the photons arrive independently of each other, resulting in random fluctuations in photon-to-electron conversion in the detector over time. Without internal amplification, the shot noise power is proportional to the square root of the average intensity (the number of incident photons) [11]. This results in the fact that the accuracy of the measurements increases with the intensity of the detected light in a constant time window. Shot noise can be minimized by shielding the detector from background radiation, e.g. with opaque covers [44], or NIR bandpass filters [11].
Dark current is the current flowing in the detector in completely dark conditions (no incident photons) and is highly influenced by the temperature of the material. To minimize dark current due to thermal generation, the device can be cooled.
Thermal noise is white noise resulting from Brownian motion of charge carriers in resistors internal and external to the detector, and is proportional to the resistor value

$$\bar{u^2} = 4k_B T R \Delta f, \tag{3.1}$$

where $\bar{u^2}$ is the mean square voltage variance, k_B is the Bolzmann's constant, T is the absolute temperature of the resistor in Kelvin, R is the resistor value in Ω and Δf is the

spectral bandwidth in Hz over which the noise is measured.
In detectors with internal gains (for instance PMTs or APDs), photonic shot noise and dark currents are amplified together with the signal. Thus, thermal noise is typically small compared to the signal and becomes negligible, requirements of the preamplifier components in terms of noise are therefore reduced [11]. In detectors without internal gains (e.g. SPDs), however, the preamplifier circuitry must be carefully designed to minimize noise pickup and enable a good SNR.

In the following, based on the work of Cope in 1991 [21], a brief mathematical description of the noise in a photodetector is derived:
For photon shot noise (the random arrival of photons at the detector), the probability of n photons arriving in a time interval τ is given by the Poisson distribution

$$P(n,\tau) = \frac{(\eta N_p \tau)^n}{n!} e^{-\eta N_p \tau}, \tag{3.2}$$

where N_p is the average photon arrival rate and η is the quantum efficiency of the detector. Mean μ_p and variance σ_p^2 of the Poisson distribution are given by

$$\mu_p = \eta N_p \tau \tag{3.3}$$

$$\sigma_p^2 = \mu_p \tag{3.4}$$

and thus the SNR of purely Poissonian noise is

$$\mathrm{SNR}_p = \frac{\mu_p}{\sigma_p} = \sqrt{\eta N_p \tau}. \tag{3.5}$$

Dark emission due to unwanted background light or thermal emission from the detector contributes additional noise [21]:

$$\sigma_d^2 = N_d \tau \tag{3.6}$$

Hence, the overall SNR of the detector is

$$\mathrm{SNR}_{\mathrm{detector}} = \frac{\eta N_p \tau}{\sqrt{\eta N_p \tau + N_d \tau}} \tag{3.7}$$

From eq. 3.7 it can be seen that for a high SNR

- the dark noise should be much lower than the optical signal,
- the quantum efficiency of the detector should be as high as possible (near unity),
- the photon arrival rate should be high (the interrogating light intensity as high as possible),
- the noise reduction is proportional to the square root of the total photon count and thereby to the measurement interval τ: noise reduction $\propto \sqrt{N_{\mathrm{photon}_{\mathrm{total}}}}$ [44].

The detector's collection efficiency is proportional to its active area and the square of its numerical aperture [21]. Together with careful design regarding thermal noise influences, these findings were considered for the system design approach.

3.2.2 Crosstalk

There are two main origins of optical crosstalk in NIRS systems:

- *Intrinsic crosstalk*: Change in HbR may mimic a change in HbO and vice versa. One source of this crosstalk is the *partial volume effect* [12] that results from estimates of the correct path length factors (DPFs) (using constant mean path lengths in the MBLL), which are wavelength-dependent [66]. These estimates often have systematic errors that can create crosstalk between species in the estimated concentration changes.
  The size of the intrinsic crosstalk is highly wavelength-pair-dependent and can be significantly reduced by the selection of an optimal wavelength pair [67] (see section 3.4.1).
- *Crosstalk between different sources* that illuminate one detector: When there are more active light sources than one at the same time, NIR light from one source can reach a detector of another active source. This can be minimized by using I-Q-/frequency modulation/demodulation or by time-sharing of the sources (Time-Division Multiplex).

Furthermore, as usual in system design of acquisition instruments, electrical crosstalk should be minimized, e.g. by shielding and large ground planes.

3.2.3 Other Error Sources

Finite bandwidth effect: As the MBLL is only valid for monochromatic light sources, finite bandwidth effects have to be taken into account. In practice, all light sources have a finite bandwidth, beginning with a few nm for laser diodes up to several $10\,nm$ for LEDs. The effect can be mathematically described as follows [21].
The measured transmission $\tilde{T}$ is given by

$$\tilde{T} = \frac{\int_{\lambda_1}^{\lambda_2} I(\lambda)S(\lambda)10^{-A(\lambda)}d\lambda}{\int_{\lambda_1}^{\lambda_2} I(\lambda)S(\lambda)d\lambda}, \tag{3.8}$$

where $I(\lambda)$ is the input light intensity, $S(\lambda)$ is detector sensitivity and $A(\lambda)$ is the monochromatic absorbance. The measured absorbance $\tilde{A}(\lambda)$ is then given by

$$\tilde{A} = \log_{10}(\frac{1}{\tilde{T}}). \tag{3.9}$$

As in the fNIRS context $A(\lambda)$ is not constant, the source and detector wavelength dependencies will have an effect: The measured attenuation is less than the theoretically expected value for the mean of $A(\lambda)$ between λ_1 and λ_2 [21].

Stray radiation: Other light sources such as sunlight or room light sources also emit light in the NIR range and thereby effect the detector signal. The acceptable amount of stray light is dependent on the maximum positive absorbance change observed [21]. Its influence can be reduced by opaque covers, frequency modulation techniques, and the subtraction of a dark current intensity baseline that is measured during inactive NIR emitter time slots.

System non-linearities and **system drift** must be avoided in system design and have to be assessed before the instrument is used for the collection of physiological data (see subsection 4.1.5).

3.3 System Concept

The designed fNIRS instrument is based on a modular design (see fig. 3.2). The main development is a 4-channel Continuous Wave NIRS module that provides full stand-alone functionality.
Up to four of these modules can be connected to a mainboard that provides a simple parallel $4\,Bit$ control interface, the power supply rails and converts the analog signals. This modular design has the advantage of being adaptive to the requirements of future applications and research, it enables spatial distribution of the hardware (and weight), it allows direct hardware signal processing (thus minimizing noise and interferences) and it was premise for a much more efficient debugging and development process.

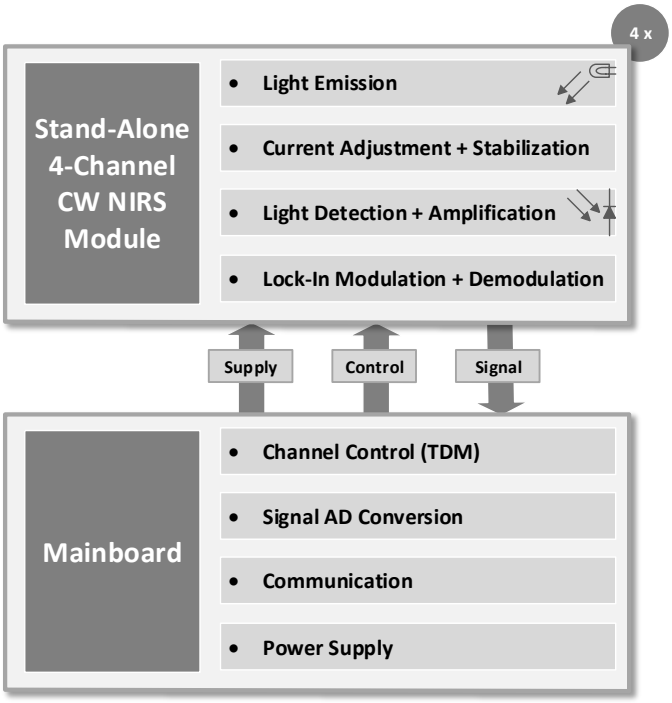

Figure 3.2: Modular system concept of the developed CW fNIRS system.

Each module provides four complete NIRS channels with two wavelengths each, consisting of four dual-wavelength light emitters, eight adjustable current regulators, one central light detector and lock-in modulation and demodulation of the light signals, as well as pre- and post-amplification of the detected signals.
The system uses Time-Division Multiplexing (TDM) for the NIRS channels. This is a trade off between preventing inter-channel crosstalk and sacrificing SNR, which is limited by the width of the applied time windows. The modules work stand-alone, with the interface requiring only the power supply, the above-mentioned parallel control signals for the activation of one of the module's four NIRS channels and providing the associated outgoing analog NIRS signal. Hence, any customization is possible and the NIRS module can also be used stand-alone, e.g. with NI DAQ equipment or any customizable hardware.
As one objective of this work was to provide CW NIRS instrumentation for mobile applica-

tions, a controller mainboard was developed for this purpose. The heart of the mainboard is a microcontroller unit that

- adaptively controls the NIRS modules
- enables communication with the user via the UART protocol using a RS232 cable or the onboard Bluetooth wireless controller
- and supervises the analog-to-digital conversion of the incoming analog NIRS signals.

The board is designed for the connection of up to four NIRS modules, allowing up to 16 channels to be individually addressed and activated. The number of active NIRS modules can be configured at any time, enabling the adaption of the instrument to the needs of the experimental protocol and allowing to reduce the amount of active hardware and thus power consumption.

Figure 3.3 depicts a more detailed version of the above-introduced system concept for further commentary.
The upper part of the NIRS module shows the basic elements of NIR light modulation, current regulation and adjustment. Each of the four NIR light sources supplies two wavelengths, resulting in 8 channels that are controlled individually.
Each channel's current is regulated by a separate current regulator circuit consisting, among others, of a high-precision operational amplifier and a FET transistor. The activation and modulation of each of the channels for lock-in amplification is done by analog switches that are controlled by a 1:8 demultiplexer.
Heart of the NIRS module is a microcontroller that controls all functional units on the board. For NIR light lock-in modulation and demodulation, it supplies a $3.125\,kHz$ pulse width modulation (PWM) signal that is fed into the 1:8 demultiplexer. By choosing the demultiplexer channel, the controller activates one of the 8 NIR light channels and the PWM signal is fed through to the corresponding current regulator, where it modulates the analog switch and with that the current regulator input.
The current value that is the command variable for the current regulator is adjusted by a voltage at the current regulator inputs. This voltage is produced by a 1 channel $8\,Bit$ digital-to-analog converter (DAC) circuit controlled by the microcontroller.

The elements for light detection and amplification are depicted in the lower part of the NIRS module.
A light detector with integrated trans-impedance amplifier (TIA) converts the incoming optical signal into a voltage signal, which is then amplified by a programmable gain amplifier (PGA). The PGA is controlled by the microcontroller using a signal monitor line. This way, the maximum possible gain can be applied without reaching the dynamic range limit of the amplifier.
The amplified signal is then demodulated by a lock-in amplifier circuit using the same PWM signal reference that is used for the modulation of the light sources. After demodulation, the signal is filtered by a 3rd-order Butterworth low-pass and is then again amplified and stabilized before it leaves the NIRS module for analog-to-digital conversion on the mainboard.

In the lower part of the figure, the mainboard unit is depicted. A microcontroller unit administrates the operation of the instrument corresponding to the user inputs. It sends the control signals for up to four NIRS modules and reads the corresponding digitized values via SPI interface from a $16\,Bit$ 4-channel analog-to-digital converter (ADC).

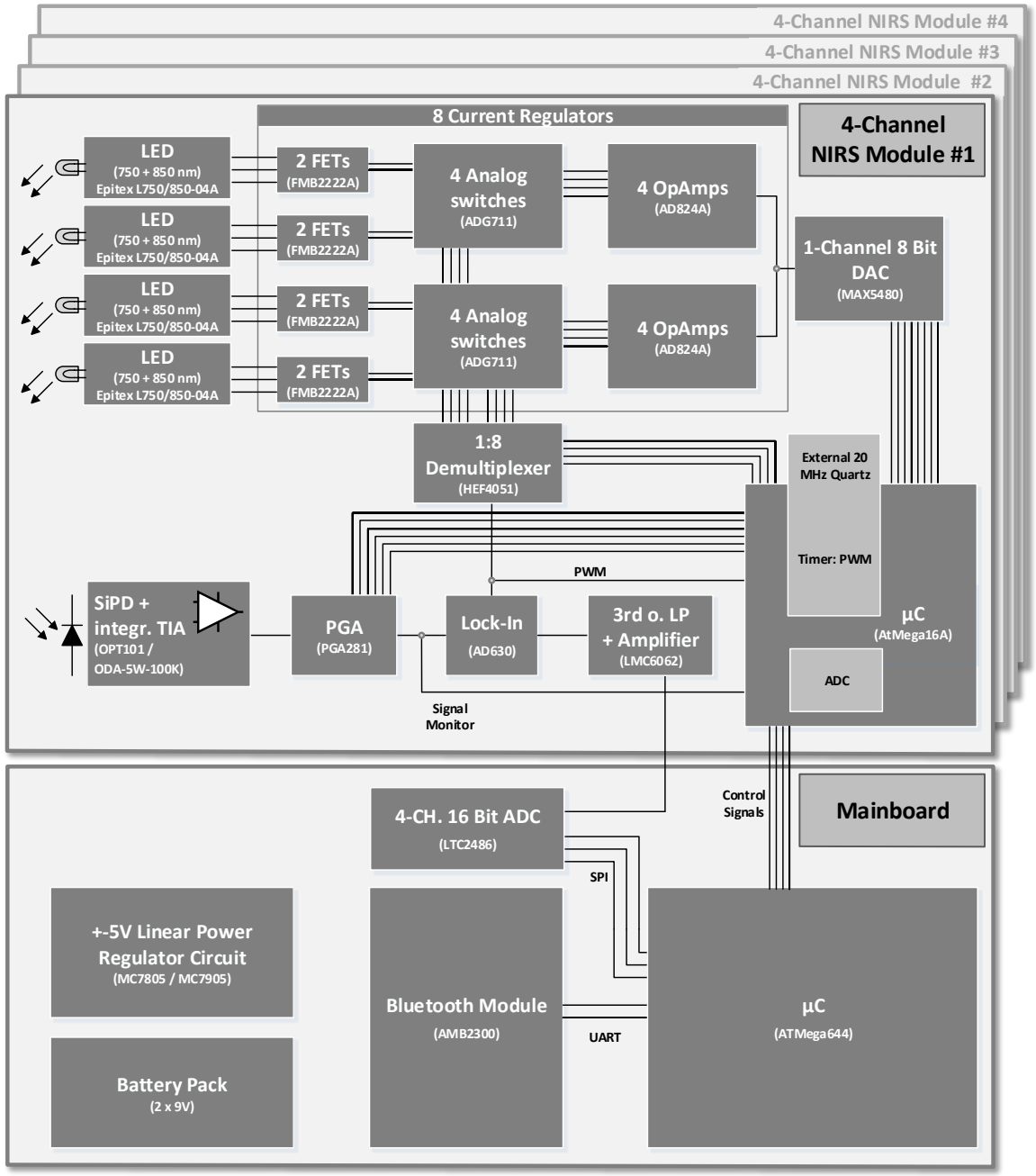

Figure 3.3: Detailed system concept of the developed CW fNIRS system.

The digitized values are then assigned to their correct channel and wavelength, further operational information is added and the complete data block is sent via UART to a Bluetooth module. The Bluetooth module works in transparent mode and simulates a common RS232 interface, sending the data to the PC where it can be saved and evaluated. Also on the mainboard, a stabilized linear power regulator circuit provides a $\pm 5\,V$ power rail for the NIRS modules. The two $9\,V$ (at least $7.5\,V$) inputs for the power regulator circuit come from battery packs that can be chosen at will.

3.4 Hardware Design NIRS Module

In this section, the detailed implementation of the system concept's NIRS module elements is described. To do so, the functional units are viewed individually, implemented under consideration of the findings in earlier sections and were built upon another using the results of evaluation and testing of 3 prototype versions. Fig. 3.4 shows two main results of the NIRS module development process.

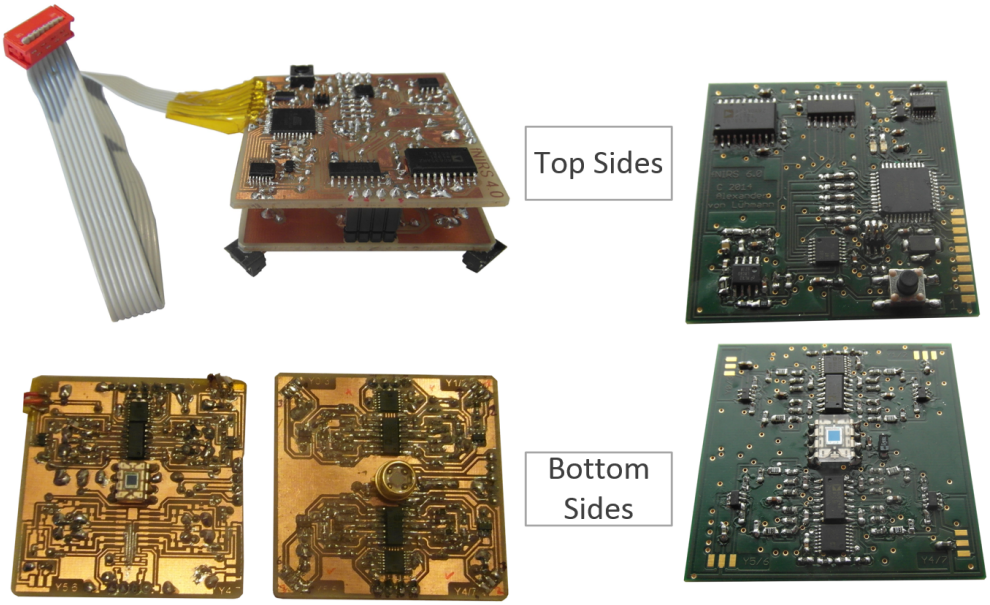

Figure 3.4: NIRS module design steps. Left: prototype with exchangeable sensor PCB, right: final version.

In the prototype version (left), the NIRS module itself is built up from two modules that are plugged onto each other, allowing evaluation of different detector types. On the right, the final 4-layer PCB version of the NIRS module is shown. In the following, the hardware design of this module will be discussed in detail based on excerpts of the final hardware schematics. For the complete schematics, please refer to the appendix figs. A.3 and A.4.

3.4.1 NIR Light Emitter

As described in section 2.5 and contrasted in tab. 2.2, only laser diodes (LD) and light emitting diodes (LEDs) can be used for a mobile and compact instrument.
LDs have the advantages of very sharp radiation peaks and high intensities which are desirable for high-quality fNIRS signal generation. On the other hand, their disadvantages (high heating problems, higher safety demands, large packaging, high costs and limited wavelength availability) forbid the usage of LDs in this mobile context and prioritize LEDs. As LEDs are small, comparatively cheap, a greater variation of NIR wavelengths is available, and the heating problems are less critical in the case of direct application to the head, they were judged more fitting for the design of this instrument.
Another very important advantage of LEDs for direct application on the head is the availability of multi-wavelength packages. Using the modified Beer-Lambert Law, it is

implicitly assumed that both interrogating wavelengths enter the tissue at the same spatial location to ensure the interrogation of the same partial tissue volume by both beams. So far, no multi-wavelength laser diodes with suitable NIR wavelengths were found. The use of multiple single-wavelength emitters makes optical fiber guides necessary to bring both signals together to a single output location. The use of optical fibers, however, does not fit the objective of this work.

For the multi-wavelength LED light sources, the two optimal NIR wavelengths had to be determined. As mentioned before, an optimal choice of the wavelength pair in the optical window is crucial for signal sensitivity and minimal crosstalk.
Generally, it is necessary to choose one wavelength above and one wavelength below the isobestric point of 805 nm in HbR and HbO absorption coefficients [20, 21] (see fig. 3.5).

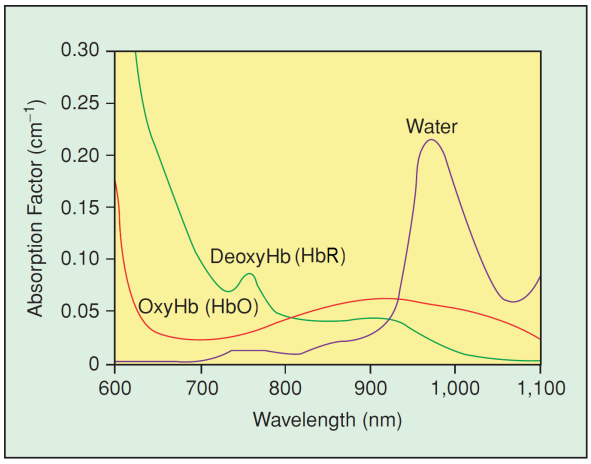

Figure 3.5: Absorption Coefficients of HbR, HbO and Water, taken from [14].

Left and right of the point at 805 nm, near isobestric wavelengths are commonly used to minimize absorption artifacts due to the presence of compounds other than hemoglobin [21]. To further narrow down the optimal wavelength pair, published investigations on the wavelength selection optimization problem, as well as the wavelength selections in NIRS instruments from both research and commercial developments were evaluated and summarized (see Appendix tab. A.3).
A commonly used wavelength is 830 nm, as the hemoglobin absorption spectra change little in the range of $830 - 900\,nm$ and the sensitivity of photo multiplier tubes (which were, as noted before, used for many of the first NIRS instruments) decreases rapidly above 840 nm [67]. Based on this early determination, many of the later investigations used 830 nm as a constant:

- Using an error propagation approach, Yamashita et al. [68] concluded that 830 nm together with $< 780\,nm$ is optimal.
- Using the Monte Carlo Method (Strangman), and empiric SNR tests (Sato), Yamashita, Sato and Strangman et al. [66, 68, 69] concluded that 830 nm with 690 nm or 760 nm minimize random and systematic errors.
- Using the Monte Carlo Method for minimizing crosstalk, Okui et al. [70] came to the conclusion that 830 nm with $690 - 750\,nm$ are optimal.

Uludag et al. [71], however, stated that $830\,nm$ is not the optimal wavelength and that > 730 and $< 720\,nm$ with both not $> 780\,nm$ should be used.
Finally, based on a three-layer model analysis, Correia et al. [72] concluded that $887 \pm 12\,nm$ and $704 \pm 7\,nm$ are optimal.

Table A.3 (see appendix) shows an overview of the wavelength pairs chosen in research and commercial NIRS instruments as well as the above-outlined results from theoretical investigations.

Based on this work, the wavelength pair $760 + 850\,nm$ was selected. Because of temporal non-availability in low amounts of LEDs with this wavelength configuration, alternatives had to be found and were compared (see A.10, appendix). As the best alternative, a $750 + 850\,nm$ LED from Epitex (L750-850-04A) in a $5\,mm$ molded package was selected and supplied by Meuvo-Technik Austria. The distance between both emitters in the LED is $< 1, mm$ and therefore negligible in this application context. Tab. 3.1 depicts the most important technical characteristics.

L750-850-04A	**750 nm**	**850 nm**
Maximum Power Dissipation	$200\,mW$	$160\,mW$
Typical Total Radiated Power ($I_F = 50\,mA$)	$15\,mW$	$18\,mW$
Max. Forward Current	$100\,mA$	$100\,mA$
Half Width $\Delta\lambda$ ($I_F = 50\,mA$)	$30\,nm$	$35\,nm$
Viewing Half Angle $\Theta_{1/2}$	$\pm 20\,deg.$	$\pm 20\,deg.$

Table 3.1: Epitex L750-850-04A characteristics.

3.4.2 NIR Light Sensor

Based on the comparison of photomultiplier tubes (PMTs), silicon photo diodes (SPDs) and avalanche photo diodes (APDs) (table 2.3, section 2.5), silicon photo diodes were selected for light detection in the fNIRS system. Because of their size and cost, PMTs are not a possibility for mobile devices. Although APDs can be used in principle, the necessity of high-voltage supply and cooling makes them less suitable for this application with regard to safety aspects and direct head attachment.
The very small packaging, high dynamic range and speed, together with low-voltage operation makes SPDs the best choice for mobile and adaptive lock-in amplification purposes. Another advantage is that they can be applied directly to the skin surface, which is the most efficient method of collecting the light [21]. The main disadvantage of SPDs is their low sensitivity due to a lack of internal gain. To minimize this drawback, only SPDs with integrated trans-impedance amplifiers (TIA) were taken into account during the investigation of available components. Using integrated and fitted TIAs should minimize noise pickup during the highly sensitive pre-amplification of the signal and compensate for the missing internal gain as much as possible.

Tab. 3.2 shows the most important characteristics of SPDs with integrated TIA that were available.
Due to the lock-in modulation of the optical signal, a bandwidth of several kHz is necessary. Therefore, some of the available SPDs are not suitable for lock-in purposes. From the remaining detectors, two were selected with respect to maximal sensitivity and minimal noise: ODA-5W-100K and OPT101. While the OPT101 has a ten times higher sensitivity, the ODA-5W-100K has a very high bandwidth. With OPT101 as favorite, both SPDs were tested in the further development process.

Model	Min. Supply Voltage $[V]$	TIA Gain $[\Omega]$	Typ. Sensitivity @ 850 nm $[V/\mu W]$	Max. Dark Offset $[mV]$	Typ. Dark Offs. Noise $[\mu Vrms]$	Cutoff Freq. $-3dB\,[kHz]$
ODC. ODA-5W-100K	±5	$100\,k$	0.056	±1	477	800
ODC. ODA-6W-100M	±5	$100\,M$	56	±2	198	1
ODC. ODA-5W-500M	±5	$500\,M$	267	±2	500	0.315
BB OPT101	+2.7	$1\,M$	0.6	+10	300	14
BB OPT301	±2.25	$1\,M$	0.47	±2	160	4
API SD112-42-11-221	±5	$100\,k$	0.0558	±1	60	750
API SD112-43-11-221	±5	$75\,M$	45	±3	20	1

Table 3.2: Silicon photo diodes with integrated TIA. ODC: Opto Diode Corp., BB: Burr Brown, API: Advanced Photonic Inc.

The OPT101 is a monolithic photodiode with single supply and integrated TIA operating in the photoconductive mode with an $1\,M\Omega$ feedback resistor and it has an effective sensing area of $2.29 \cdot 2.29\,mm^2$. Figure 3.6 shows the internal wiring and spectral responsivity curve.

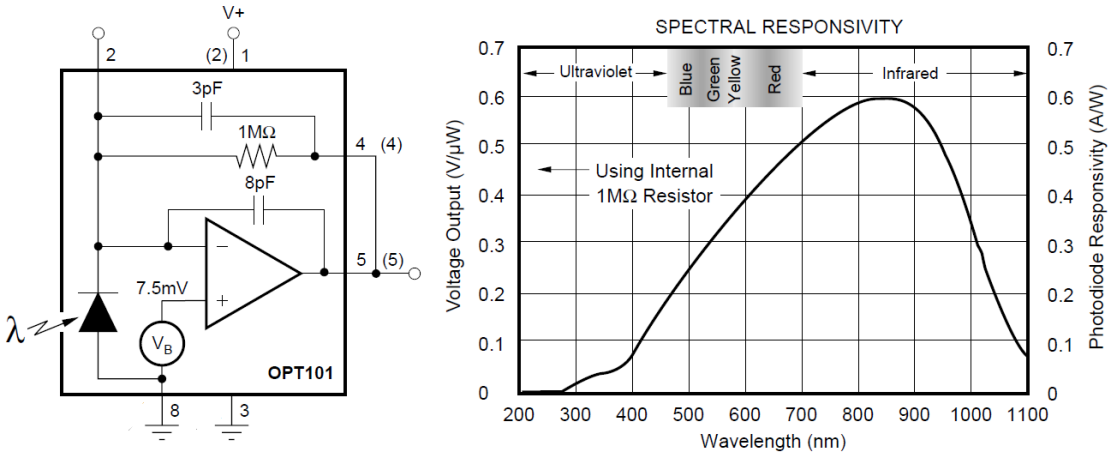

Figure 3.6: OPT101 interior circuit and spectral responsivity curve, taken from OPT101 datasheet.

3.4.3 Amplification, Lock-In Modulation and Demodulation

As the NIRS signal is a very weak optical signal that can easily be drowned in noise during the extraction process, a lock-in approach was chosen for the system design. Lock-in amplification or phase-sensitive detection is a widely-used method for the recovery of weak signals masked by a strong noisy background, and can be found in many spectroscopic applications. In the following, the concepts of lock-in recovery will be briefly introduced to build a basis on which the system design can be further elaborated. For additional information on lock-in recovery, see for example the fundamental work of Meade [73, 74] which is also basis for the following explanations.

Lock-in amplifiers are based on the concept of phase-sensitive detection. Phase-sensitive detection is the demodulation of an ac signal with a common reference waveform. Demodulating the signal with the same reference waveform that was used for modulation, the phase-sensitive detector is only sensitive to signals coherent with the reference (same frequency and phase) and rejects others. Thus being an extremely narrow-band bandpass filter, it significantly enhances the signal-to-noise ratio (SNR):
Lock-in amplification results in large rejection of ambient room lighting sources, dark current of the photodetector, amplifier offsets and also of $\frac{1}{f}$ amplifier noise, implied that the signal is modulated at a fixed frequency in the kilohertz range, where the amplifier noise is significantly lower than at near zero frequency.

The mathematical description of this principle is quite straightforward:
Let $s(t)$ be the modulated signal carrying signal information in its amplitude $V_S(t)$ and $r(t)$ be the reference with constant amplitude V_R both with frequency ω and phase Φ

$$s(t) = V_S(t) \cdot \cos(\omega_S t + \Phi_S), \tag{3.10}$$

$$r(t) = V_R \cdot \cos(\omega_R t + \Phi_R). \tag{3.11}$$

Then demodulation (multiplication) of signal and reference yields

$$v(t) = \frac{V_S(t)V_R}{2} \cdot (\cos[(\omega_S + \omega_R)t + \Phi_S + \Phi_R] + \cos[(\omega_S - \omega_R)t + \Phi_S - \Phi_R]). \tag{3.12}$$

In case that signal and reference have the same frequency $\omega = \omega_S = \omega_R$ and a low-pass filter $A_L(\omega) = |H_L(j\omega)|$ is applied with cut-off frequency $f_c \ll \omega$, $A_L(0)$ being the magnitude of the filter response at zero frequency, the slow dc signal with frequency components $\ll f_c$ after filtering yields

$$v_{LP}(t) \approx \frac{V_R A_L(0)}{2} V_S(t) \cdot \cos(\Phi_S - \Phi_R). \tag{3.13}$$

$\cos(\Phi_S - \Phi_R)$ is the attenuation factor based on the phase between incident and detected optical signal and is mainly determined by the propagation delays of hardware components in the signal path.
In practice, the reference signal is often a square wave instead of a sine wave. In that case, the demodulation can be done simply by multiplication of the incoming signal with ± 1. Fig. 3.7 depicts this case.

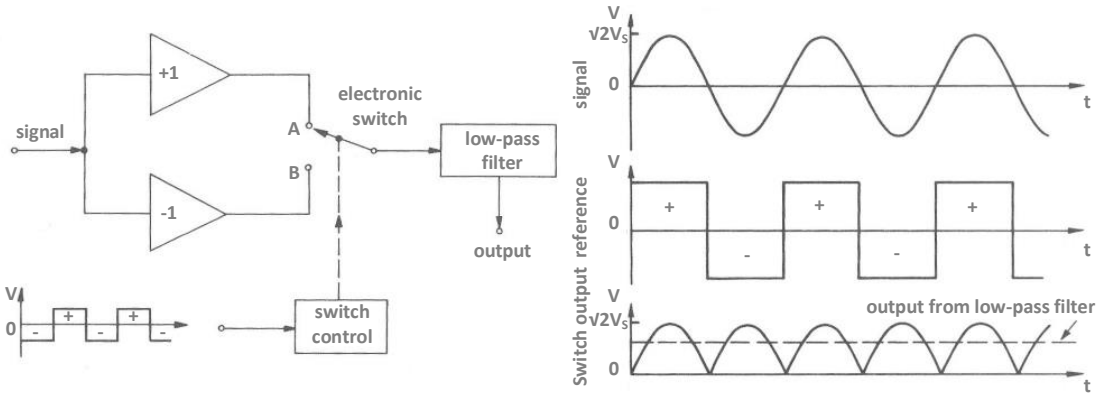

Figure 3.7: Principle of squarewave lock-in amplification, fig. taken from [73].

Using the same signal s(t) from eq. 3.10 now with a Fourier representation of the square wave reference r(t) for demodulation

$$r(t) = \frac{4}{\pi}[\cos(\omega_R t + \Phi_R) - \frac{1}{3}\cos(3(\omega_R t + \Phi_R)) + \frac{1}{5}\cos(5(\omega_R t + \Phi_R)) - ... \tag{3.14}$$

the resulting demodulated signal yields

$$\begin{aligned} v(t) = \frac{2V_S(t)}{\pi} \cdot [\cos(\omega_R t \pm \omega_S t + \Phi_R \pm \Phi_S) - \frac{1}{3}\cos(3\omega_R t \pm \omega_S t + 3\Phi_R \pm \Phi_S) \\ + \frac{1}{5}\cos(5\omega_R \pm \omega_S t + 5\Phi_R \pm \Phi_S) - ...]. \end{aligned} \tag{3.15}$$

Again, when the signal and reference have the same frequency $\omega = \omega_S = \omega_R$ and a low-pass filter $A_L(\omega) = |H_L(j\omega)|$ with cut-off frequency $f_c \ll \omega$, $A_L(0)$ being the magnitude of the filter response at zero frequency, is applied, the slow dc signal with frequency components $\ll f_c$ after filtering is

$$v_{LP}(t) \approx \frac{2V_R A_L(0)}{\pi} V_S(t) \cdot \cos(\Phi_S - \Phi_R). \tag{3.16}$$

As can easily be seen, the responses of the "ideal" sinusoidal synchronous detector (3.13) and the square wave reference detector (3.16) differ only in a constant scaling factor with the square wave excitation providing a 27% larger signal. "The essential difference in this case is that the phase-sensitive detector will also give a phase-sensitive dc output in response to signals at frequencies $3\omega_R$, $5\omega_R$, etc. A detection system with this property is said to be harmonically responding" (p. 35, [73]).
It has to be pointed out that this harmonic response is effective both on higher harmonics in the signal as well as on noise. The degradation by noise is, however, not as great as one could assume. As the noise in each additive term is random and not correlated with the signal, it "adds power only as the square root of its magnitude in each term, whereas the signal gained adds arithmetically" [75].
Again, the term $cos(\Phi_S - \Phi_R)$ is the attenuation resulting from a phase between the incident and the detected optical signal and is mainly determined by the propagation delays of hardware components in the signal path. A high delay results in a significant attenu-

ation of the signal during demodulation. Thus, all hardware elements in the signal path were chosen with respect to their speed/delay properties. A mathematical estimation and measurement of the real attenuation effects resulting from phase delay will be presented in subsection 4.1.4.

In the NIRS module, a $3.125\,kHz$ square wave reference is produced by the PWM module of the microcontroller and is used for both modulation of the light sources and demodulation of the amplified detector signal. Fig. 3.8 depicts the application of lock-in amplification in the module.

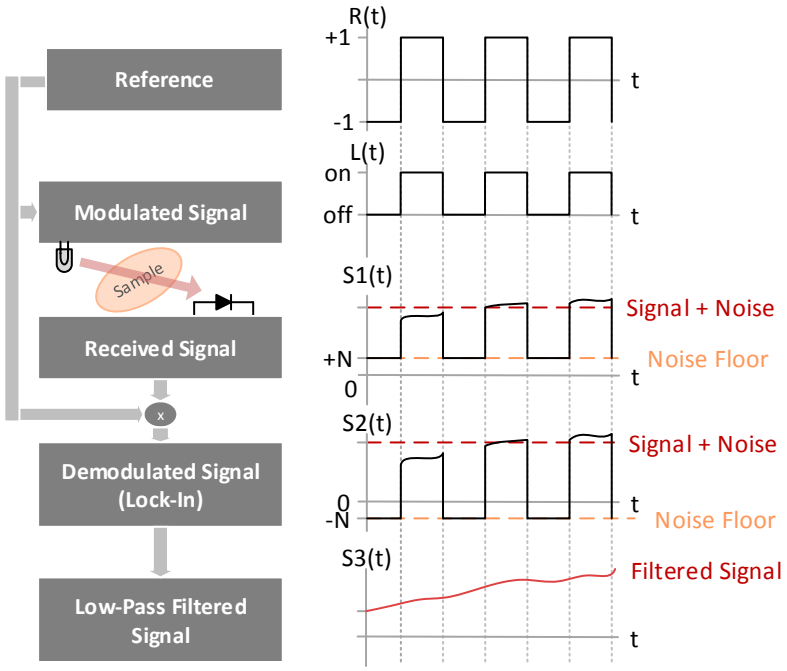

Figure 3.8: Principle of lock-in amplification in NIRS module.

The microcontroller PWM reference modulates the active channel's LED. The hardware details of this modulation are described in the next subsection on current regulators. The square wave optical signal is then sent into tissue for interrogation. On the detector side, the optical signal is received and amplified, now carrying both functional NIRS information and noise from stray light, dark current, amplifier noise and offset. This noise floor exists in both halves of the duty cycle: The active part carrying NIRS information (LED on), as well as the inactive part (LED off). Demodulating this signal with the PWM reference inverts the part of the signal only carrying the noise floor to a negative voltage level. Low-pass filtering the demodulated signal removes the high-frequency component, thereby integrating positive and negative voltage signals. Simplifying but vividly speaking, the low-pass filter subtracts the noise floor during LED-off times from the signal and noise during LED-on times. The lower the filter's cut-off frequency (respecting the physiol. signal's freq. spectrum), the narrower the lock-in bandwidth and thus the better the SNR.

For the actual lock-in demodulation, an integrated analog high-precision balanced modulator/demodulator circuit from Analog Devices was chosen.

The AD630 provides a $350\,kHz$ full-power bandwidth, $45\,V/\mu s$ slew rate, $-120\,dB$ crosstalk at $1\,kHz$ and a maximum channel offset voltage of $100\,\mu V$. It has been successfully used in low-cost laboratory lock-in applications [76] and in compact four-quadrant amplifier applications [77].

Figure 3.9 shows the hardware implementation of the complete detector amplification unit on the NIRS module.

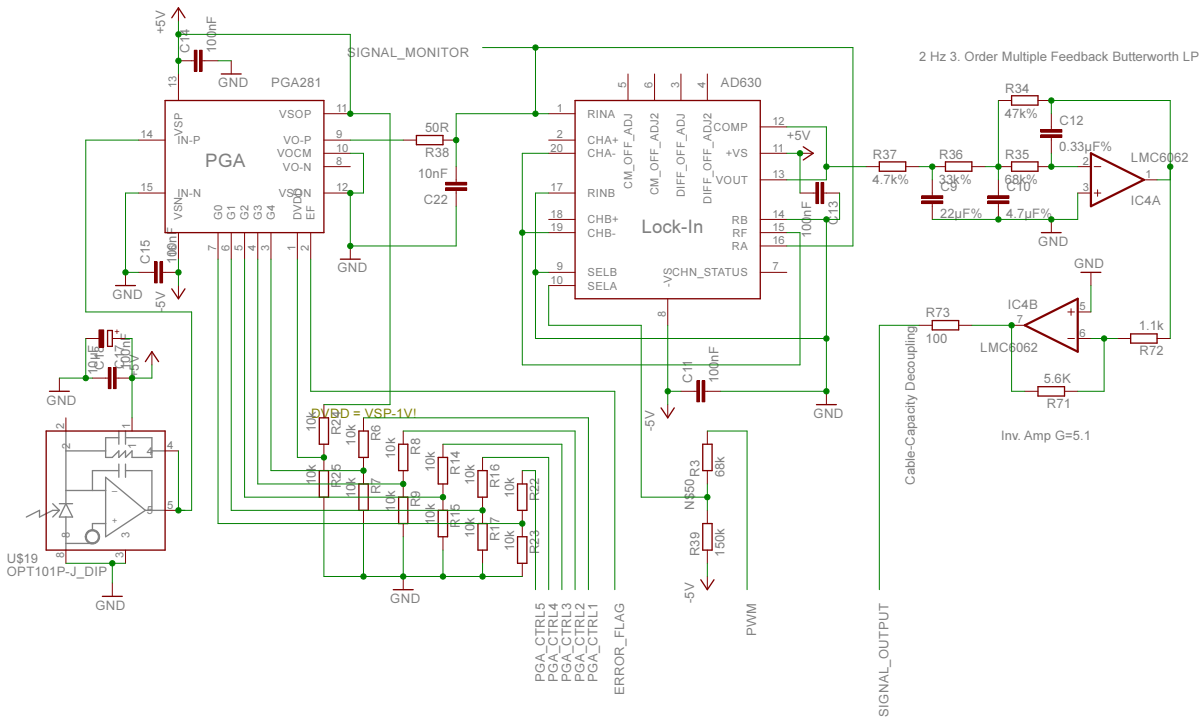

Figure 3.9: Hardware implementation of lock-in amplification.

On the bottom left, the OPT101 photodiode and integrated TIA detect and pre-amplify the optical signal. This signal is then fed into a programmable gain amplifier (PGA) for further amplification.
For this purpose, the high-precision instrumentation PGA281 from Texas Instruments was chosen. It provides near-zero long-term offset voltage and gain drift, very low $\frac{1}{f}$ noise of $420\,nV_{pp}$ at $f = 0.01 - 10\,Hz$, excellent linearity of $1.5\,ppm$ and binary gain steps from $\frac{1}{8}\,V/V$ to $176\,V/V$. As the digital supply voltage and gain control logic levels have to be lower than the input and output stage power supply levels due to internal design specifications of the PGA281, voltage dividers are applied to scale the digital logic levels from $+5\,V$ VDD down to $2.5\,V$ DVDD.
The amplified signal is then filtered with a passive RC output low-pass filter (R38 and C22) for removal of a minimal residual amount of high-frequency switching noise coming from the internal chopper stabilized architecture.
The filtered signal is monitored by the microcontroller (not in the picture) using a SIGNAL_MONITOR line and the PGA281 error flag line (EF) to enable gain adaption in case the signal reaches the dynamic range limit of the amplifier.

Now, the AD630 modulator/demodulator circuit demodulates the signal using the PWM reference from the microcontroller unit. In the internal design of the AD630, a voltage-sensitive comparator selects one of two input stages (inverting/non-inverting) based on the sign of the reference signal at the SELA pin. As the PWM signal is only positive or zero, a negative offset is applied by a voltage divider (R3, R39), shifting the 0 to +5V reference to a level 1.6V below zero, thus enabling the comparator to switch according to the PWM cycles.
The demodulator circuit is pin-configured with a gain of ± 2 to compensate for the factor $\frac{1}{2}$ resulting from the demodulation (see equations (3.13) and (3.16)).
The demodulated signal is then low-pass filtered by a 3rd-order multiple feedback Butterworth filter with cut-off frequency $f_c = 2\,Hz$ and finally inverted and amplified with a gain of $G = 5.1$. To this end, the LMC6062, a dual high-precision, low-offset voltage, micropower operational amplifier by Texas Instruments was selected. The LMC6062 provides a low-offset voltage of $100\mu V$, ultra-low input bias current of $10\,fA$ and operates single supply with ultra-low supply current of $16\,\mu A/Amplifier$. The filter design was simulated and optimized using LTSpice. Fig. 3.10 shows the simulated bode diagram of the filter and amplification unit.

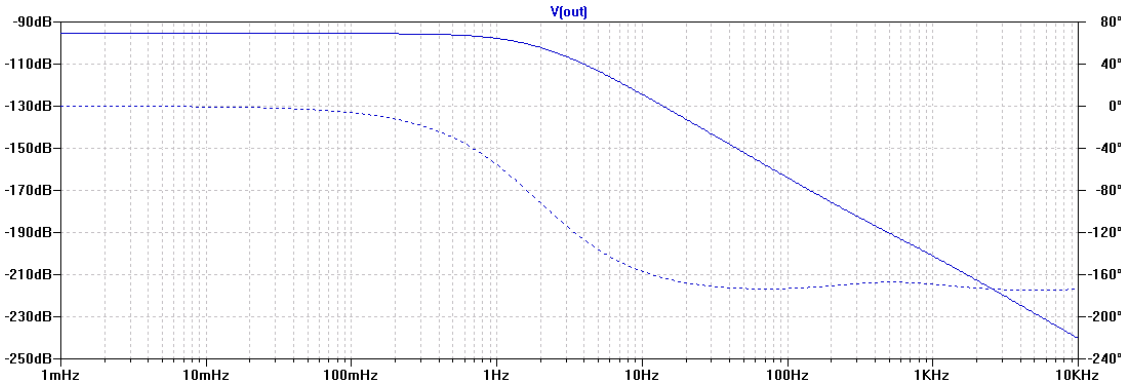

Figure 3.10: Low-pass and amplification bode diagram LTSpice.

The elements in this lock-in amplification unit were sequenced in a way that is thought to optimally utilize the advantages of the phase-sensitive detection technique. As the PGA amplifies the signal before demodulation, not only stray light, dark current and other noise effects during detection and pre-amplification but also offsets and amplifier noise from the process of post-amplification are reduced in the lock-in amplification process.
To keep the resulting signal as clean as possible, high-precision amplifiers are used for low-pass filtering and the final inversion and amplification.

3.4.4 Current Regulators

As mentioned in section 2.5, for high accuracy of the NIRS instrument the intensity of the emitted NIR LED light has to be kept as constant as possible, as emission variations can not be separated from absorbance variations in the signal after detection.
Even though a regulator using the measured emitted optical power as feedback variable would be optimal, the technical implementation of such a regulator increases system

complexity and is usually not necessary (see subsection 4.1.5 for drift evaluation). Thus, current regulators were designed to keep the current through the LED semiconductor junctions constant and independent from variations in supply voltage and temperature. At the same time, the design should be suitable for an adjustment of the current levels as well as square-wave modulation for lock-in purposes. For this, a basic approach proposed by Chenier 2007 [54] (see fig 3.11) was investigated:

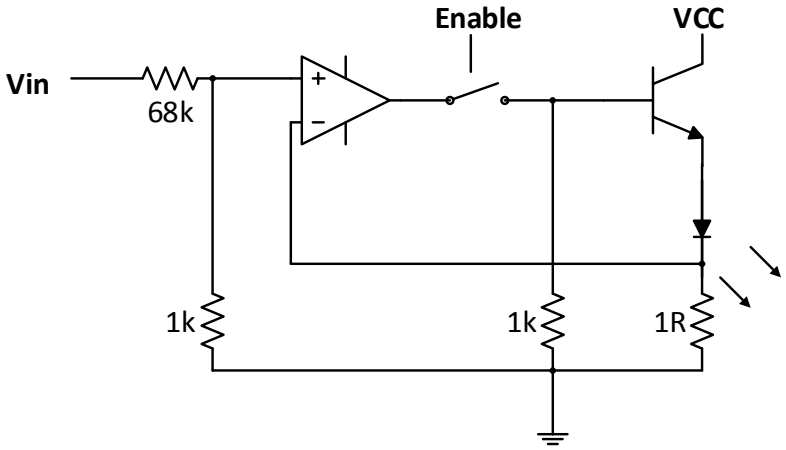

Figure 3.11: Current regulator by Chenier 2007 [54].

A reference input for the current regulation is produced by a voltage divider at the positive input of an operational amplifier (OpAmp). At the negative input of the OpAmp, the voltage drop across an $1\,\Omega$ resistor that is produced by the LED current is measured. Using the fundamental functionality of OpAmps, both potentials are subtracted, creating a difference voltage at the OpAmp output. This voltage controls the base/gate of a transistor, thus regulating the current flowing through it until the difference voltage is zero and the voltage at the positive OpAmp input and at the $1\,\Omega$ resistor are the same. For modulation, an analog switch is inserted between OpAmp output and the base of the transistor. When the switch is opened, the $1\,k\Omega$ pull-down resistor pulls the base to ground, thus closing the transistor.
When the proposed current regulator by Chenier was built and tested, however, it showed unstable and unreliable functionality. Therefore, a significantly changed and iteratively upgraded design is presented in this work (see fig. 3.12).
With the same regulation principle as described above, there are major differences in the design:

- The LED was placed directly at the power supply because of its three-pin multi-wavelength package. Having individual cathodes but a common anode, this was necessary to enable single-wavelength illumination.
- As the instability and unreliability of the design by Chenier was mainly based on the interruption of the closed loop control circuit, the analog switch for modulation was placed at the OpAmp input. With inverted logic (active low switch), the switch pulls the input to ground when the channel is inactive during short (modulation) or long (other channels active) LED-off times. This enables a continuous regulation, only changing the input reference variable.

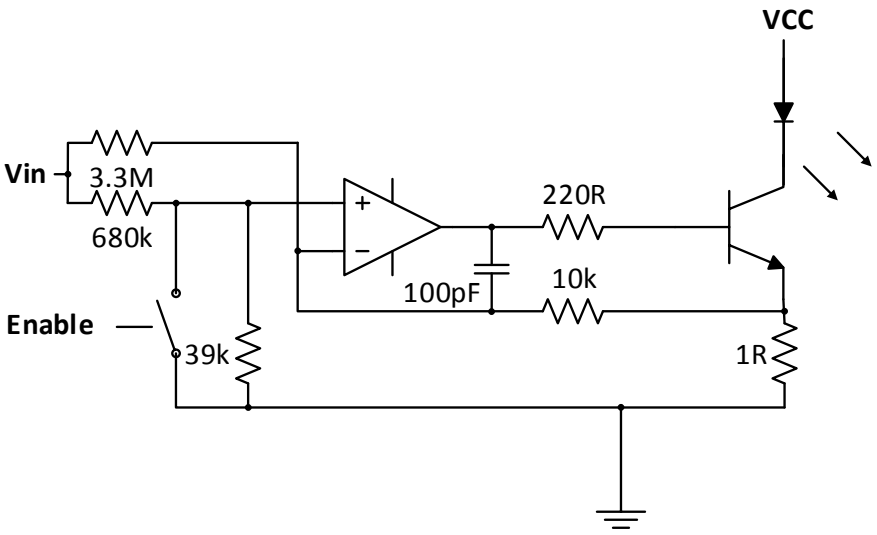

Figure 3.12: Developed and optimized current regulator for NIRS module.

- As the regulator is modulated in the kHz-range, over- and undershoots influence the ideally square-wave shape of the current. To enhance the switching performance, a passive RC negative feedback was added and evaluated (see section 4.1.3) and an output resistor was put between transistor base and OpAmp output to increase transistor gain and thus the effective slew rate.
- Despite the use of a high-precision OpAmp, evaluation of the regulator circuit revealed that during off-times (OpAmp inputs pulled to ground), some LED channels were still weakly illuminated. The small current flow leading to this illumination was found to be due to OpAmp offset voltage. This was corrected by impressing a low negative offset current to the negative OpAmp input with a $3.3\,M\Omega$ resistor that is connected with the reference input voltage V_{in}.

Figure 3.13 shows an excerpt of the hardware implementation on the NIRS module. For the sake of clarity, only two of eight NIRS channels (one multi-wavelength LED channel) are shown.
On the NIRS module, there are eight channels (4 dual wavelength LEDs) with corresponding current regulators. A 8:1 demultiplexer (MUX) is used to select the active channel and current regulator. By configuring the MUX for one channel, the PWM reference signal from the microcontroller is fed through to the corresponding analog switch of the current regulator that is to be activated. As the switches in this application use inverted logic (active low), the high-level part of the PWM duty cycle corresponds with an open switch and therefore an active current regulator/active current. The low part of the PWM cycle closes the switch which pulls the regulator input reference to ground, thereby closing the transistor and stopping the current flow.
For the MUX, the HEF4051B from NXP Semiconductors was chosen from several possibilities. The HEF4051B is an 8-channel analog multi-/demultiplexer with three address inputs, a common input, an active low enable input and eight independent ouptuts. Criteria for the selection of the analog MUX were mainly supply voltage and speed to keep the propagation delay in the signal path as low as possible and thereby minimize attenuation by the lock-in amplification process resulting from phase shifts. The

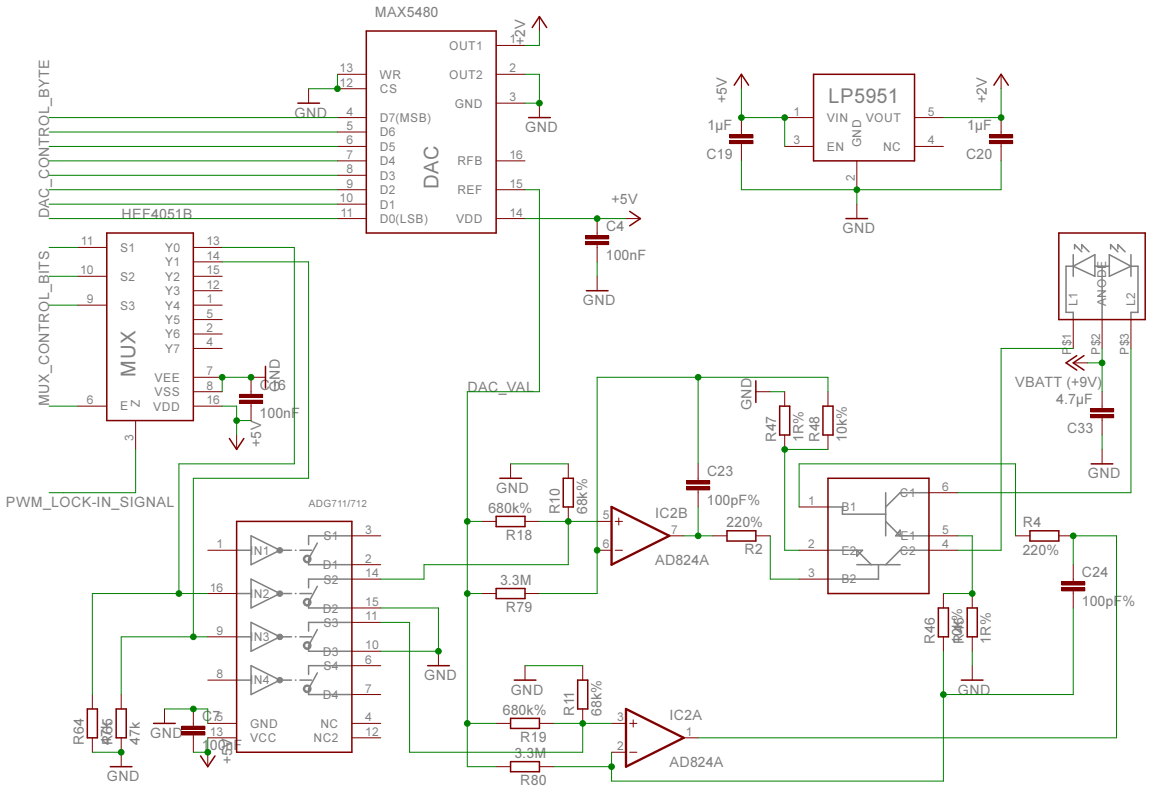

Figure 3.13: Excerpt of hardware current regulator implementation on the NIRS module.

HEF4051B's typical propagation delays for HIGH to LOW and LOW to HIGH propagation are $t_{PHL} = t_{PLH} = 15ns$.
For the analog switches, the low voltage quad CMOS switches ADG711 from Analog Devices were used. Providing four analog switches in one small TSSOP package, low on resistance of typ. 2.5Ω, low power consumption ($< 0.01\mu W$) and fast switching times ($t_{on} = 16ns$, $t_{off} = 10ns$), these switches fitted the requirements best. Again, criteria for the selection of the ADG711 were speed, supply voltage and power consumption. While in first design protoypes, based on the approach of Chenier 2007, the ADG712 with non-inverted logic was used, in the final NIRS instrument the ADG711 with inverted logic is used in the way described above. To keep the switch control inputs at defined logic levels during high-impedance output of the MUX (channel deactivated), pulldown resistors (R64, R65) are applied.

To adjust the NIR LED intensity, the current of the regulators is controlled by the reference voltage input that is produced by an $8\,Bit$ digital-to-analog converter (DAC). This DAC is configured by the microcontroller unit. At this time, four different LED power/current levels are implemented ($25\,mA$, $50\,mA$, $80\,mA$ and $100\,mA$). To this end, the MAX5480 $8\,Bit$ parallel DAC by Maxim Integrated Products was selected. It provides single supply operation, low power consumption of max. $100\,\mu A$ and a linearity of $\pm 1/2\,LSB$ over temperature in a small QSOP package. For use in voltage output mode, a reference input of $VDD - 3V, max$ has to be provided. This reference is generated by a micropower $2\,V$ buffered low-dropout CMOS voltage regulator (LDO) LP5951.

For the actual current regulators, two high-precision quad operation amplifiers, LMC6064 (Texas Instruments) and AD824A (Analog Devices), were used and evaluated (see section 4.1.3) with the AD824A showing the best characteristics due to a much higher slew rate and thus a higher edge steepness of the square-wave current signal. The AD824A is a quad, single supply, low power, rail-to-rail, FET Input OpAmp with very low input bias current of $2\,pA$, wide bandwidth of $2\,MHz$, a slew rate of $2\,V/\mu s$ and a low offset voltage of typ. $0.1\,mV$.
For the transistors in the current regulator design, general purpose FMB2222A npn arrays by Fairchild Semiconductor are used. In the FMB2222A, two transistors come in a tiny SuperSOT6 package, which allow a maximum continuous collector current of $500\,mA$ and a total power dissipation of $700\,mW$ with good switching characteristics (typ. delay time $t_d = 8\,ns$, rise time $t_r = 20\,ns$, fall time $t_f = 40\,ns$).

For the implementation of 8 NIRS wavelength channels on one module, one HEFB4051B MUX, two analog switch packages ADG711, one DAC MAX5480, two quad, high-precision amplifiers AD824A and four FMB2222A npn arrays are used.

3.4.5 Microcontroller Unit

An AtMega164A microcontroller from Atmel Corporation is used for PWM signal generation, control of MUX, DAC, PGA and for communication with the NIRS mainboard. The AtMega164 is a high-performance, multipurpose, low-power, $8\,Bit$ microcontroller with a $16\,kBytes$ in-system programmable flash memory, based on advanced RISC architecture. As the software design for the NIRS module microcontroller unit is described in subsection 3.7.1, only one important hardware design aspect will be further discussed at this point:
For the generation of the lock-in PWM square-wave reference, the built-in PWM channel is used with a 50% duty cycle at $3.125\,kHz$. As the internal $8\,MHz$ RC oscillator of the microcontroller provides only low precision in oscillation stability, a significant jitter can be observed in the spectral analysis of any produced kHz oscillation. For higher precision and to reduce this jitter, an external $20\,MHz$ crystal (type NX5032) is used for clock cycle generation of the AtMega164A. Wiring the microcontroller with an external crystal, its load capacity and the capacities of the conductor paths (strip lines) have to be regarded and additional capacities (C1, C2) have to be added for compensation (see fig. 3.14).

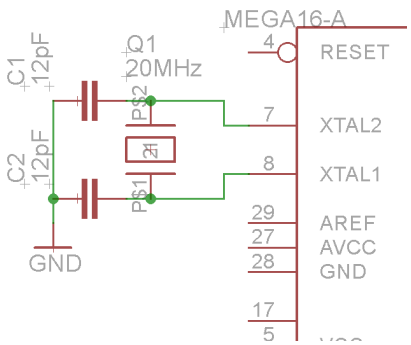

Figure 3.14: External clock source: crystal and capacities.

Using the expertise of a big online microcontroller community [78], the capacities were designed to be $12\,pF$ each with

$$C_1 = C_2 = 2 \cdot C_L - (C_P + C_I) \tag{3.17}$$

C_L being the load capacitance of the crystal, C_P the capacity of conductor paths, C_I the capacity of the microcontroller ports and $C_P + C_L \approx 5\,pF$.

3.4.6 General Remarks on Layout and Design

Generally, during the layout of the prototype and final PCB versions, much attention was paid to follow good design practice for measurement instrumentation design. Every supply pin of integrated components such as the microcontroller, photodetector, etc. is buffered with a $100\,nF$ capacity placed as closely as possible to minimize effects of power supply noise and fluctuations.
At the common anode of the NIR LEDs, $4.7\,\mu F$ capacitors are placed to buffer current peaks for the rising and falling edges during PWM current modulation.
To provide a stable ground (GND) potential without ground loops, shield top from bottom layer influences and vice versa, and to minimize effects on the supply voltage (VCC) during changes of load, a complete GND and VCC plane each are provided in a 4-layer PCB layout (see fig. 3.15).

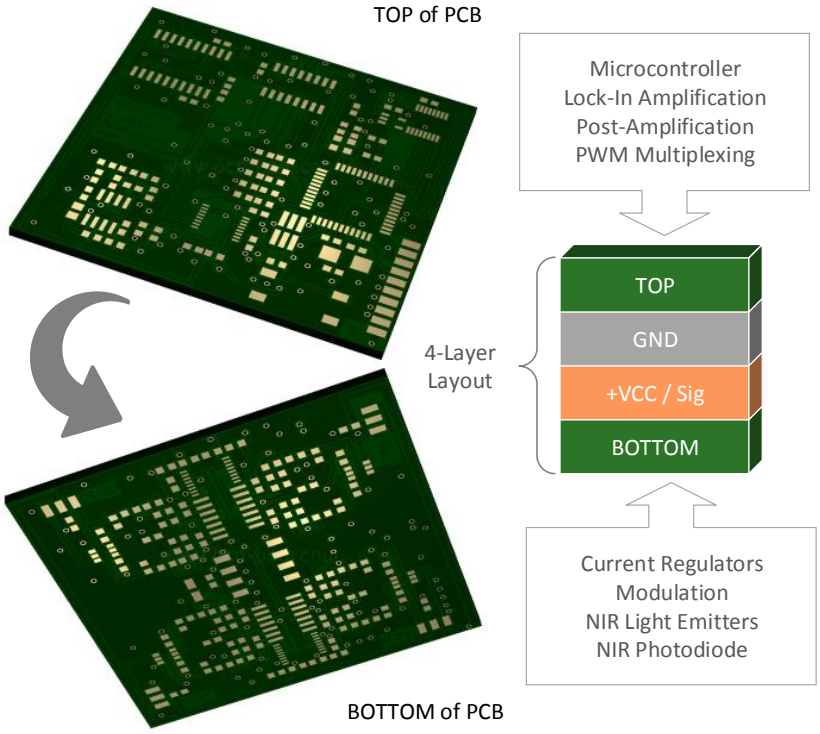

Figure 3.15: Layout of the NIRS module (using a PCB preview from www.pcb-pool.com).

Furthermore, functional units were separated to minimize electrical crosstalk:
With one exception, only the 8 current regulator circuits are placed on the bottom layer of the PCB. For detection of the optical signal, the OPT101 photodiode is also placed on the bottom layer and surrounded by regions on GND potential to shield from current regulator influences.
Electromagnetically isolated by the mid GND and VCC planes, the rest of the components is placed on the top layer. Thus, especially post-amplification, lock-in demodulation and filtering processes are shielded against electrical noise from current modulation processes. Sensible signal lines on all layers were routed as far away from potential noise sources as possible.
The complete layout of the fNIRS module is depicted in figs. A.5 and A.6 in the appendix.

3.5 Hardware Design NIRS Mainboard

In this section, the detailed implementation of the system concept's NIRS mainboard elements will be described. To do so, the functional units are viewed individually and implemented under consideration of the findings in earlier sections and using the results of evaluation and testing of 3 prototype versions that were designed in the course of this work.
For the full schematics, please refer to figs. A.7 and A.8 in the appendix.

3.5.1 Power Supply

All elements and integrated circuits on the NIRS module and mainboard were selected for low-voltage symmetric operation. To supply the NIR light emitters, detector, amplifiers, conversion and communication units with power, a dual $\pm 5\,V$ power supply was designed for the mainboard.
For mobility and safety reasons, batteries are used as power source. This has another great advantage: Since no rectification and filtering is necessary to get a clean dc output, the overall complexity of the power supply design is reduced.

An estimation of the maximum peak currents resulted in a minimum current of $200\,mA$ (consisting mainly of $100\,mA$ for the LED emission unit and $60\,mA$ for the Bluetooth module), that needs to be supplied without significant drop of the supply voltage.
As the availability of negative voltage, low-dropout regulators ($-5\,V$ rail) in this power range is very limited, common fixed-voltage regulators are used. Regarding efficiency, these are in fact not the optimal choice for battery-powered applications but were the best compromise so far. Step-down regulators were not considered as an alternative to preclude possible noise/error influences resulting from the high-frequency chopping process.

The dual power supply design that was implemented for the NIRS instrument (see fig. 3.16) is based on MC7805 and MC7905 $1\,A$ positive and negative voltage regulators from ON Semiconductor and the design considerations in the MC7900 and MC7800 series datasheets.
To ensure good high-frequency characteristics ($3\,kHz$ LED modulation) and stable operation under all load conditions, $10\,\mu F$ bypass tantalum capacitors with low internal impedance at high frequencies are placed directly at the regulator inputs. Further $100\,nF$

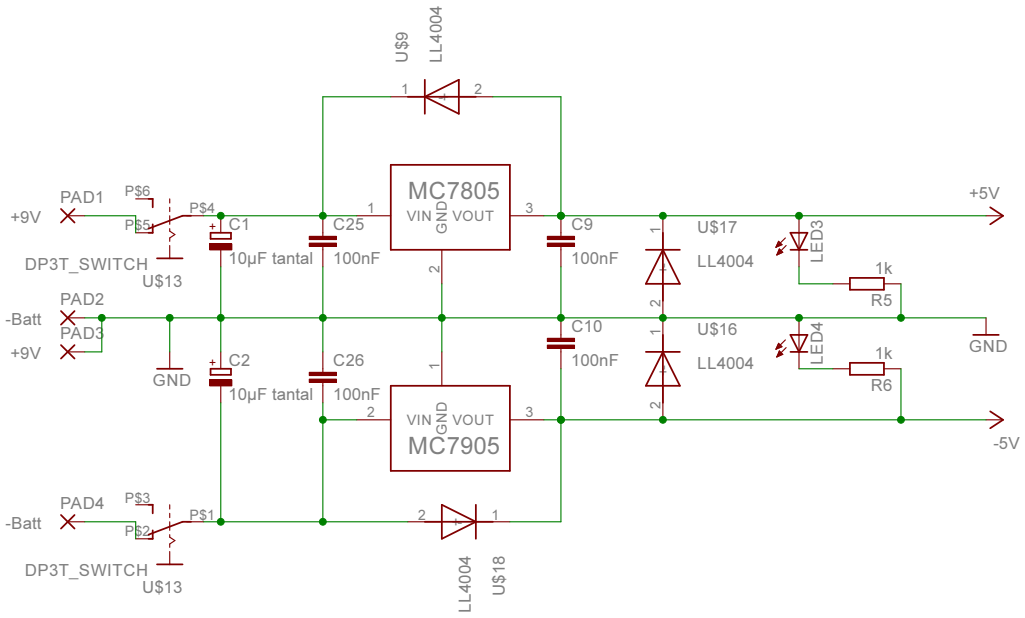

Figure 3.16: NIRS power supply.

bypass capacitors are placed at the in- and outputs.
For opposite polarity and reverse-bias protection, 1N4001-equivalent LL4004 diodes are used in the design.

For the input power supply rails, any battery (packages) with $> 7.4\,V$ can be used. In the first prototypes, $9\,V$ NiMh batteries were applied, enabling about 2 hours of continuous use. The final version of the instrument operates on two $6 \cdot 1.5\,V$ AA battery packages, allowing continuous usage for approximately 10 hours. A more expensive but possibly good alternative optimizing usability aspects (capacity, weight and recharging characteristics) would probably be the use of Li-Ion/Li-Polymer-battery packages from rc-car/hobby applications.

3.5.2 Analog-to-Digital Conversion

The NIRS mainboard provides four slots for NIRS modules. Thus, a total of 16 channels can be used. Even though the channels are time-division multiplexed and hence four NIRS channels of one module require only one analog-to-digital conversion (ADC) unit, four different physical lines have to be taken into account when all modules are to be used.
At the same time, high dc accuracy and quantization depth are necessary for a high-quality digital fNIRS signal representation.

For this reason, the LTC2486, a $16\,Bit$ 4-channel sigma-delta ADC from Linear Technology with integrated temperature sensor and $50/60\,Hz$ line-frequency rejection and very low noise ($600\,nV\,RMS$) was selected.
The LTC2486 provides a 4-wire SPI interface for configuration and data readout and an integrated 4-channel analog MUX. Using this integrated multiplexer, all four analog NIRS module lines can be digitized by one ADC.

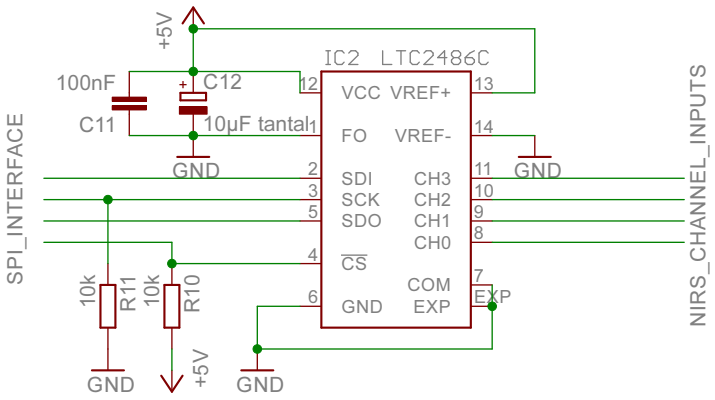

Figure 3.17: Analog-to-digital conversion (LTC2486).

To decouple the ADC from power supply variations, the VCC supply pin is stabilized by a $10\,\mu F$ tantalum bypass capacitor in parallel with a $100\,nF$ capacitor as recommended by the manufacturer.
Because of the high accuracy and internal noise rejection techniques and using an internal oscillator, the ADC allows a maximum sampling rate of $15\,Hz$. Even though the NIRS signal is a very slow dc signal (see section 2.2) and low sampling rates are therefore often sufficient, this would not be enough for simultaneous use of all 16 channels. With the SPI bus as communication interface, an increase of the overall sampling rate by scaling the number of ADCs on the mainboard design can easily be done. As this work focused on the NIRS module design, and the funds available for the instrument's design were limited and a few simultaneously active channels for BCI-trials are usually enough, this limitation was accepted for the time being.

Further design aspects regarding the ADC will be discussed in sections 3.5.5 (layout and shielding practice) and 3.7.2 (software implementation).

3.5.3 Communication/Bluetooth Transmission

For control and data transmission between the NIRS instrument and any host computer, the UART interface of the on-board microcontroller is used. This UART interface can be accessed by two means: By an ordinary RS232 wired connection or, as one aim of this work was to design the system for maximum mobility, via Bluetooth.
For the Bluetooth transmission, an embedded class 2 Bluetooth module by Amber Wireless was selected: The AMB2300 is a fully functional Bluetooth module with integrated LMX9830 antenna, configurable baud rate and several available integrated supported profiles. Using the Serial Port Profile in transparent mode, this module emulates a simple RS232 cable connection. Thus, with the software on the mainboard's microcontroller unit being implemented to support both modes of communication - wired and via Bluetooth - either one can be used.
In the latest prototype version of the mainboard, the interface is selected simply by using jumpers for the on-board Bluetooth module or a cable to a RS232 level converter unit with RS232 connector (see fig. 3.18).

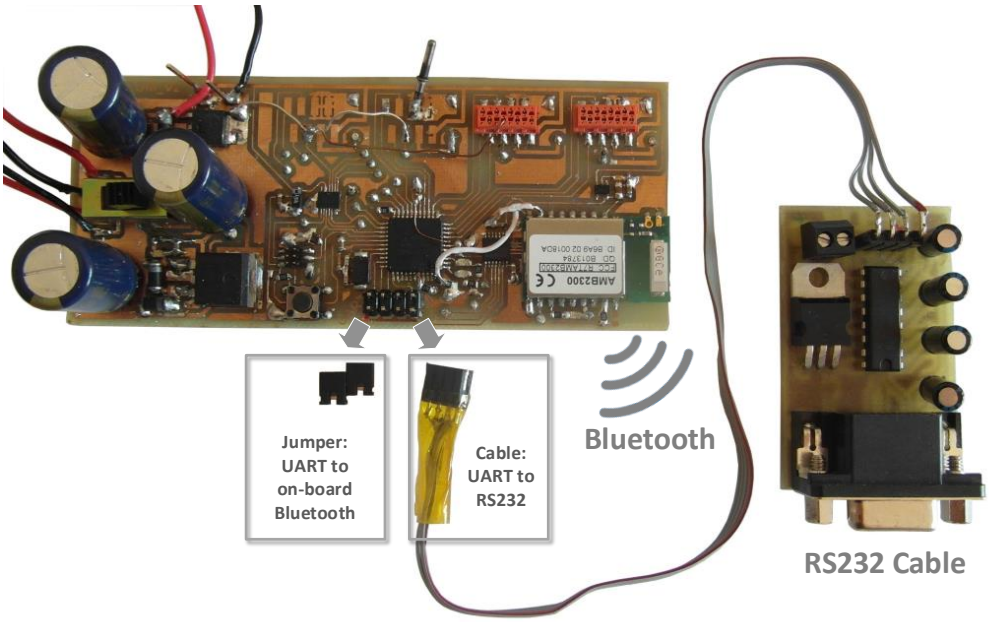

Figure 3.18: Communication interface: interface selection.

Implementing the support of a physical connection between the instrument and a PC without the use of the wireless module made the system suitable for a much better step-by-step hardware and software design testing and debugging.
Evaluation of the mainboard hardware and signal quality revealed that the Bluetooth module's high-frequency signals can generate significant electrical crosstalk to the on-board analog signal lines for analog-to-digital conversion. This crosstalk superimposes the amplified NIRS signal strongly enough for the signal to appear purely noisy after AD conversion. Fig. 3.19 shows the effect of the Bluetooth module signals on the analog dc NIRS signal (blue). $400mV$ peak-to-peak "Byte" noise distorts the signal significantly.

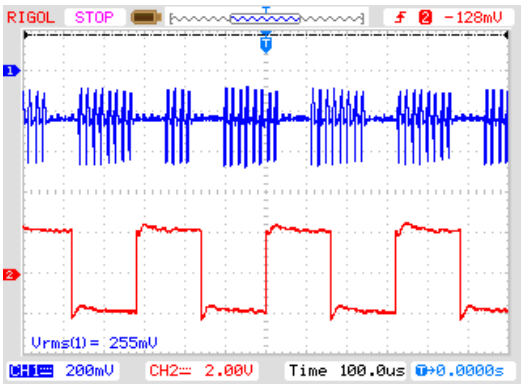

Figure 3.19: Bluetooth crosstalk on NIRS signal. Red: lock-in demodulator output, blue: low-pass output with Bluetooth interference.

To resolve this problem in the final version of the NIRS instrument (see fig. 3.20), the Bluetooth module and its peripheral hardware is placed on a separate PCB and is physically and electromagnetically separated by a metal shield surrounding the mainboard hardware. With the same interface selection concept as in fig. 3.18, the connector on the mainboard can either be used for the external Bluetooth PCB or for the RS232 level converter PCB.

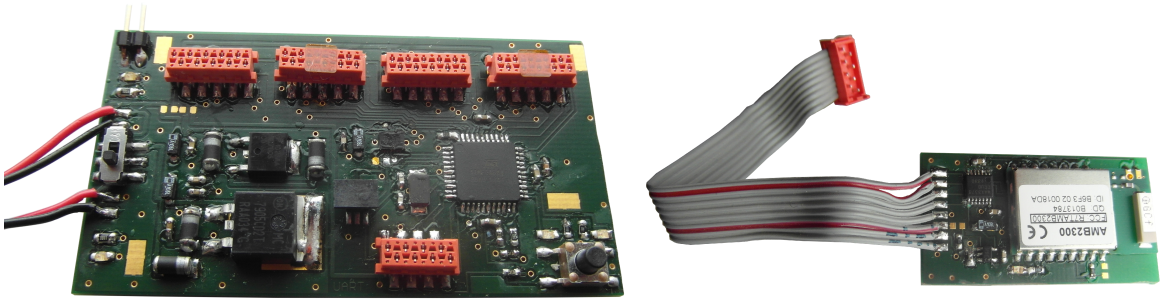

Figure 3.20: Final mainboard concept with separated Bluetooth module (right).

Figure 3.21 shows the hardware implementation of the final Bluetooth module PCB.

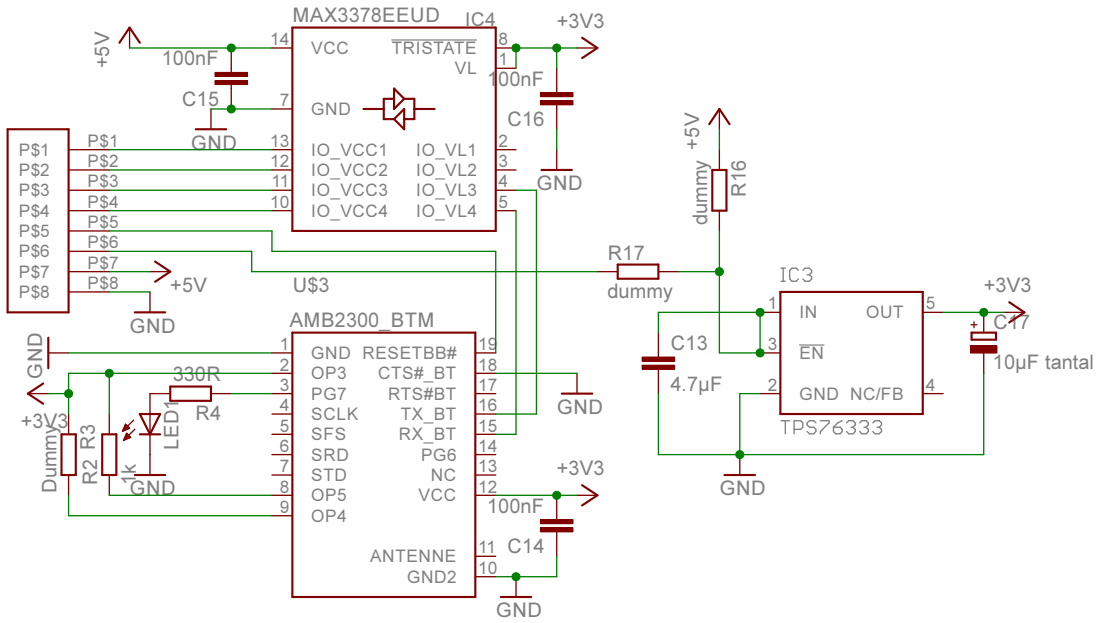

Figure 3.21: Hardware implementation of the Bluetooth module.

As the AMB2300 needs a $3.3V$ voltage supply, a TPS76333 low-dropout regulator (LDO) creates the $3.3V$ supply from the mainboard's $+5V$ rail. To minimize effects on the $+5V$ rail by the Bluetooth module supply currents, a $4.7\,\mu F$ input and a $10\,\mu F$ tantalum output bypass capacitor are placed closely by the in- and output pins of the LDO. The

input source ($+5\,V$ regulated or $+9\,V$ unregulated from the battery) can be selected by connecting one of two possible dummy $0\,R$ resistors.
As a result from the operation on different supply voltages, the digital voltage levels for the communication between microcontroller and AMB2300 have to be level shifted. A bidirectional level translation integrated circuit by maxim integrated (MAX3378) was selected for this purpose.
The AMB2300 Bluetooth module is externally hardwired for a baud rate of $9.6\,kbps$ and a LED is connected for status display.

3.5.4 Microcontroller Unit

For the control of the NIRS module channels and the analog-to-digital converter and for communication with a pc, an Atmel Corporation AtMega644 $8\,Bit$ microcontroller with $64\,kBytes$ in-system programmable flash and advanced RISC architecture was used.
The AtMega644 provides a programmable serial USART and a master/slave SPI serial interface, one $16\,Bit$ and two $8\,Bit$ timers/counters and 32 programmable I/O lines.

To guarantee the necessary accuracy for USART baud rate generation and to use the maximum possible processing speed, an external 20MHz crystal is applied. The design considerations are identical to the ones for the AtMega16A crystal in subsection 3.4.5.
For the generation of the USART baud rate and the selection of a proper crystal, some rules have to be followed to ensure error-free data transmission. The $8\,Bit$ baud rate register UBRR in the AtMega644 has to be configured using equation 3.18 (see AtMega644 datasheet)

$$UBRR = \frac{oscillatorfrequency(Hz)}{16 \cdot baudrate(bps)} - 0.5 \tag{3.18}$$

Since the value for UBRR has to be rounded, deviations of the generated frequency from the correct baud rate occur. For an error free data-transmission, the error

$$Error_{baud}[\%] = |(\frac{(UBRR_{rounded} + 1}{UBRR_{exact} + 1} - 1) \cdot 100| \tag{3.19}$$

has to be less than 1%.
For the chosen baud rate of 9600 and a 20MHz crystal $UBRR_{exact}$ is 129.208 and $UBRR_{rounded}$ is 129, resulting in an $Error_{baud} = 0.16\%$. Therefore, the crystal can be used.

For an automated start of the pre-configured instrument in an experiment, an external hardware trigger is implemented. It can be used, for example, to synchronize the start of a measurement with a certain condition becoming true, such as a button being pressed, a light sensor on a screen being illuminated, and so on. A jumper connector for those digital/analog control signals is provided on the mainboard. The input signal is analog-to-digital converted by one of the integrated $10\,Bit$ ADCs for comparison with a programmable threshold. When the control crosses the threshold line, a corresponding log-message is inserted into the UART data stream.

For status signals and debugging puproses, two LEDs are provided.

3.5.5 General Remarks on Layout and Design

As during the design of the NIRS module, the rules for good design practice were followed as well as possible and all supply pins of integrated circuits are buffered with $100nF$ capacitors.
For the final NIRS mainboard, a 4-layer PCB was designed (see fig. 3.22):

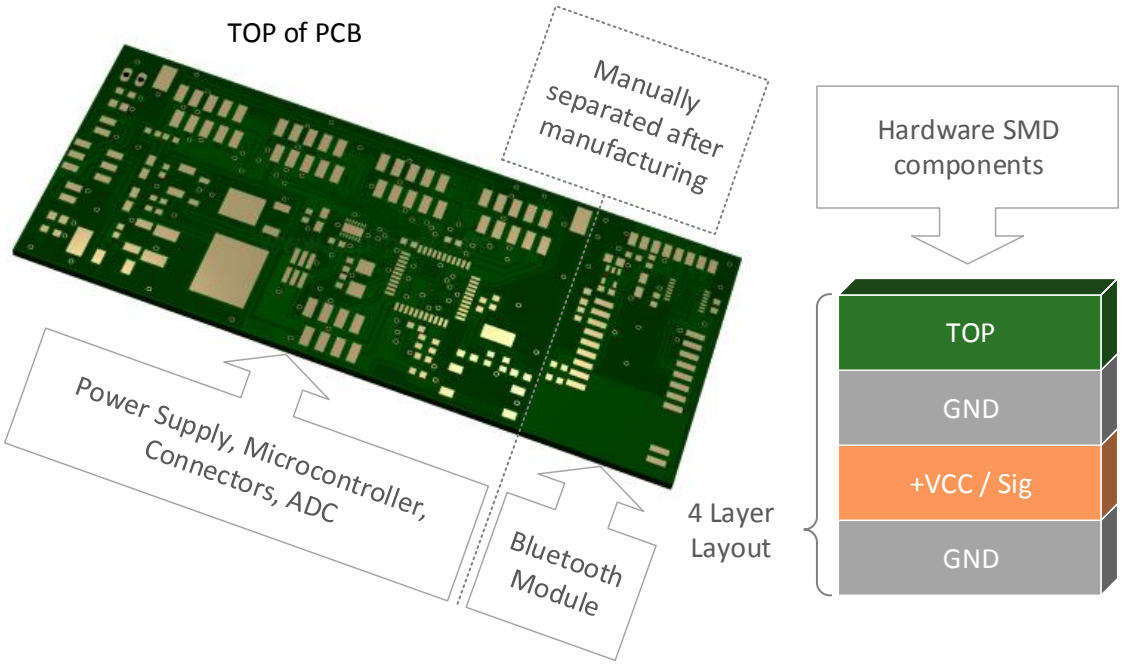

Figure 3.22: Layout of NIRS mainboard (using a PCB preview from www.pcb-pool.com).

The second and the fourth layer are designed as GND planes. Sensitive signal lines, such as the ones carrying the analog fNIRS signals from the connectors to the ADC, are routed between both GND planes and are thus shielded from external electric crosstalk coming from the Bluetooth module and other noise sources.
Below and around the ADC, only ground potentials, digital ADC control lines and analog signals are routed to further minimize noise pickup.

For cooling by passive heat distribution, the areas around and connected with the heat sinks of the voltage regulators are as large as possible.

On the Bluetooth module PCB, keep-out areas below and around the Bluetooth antenna were designed as specified by the manufacturer to minimize range attenuation by metallic elements.
To save manufacturing costs, the Bluetooth module and mainboard are designed in a single layout and manually separated after production.
The complete layout is depicted in fig. A.9 in the appendix.

3.6 Safety Aspects

Regarding user safety, there are three aspects that were considered in the system design process:

- *Hazards from supply voltages* in case of short circuits/direct contact
- *Hazards from high NIR light intensities* in case of eye exposure
- *Hazards from tissue heating* during direct contact with the NIR light emitters.

Hazard from supply voltages: As the system is designed for mobility and safety, only low-voltage components were used. At no time, the battery and supply voltages exceed 9V dc, which is in the range of protective extra-low voltage (PELV) and does not pose any danger even in direct contact to the skin over longer time periods.
As the measured data is transmitted via Bluetooth to a computer, no galvanic isolation between instrument and PC is necessary, as it is the case when using a RS232 cable. In the case that the UART-RS232 interface is used with a level converter and cable to the PC (as mentioned in subsection 3.5.3), it is only safe to wear the device in accordance with European medical isolation standards (EN60601-1) when the level converter/connector PCB includes a galvanic isolation between the NIRS instrument and the PC, e.g. by optocouplers. However, for testing and debugging without the need to wear the device, the direct cable connection could be used without galvanic isolation.

As NIRS is an active recording technique depositing energy into the subject and measuring the changes of the reflected energy, the effects of the deposited energy have to be taken into account.
Regarding the *hazards from high NIR light intensities* and *tissue heating*, safety assessments were made by Cope 1991 [21], Strangman 2002 [13] and Bozkurt 2004 [57]:
As there are no safety standards for single wavelengths in LEDs, as it is the case for Lasers (IEC68025), laser standards and the IEC62471 (photobiological safety of lamps and lamp systems) are often used as orientation. Because LED light is not coherent, relatively high intensities compared with laser light still do not pose danger to the eyes.
As NIR light is non-ionizing, it poses no risk of altering genetic information unlike UV radiation. The major concerns are discomfort and damage by tissue heating. According to Strangman [13], the maximum permissible exposure of NIR light on the skin ranges from $0.2\,W/cm^2$ at $630\,nm$ to $0.4\,W/cm^2$ at $850\,nm$ with the exact limits depending on many factors such as wavelength, coherence, duration and area of exposure.
The main potential hazard of NIR light is tissue heating as a result of absorption, as the vast majority of the energy ($> 95\,\%$) is deposited in the scalp [13]. Absorption by blood pigments in deep tissue is not a problem as they are constantly circulating and therefore cannot heat up. According to Bozkurt et al., the limits for tissue heating are set by the propability of cell death which is increasing when cell temperatures are sustained above $41\,^\circ$C. These limits are also applied in pulse oximetry applications. With the mean temperature of the forehead being $35\,^\circ$C, this permits a maximum increase of $6\,^\circ$C during longer usage of the instrument.
Systems using Time-Division Multiplexing (as is the case here) or sinusoidal modulation significantly lower the temperature increase of the scalp resulting from the cooling effect of duty cycles/idle durations [57].

3.7 Software Design

In the following subsections, the software design for both microcontroller units and for the user front end at the PC are explicated. Fig. 3.23 shows the software design concept for the instrument.

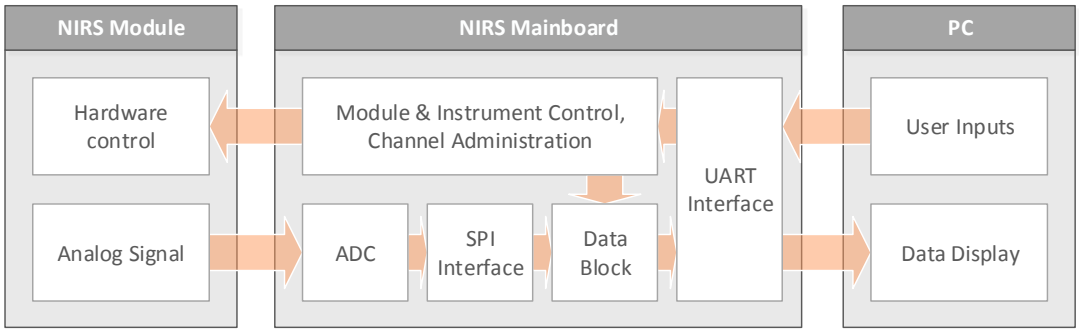

Figure 3.23: Software concept for the system.

The NIRS module software comprises mainly initialization and configuration of the hardware components and handling the control signals coming from the mainboard.
The NIRS mainboard software is based on a far more comprehensive design and includes the implementation of the communication protocols, handling of control signals from the user and (cyclic) generation of corresponding control signals for the NIRS mainboard. It also processes the converted NIRS data and creates identifiable data packages for the further processing on the PC.
The NIRS instrument can either be used and controlled with a simple operating system terminal program (or any other software that can send and process data via serial interface such as MathWorks Matlab), or with a graphical user interface that enables control, processing, logging and display of the received data.

The software for both microcontrollers is written in C and compiled and flashed with Atmel Coorporation AVRStudio v6.1. The software for the graphical user interface is based on National Instruments LabView and can be used as a stand-alone executable with a NI runtime environment.

3.7.1 NIRS Module

The NIRS module is controlled by the mainboard or any other custom data acquisition hardware using a simple $4\,Bit$ parallel interface as shown in tab. 3.3.

The bits CH1:CH0 represent the binary number of one of the four corresponding physical NIRS channel that is to be activated.
A rising edge on the TRIG line activates the channel that is selected with the CH1:CH0 bits, always beginning with $750\,nm$. Each subsequent rising edge toggles the activation

of both wavelengths of the selected channel, 750 nm and 850 nm.
When the RST line is pulled up, the multiplexer is deactivated and all channels are turned off. The next rising edge of the TRIG line starts the process all over again, beginning with 750 nm.

Bit #	3	2	1	0
Name	RST	TRIG	CH1	CH0
μC Pin	PD4	PD3	PD2	PD1

Table 3.3: Control Bits for NIRS module.

Fig. 3.24 shows a flowchart of the main routine on the NIRS module microcontroller.
After hardware reset/powering up, the external control interrupt for the TRIG line is initialized by configuring the External Interrupt Control Register for rising edge detection. Next, the PWM module of Timer/Counter2 is configured and enabled for lock-in modulation/demodulation. The PWM module is configured for toggle on compare match in phase correct mode for a 50% duty cycle PWM signal with a frequency of 3.125 kHz.
Then, the analog-to-digital converter ADC7 at the signal monitor line for PGA gain and current adjustment (out-of-range indication) is initialized and enabled for conversion in free-running mode.
After that, Timer/Counter 1 is configured for output compare interrupt request: As soon as a time threshold of 10 seconds is exceeded with no alteration of the multiplexer setup during that time, the currently active channel is disabled until reactivated by the mainboard. This makes the NIRS module suitable even for use without a TRG line. 10 seconds after a stop of the instrument, the module deactivates itself automatically.

Now, a calibration process can be started. The calibration routine is implemented for the sake of completeness but is not used at this time, as a fixed configuration of the PGA and DAC is used that is based on experimental determination of the optimal levels. For a maximum SNR of the device, primarily light emission and secondarily post-amplification should be maximized. The experimentally determined configurations can be used as fixed maximum levels as long as experiments do not indicate otherwise, which has so far not been the case: If the device is used on people with very high skin pigmentation or dark and thick hair, running the calibration cycle might further optimize the PGA/DAC configuration.
Using fixed levels, the current regulator DAC level is set to maximum (level 4 of 4, 100mA) and the PGA to a gain of $G = 44$.
Using the calibration cycle, the current level is initialized to maximum and then the PGA gain is reduced step-by-step until the out-of-range indication is false. As long as this is not the case, the current level is reduced by one step and the PGA procedure is repeated.

Now, a multiplexer test routine is started, enabling each channel and each wavelength for one second. This allows the user to manually check whether all channels are fully functional or hardware faults prevent the use of a certain channel.
Then, interrupts are globally enabled and the device enters an idle state. Each trigger from the NIRS mainboard on the TRG line then starts an interrupt service routine (ISR)

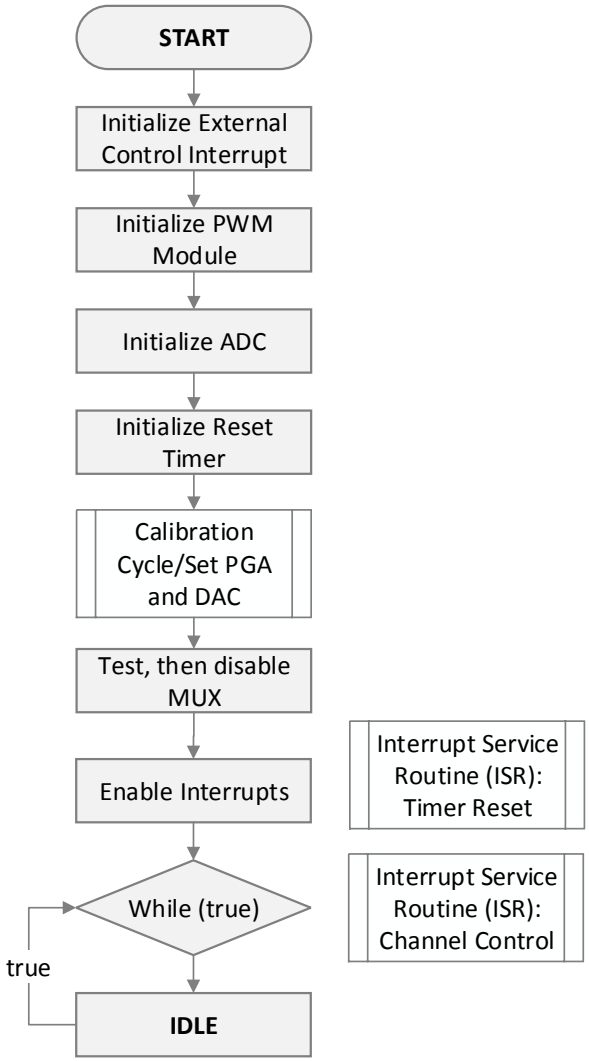

Figure 3.24: Flowchart of the NIRS module main routine.

for channel configuration and activation (see fig. 3.25).

When the ISR is called, the channel being currently active is turned off by a global MUX deactivation. Then, the new channel configuration is read from the CH1:0 bits at Port D pins PD2:1.
Depending on a global toggle bit (GTB) that indicates the last active wavelength, the multiplexer is then updated. The first rising edge (ISR) following a new physical channel selection results in a MUX configuration for the 750 nm wavelength current regulator of the corresponding channel and the toggle bit GTB is set. The second rising edge (ISR) results in a MUX configuration for the 850 nm wavelength of the same channel.
Thus, for the acquisition of one fNIRS datapoint at a single location, the corresponding NIRS channel number has to be configured (CH1:0) and two subsequent rising edges at the TRG line enable the access to the analog signals for the two respective wavelengths.

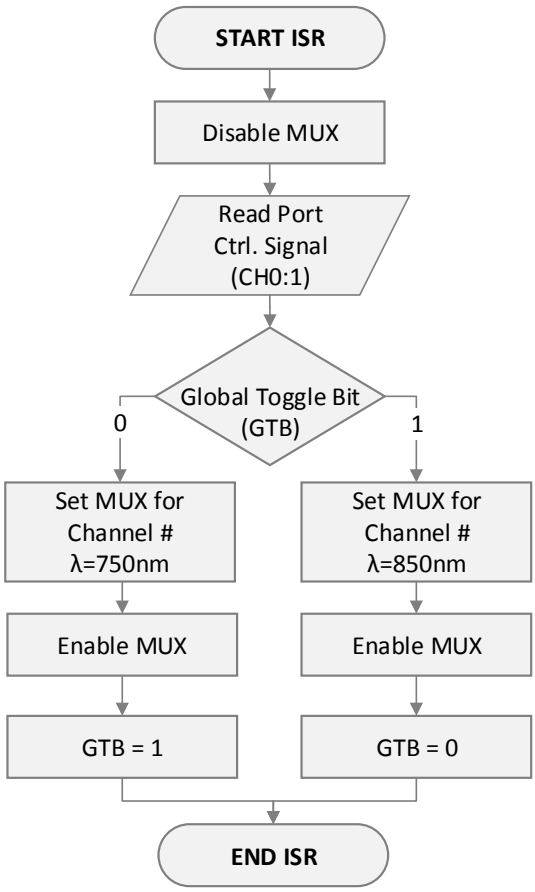

Figure 3.25: Flowchart of the NIRS module ISR.

3.7.2 NIRS Mainboard

The main routine of the NIRS mainboard uses several separately developed functional blocks, of which the most important are:

- LTC2486 ADC configuration and SPI communication module
- NIRS channel administrator
- UART-ring-buffer-based communication interface
- UART-received-data processing module
- UART data transmission package handler

The LTC2486 ADC transmits the conversion result of 16 bits plus sign bit in a 24 bits word, receives a 16-bits-long input configuration word and a start of conversion command through the SPI interface. The principal operation is depicted in a state transition diagram in fig. 3.26
As the SPI interface is a synchronous interface, the ADC has to be configured for the next conversion when the last conversion result is read. Using information from the NIRS channel administrator, the implemented LTC2486 ADC configuration module generates the configuration word according to the next channel that is to be activated and to settings configured by the user. These user settings are either speed mode activation/deactivation (2x sampling rate, no internal calibration) or temperature sensor requests.

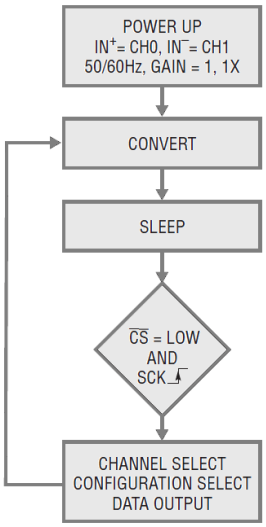

Figure 3.26: LTC2486 State transition diagram, taken from LTC2486 datasheet.

When called, the SPI communication module sends a 24 bits configuration word (16 bits configuration + 8 dummy bits), saving the received 24 bits last conversion result from the ADC.

The channel administrator is a FIFO-buffer-based function implemented for the automated generation of NIRS module control signals dependent on a user-defined selection of all available NIRS channels. If, for example, only two of four channels of a NIRS module should be used (allowing a higher sampling rate), the user can select those channels during configuration. The channel administrator then only considers the selected channels for channel activation control signals.

For the UART interface communication, a fully functional ring-buffer- and interrupt-based UART module was implemented and tested. However, to avoid race conditions in the complex main routine of the mainboard, a more sophisticated UART AVR ring buffer library by P. Fleury [79] was used for the final mainboard software.

Instrument control data that is received from the user PC via Bluetooth is read from the UART receive buffer and processed in a data processing module. This module is implemented as a simple conditional switch-case loop that processes the control bytes. The control bytes are single ASCII characters and will be described in detail in the next subsection (Console User Interface).

The data received from the ADC is managed by a data transmission package handler that adds channel/configuration information for identification and a timer value as timestamp to the ADC value and puts the data package into the UART transmit buffer. The data packages are 23 bytes long, ASCII-formatted, provide semicolon-separated values (CSV) and are built up as follows:

M	#	;	C	#	;	L	#	;	S	#	;	ADCVAL	;	TIMERVAL	CR	LF

The 12 $Byte$ header assigns the configuration information to the submitted ADC and timer values: Number # (0-3) of the active NIRS module M, number # (0-3) of the active channel C on this module, number # (0-1) of the active wavelength L with 0: 750 nm, 1: 850 nm and speed mode S active (#:1) or inactive (#:0). Subsequently, the 16 Bit ADC value (ADCVAL) in hexadecimal format and the 16 Bit timer value (TIMERVAL) in hexadecimal format are submitted, followed by a carriage return (CR) and line feed (LF) flag.

In the following, the aforenamed functional modules are put into the context of the main routine on the NIRS mainboard (see fig. 3.27).

Figure 3.27: Flowchart of the NIRS mainboard main routine.

After power-up or hardware reset, the AtMega644 UART interface is initialized and configured for a baud rate of 9600 bps, 8 data bits, 1 stop bit and no parity bits.
Subsequently, the SPI interface is initialized and enabled with the AtMega644 being configured as master, followed by the initialization of the 16 Bit timer and trigger line ADC. The 16 Bit timer is configured with a 1/1024 prescaler for output compare interrupt requests when the Output Compare Match Register A value 0d195 is matched. This configuration results in an incrementation of the NIRS signal timestamp every 10 ms. This time resolution was judged to be sufficient for later NIRS signal evaluation and applications.
The trigger line ADC is configured for free running, left adjust result conversion, allowing to quickly readout the 8 most significant bits for threshold comparison. As mentioned in subsection 3.5.4, this enables the logging of external events that are expressed as analog signals at the optional mainboard input, e.g. of trial/experiment start/stop signals.
After the initialization of all elements is finished, interrupts are globally enabled, the AMB3200 Bluetooth module is being reset and the main loop is entered. Incoming data packages from the Bluetooth module can now be processed.

The main loop begins with the access of the UART receive buffer, requesting one data byte.
If there is data in the buffer and no frame or overrun errors were detected, the data is processed and the instrument is configured (e.g. started, stopped, etc.) according to the control byte. In case of an error, error messages are sent to the user via the UART interface. If the receive buffer is empty, which is the case in most of the cycles, a running mode flag is checked:
If the device is not in running mode, e.g. stopped or not having been started yet, a get temperature flag is checked. This flag is set when the user requests a temperature measurement by sending the according control byte. If this flag is true, the ADC is configured for temperature readout and the received data is extracted and sent to the user.
If the device is not running and no temperature request has been made, the device sets a channel administrator start flag that resets the channel administrator to the starting point and an empty buffer flag that works as an indicator for the acquisition process. If the empty buffer flag is set, the acquisition process discards the first ADC value in a new measurement, as it is the result of an obsolete conversion (see fig. 3.26)

If the device is in running mode, however, the NIRS channel administration and acquisition process is executed. Fig. 3.28 depicts the details of this process.

First, the integrated threshold ADC for event logging is accessed and the received value is processed by a threshold ADC handler. In case the signal crosses the threshold towards the top, a signal-over-threshold message is sent ("#SSOT") to the UART transmit buffer, in case the signal falls below the threshold, a signal-under-threshold message is sent ("#SSUT").

Next, the channel administrator is called. It works on two typedef structures which carry the complete actual and last active configuration data and information of the instrument. Whenever called, it calculates the next active channel configuration for the LTC2486 ADC configuration module and saves the last active configuration for the assignment to the conversion result that is going to be received in the next cycle.

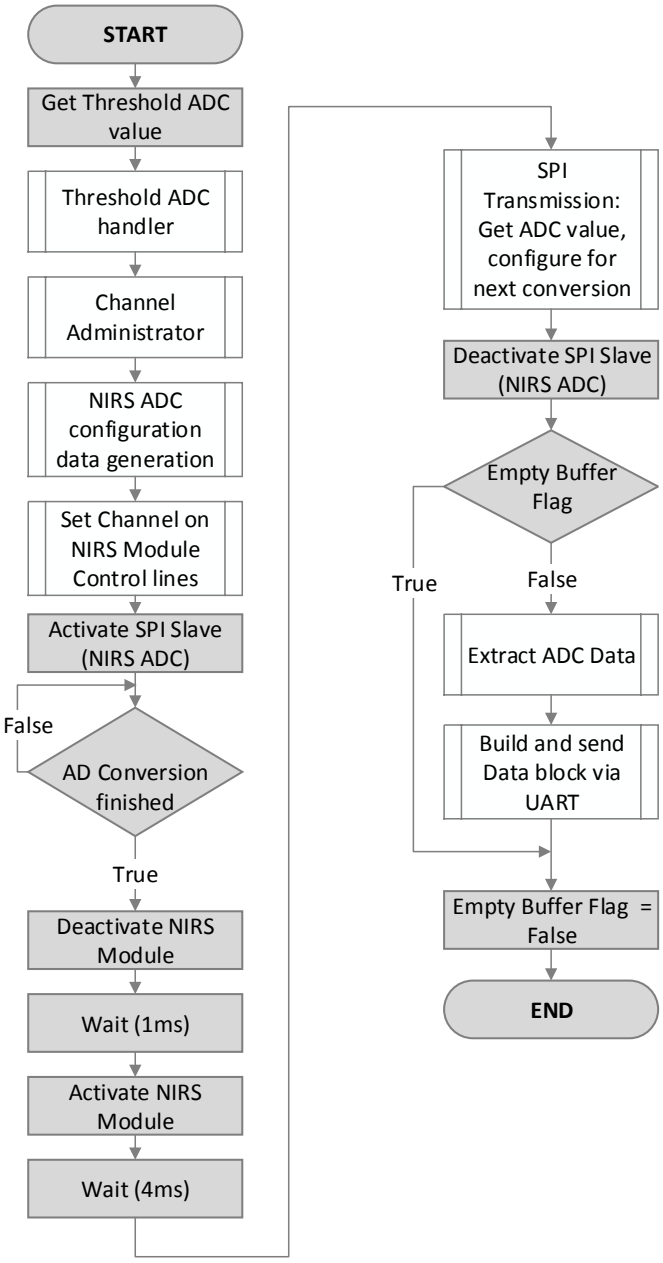

Figure 3.28: Flowchart of the NIRS mainboard module administration and acquisition routine.

Using the newly generated configuration data, the LTC2486 ADC configuration process produces the 16 Bit configuration word for the ADC and the bits for the next channel (CH1:0) are set on the parallel 4 Bit interface to the active NIRS module.
Now, the NIRS ADC is activated, allowing the observation of the status of the running conversion on the SDO line of the SPI interface. When the conversion is finished, the currently active NIRS module is deactivated (TRG control line is pulled low). After a delay of 1 ms, the NIRS module is reactivated (TRG control line pulled high, rising edge) and thus the next configured channel is turned on on the NIRS module. A dwell time of 4 ms is then applied for stabilization of the current regulators and the photodetector.

With the new configuration being active, the SPI transmission is started: The conversion result for the last channel configuration is received and the new ADC configuration is sent. After the transmission is finished, the SPI slave is deactivated for low-power conversion.
The received data is now either discarded, when the above-mentioned empty buffer flag is set, or processed by a function for the extraction of the ADC value. The extracted ADC value together with the typedef structure for the last active configuration information are then processed by the data transmission package handler for 23 $Byte$ data block generation and the data block is put in the UART transmit buffer.

3.7.3 Console User Interface and Control Commands

The communication interface of the NIRS instrument is designed for both manual console inputs and automated software control. To achieve this, the control data interface uses the ASCII format, and data can thus be easily read and generated by the user on a keyboard. The instrument sends instructions and information to the user after configuration and is controlled by a set of single-byte ASCII characters that are processed by the NIRS mainboard's data processing module:

- **"G" - Go**: Starts the running mode of the device. The timer is reset and a new acquisition process is started.
- **"S" - Stop**: Stops the running acquisition. All NIRS modules are deactivated.
- **"E" - spEed mode**: Toggles the ADC speed mode (maximum sampling rate).
- **"P" - Pause**: Pauses the running acquisition process without stopping the timer.
- **"C" - Configuration**: Enters configuration mode. Once the configuration mode is entered, the identification numbers of the channels that are to be used in the next acquisition process have to be provided, followed by an "X" for leaving the configuration mode.
- **"R" - Read configuration**: Reads the configuration data. The active configuration matrix of the instrument, showing the activation/deactivation statuses of all channels, and the speed mode status is sent to the user.
- **"T" - Temperature request**: Sends a temperature measurement request. The instrument will then send back a temperature measurement in the next cycle.
- **"H" - Help**: The device sends the above-mentioned list of commands with short comments and syntax help.

Fig. 3.29 gives an example of the typical console usage of the device. The user control inputs are shown on the left, and the the data received from the instrument is shown on the right.

3.7.4 LabView User Interface

For the final stage of development and testing as well as for later evaluation and use, a stand-alone graphical user interface (GUI) was programmed using LabView 2012.
To enable asynchronous processing and quick code execution as well as to avoid GUI lockup, this program is build on an event-based queued state machine (eQSM) architecture. At first glance, the eQSM architecture is a complex approach but significantly facilitates programming mid-sized to advanced projects so that it is nowadays widely used as a standard LabView architecture.

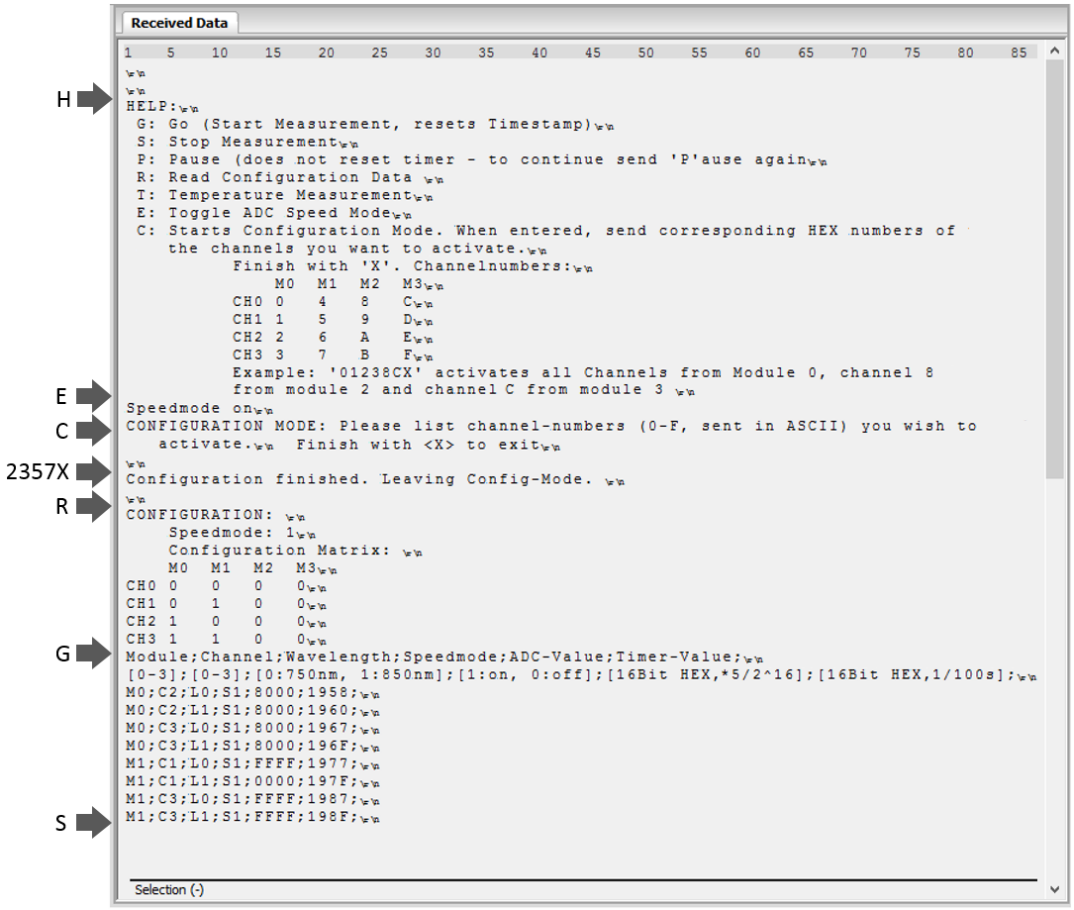

Figure 3.29: Typical console usage example.

In the following, the architecture of the designed LabView NIRS user interface will be briefly explained and the GUI functions will be described.

The eQSM architecture is based on a producer-consumer principle using a combination of three basic LabView structures: Events, queues and state machines.
Queues are structures that process and transfer data packages in a FIFO manner. An element of a virtual instrument (VI), e.g. a subVI, can insert data into a queue at any time and independently from its own position in the VI. Once called, another element can access this data from any position in the VI. This enables data transfer between loops without the generation of waiting conditions, allowing asynchronous processing. Hence, a queue acts as a global variable that can buffer data. Once a process accesses an element in the queue, it automatically removes the element from the queue, thus preventing multiple readouts of the same element (e.g. one acquisition data point).
The eQSM is a state machine that is controlled by messages from a message queue. User events as well as any other processes in the program can create these messages. The state machine itself puts information, such as acquired data, in a data queue. The data of this queue is then processed by a consumer loop for analysis, display, etc.

The NIRS LabView graphical user interface architecture using the eQSM architecture (see fig. 3.30) is therefore based on

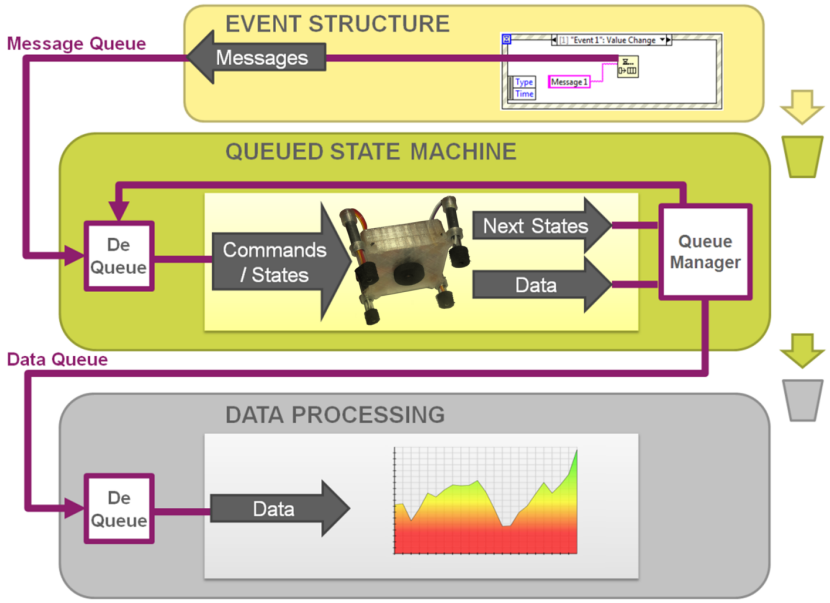

Figure 3.30: LabView eQSM architecture.

- *An event handler loop* that processes user input events and converts them into messages for the queued state machine, inserting them into the message queue. It also sends basic control signals to the NIRS instrument, such as ”G”o, ”S”top, etc.
- *A queued state machine* that reads the messages and acts as data producer. It processes the data from the NIRS instrument, handles errors, idle states, etc. and inserts the data from the instrument to the data queue.
- *A data processing loop* that is the data consumer, retrieving the data elements from the data queue. The processing loop logs, filters and displays the measured data and can execute further mathematical operations, such as the calculation of the modified Beer-Lambert Law (MBLL).

The communication between the graphical user interface (GUI) and the NIRS instrument is implemented using basic virtual instrument software architecture (VISA) VIs and functions provided by LabView. For an initial overview of the software implementation, see the block diagram in the appendix (fig. A.13). Due to the complexity of the implemented eQSM, please refer to the LabView files on the annexed data carrier for a detailed documentation of the software implementation.

Fig. 3.31 shows the finished GUI for the NIRS instrument. The software has been compiled and can be used as stand-alone executable together with a LabView and a VISA runtime environment that both are available for free on the National Instruments website. The instrument is controlled by buttons and a configuration matrix that represent the implemented ASCII control codes: Start, Stop, Get Temperature, Speed Mode and Configuration Transmission.
When the program is started, first a VISA connection has to be established, using the

corresponding emulated serial port from the operating system's Bluetooth adapter. The connect button then opens the communication channel between GUI and the NIRS instrument. To close the connection, a disconnect button was implemented.
After the communication channel has successfully been established, the current configuration data (active channels and speed mode status) is read from the device using the "R" command and the configuration is displayed in an interactive channel selection configuration matrix (green lamps). Clicking on one of the available channels (Ch0-3, Module 0-3) toggles the activation of this channel. Using the Configure button, a new configuration is transmitted to the instrument.

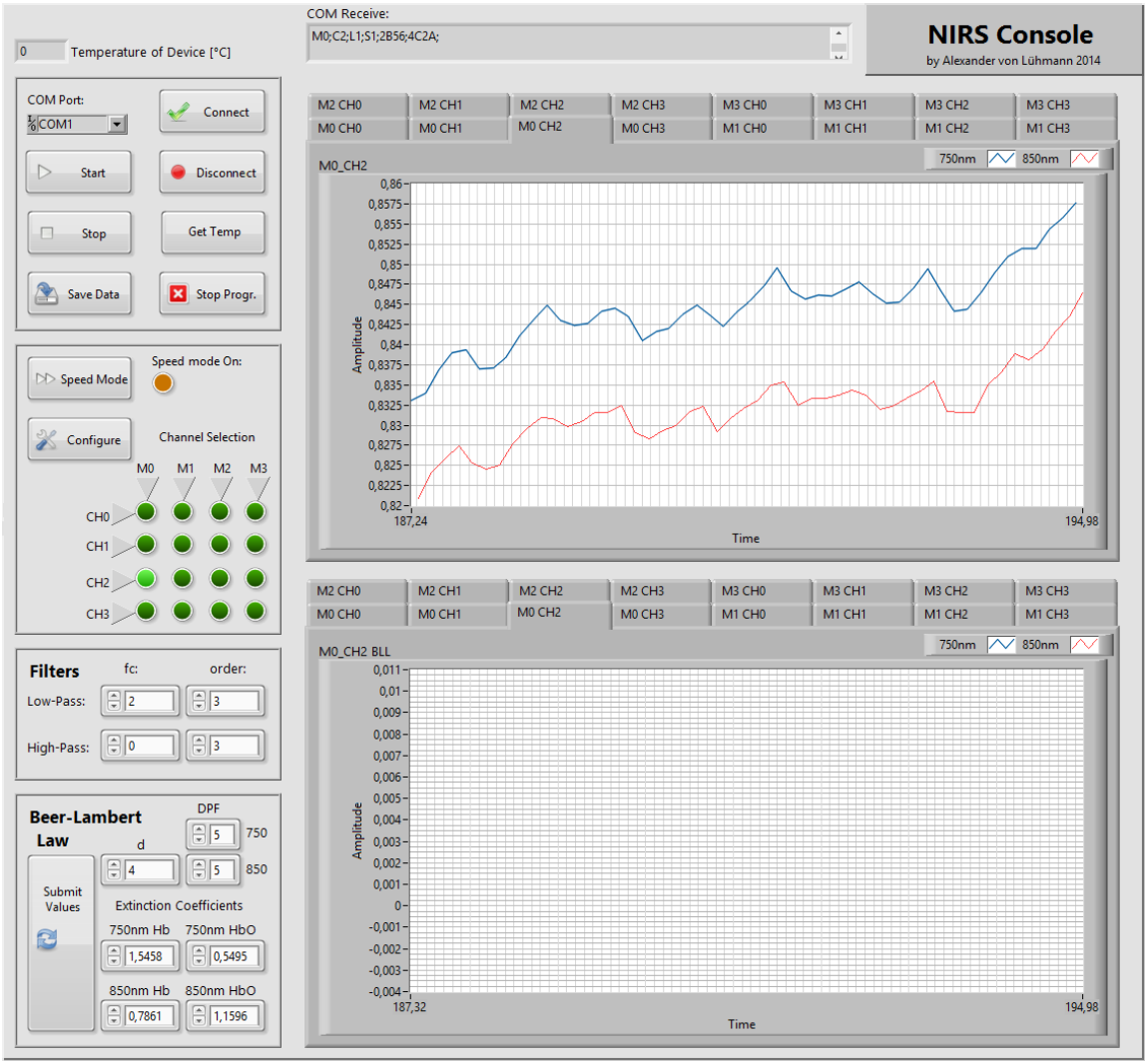

Figure 3.31: LabView NIRS software - graphical user interface.

At the very top of the GUI window, a "COM-Receive" window is implemented for display of the received and unprocessed console data from the device.
Right below, each channel can be selected for raw data display in a graph with selectable time window size (usually 100 samples). In the picture, channel 2 of module 0 is active and the two signals from both NIR wavelengths are shown. The peaks in the signals are

the result of cardiac cycle pulse waves.

Below that, the data from each active channel can be shown after application of the modified Beer-Lambert Law (MBLL). The parameters of the MBLL (DPFs, d, extinction coefficients) can be configured in the bottom left corner and have to be submitted once before the display can start. For the sake of completeness, all 16 NIRS channels are implemented graphically - but due to the extent of this work, the MBLL calculation is implemented only for four channels (CH0-3 of module 0) in the block diagram.
Also, a control for digital filters is implemented in the GUI that allows configuration of high- and low-pass filters for signal filtering. These filters have not been implemented so far as the GUI was used only for qualitative signal evaluation and raw data acquisition: Further data processing was done with matlab scripts.

To log the acquired data, a saving routine was implemented. When called, the routine creates a log file with a header carrying all relevant configuration and experimental information (current date and time, active channels, speed mode, ...) and a data block carrying the acquired data streams in a semicolon-separated CSV format.

3.8 Mechanical Design

Corresponding to the modular concept of the NIRS instrument, a modular mechanical design was developed. It is based on a spring-loaded housing for the NIRS module and a chained multiple-unit housing design for the mainboard, the Bluetooth module and batteries for fixation at the upper arm.
The construction of the mechanical elements and housings was done using Siemens NX 7.5 CAD software. For technical drawings of the instrument's housing parts, please refer to fig. A.11 and fig. A.12 in the appendix. The renderings for the figures for concept illustrations were done with Blender3D, using the meshes from the CAD design and meshes from the "BodyParts3D" life science database archive [80]. The designed elements were then produced from polylactic acid (PLA) plastic material, using a 3D printer.
In the following, both mechanical design concepts will be discussed in detail.

3.8.1 NIRS Module Attachment

The geometrical arrangement of the four NIR light emitters and the detector on a NIRS module is shown in figure 3.32. With the NIR light detector based at the center of the arrangement, the four LEDs are placed at opposite corners in equal distances of configurable $30 - 35\,mm$.

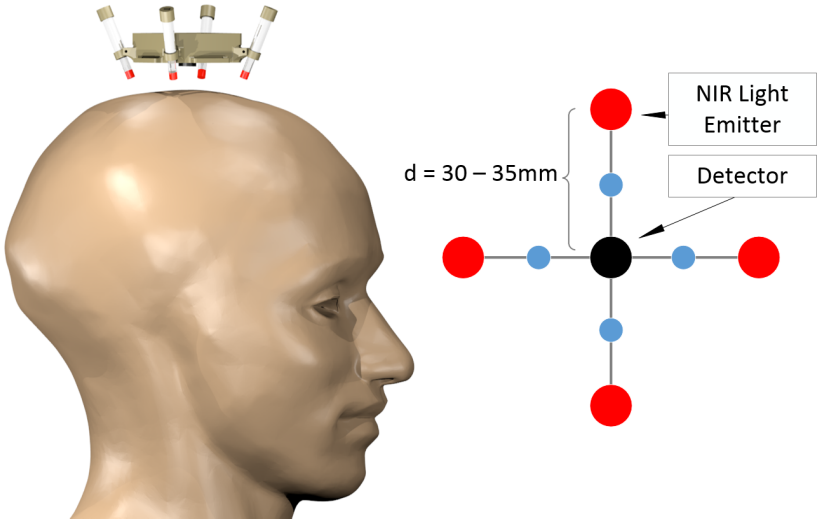

Figure 3.32: Geometrical arrangement of NIR light emitters and detector.

The blue dots in the figure represent the resulting points of the highest sensitivity for functional cortex activity.

For the optimal signal quality, it is important that the NIR light detector and the NIR light emitters are as close to the scalp as possible, while at the same time being perpendicular to the surface for maximum sensitivity and light penetration depth.
To adjust the emitters/detector perpendicular to the surface and at the same time provide an optimal fit of the NIRS module to the head, the NIRS module mechanical design was based on a spherical approximation of the head (see fig. 3.33).

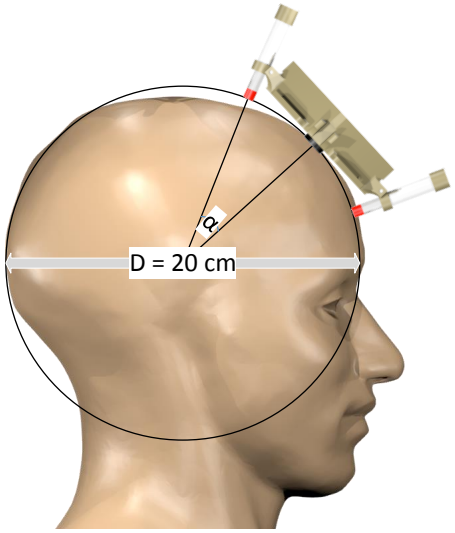

Figure 3.33: Design for head geometry alignment.

Using a sphere with a 20 cm diameter for the head, the necessary angle of slope α between detector and emitters could be specified as approximately 16 ° and the mechanical construction could be based on defined geometrical constraints.
With the module holder being a completely stiff construction, no alignment to the natural unevenness of the head and its deviations from the spherical approximation is possible. To enable an alignment and minimize influences on the signal due to movement of the head, the design is based on a spring-loaded concept (see fig. 3.34).

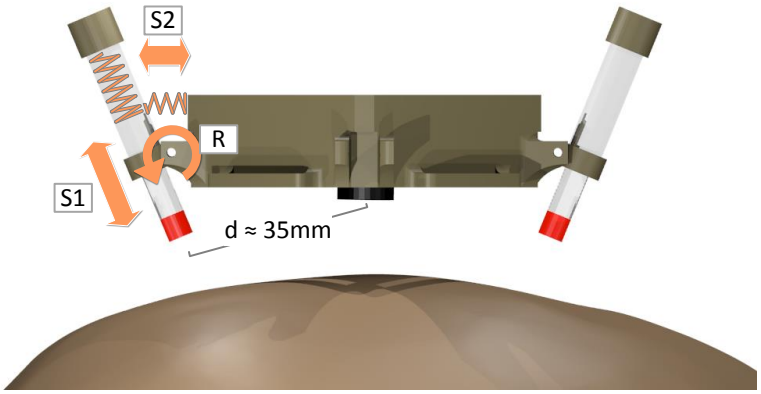

Figure 3.34: Mechanical spring-loaded design for the NIR light emitters.

The NIR light LEDs (depicted red in the image) are not stiffly connected to the module body housing but integrated in movable spring-loaded LED holders. These holders are based on two nested tubes that are spring-loaded against each other (S1) and against the module housing (S2) and are able to rotate around an axis (R).
Spring S1 presses the LED towards the surface of the head, thus enabling alignment and preventing the loss of contact during movements. Spring S2 and the rotary joint R keep the LED perpendicular to the surface while enabling small deviations for comfort and

alignment.

In the following, the components and assembly of the NIRS module body housing and spring loaded LED holders are briefly described. Fig. 3.35 shows the components and assembly.

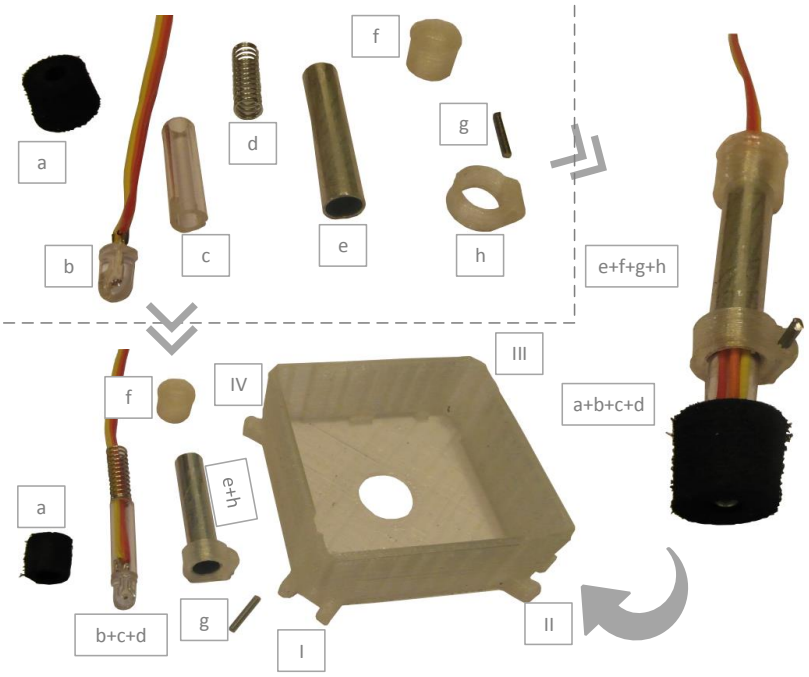

Figure 3.35: Components and assembly for spring-loaded design concept

The spring-loaded LED holders are built using 20 mm-long acrylic glass tubes (c) with an outer diameter of 6 mm, 30 mm-long aluminum tubes (e) with an outer diameter of 7 mm and a wall thickness of 0.5 mm and 18 mm-long metal springs (d) with a 5 mm outer diameter. The multi-wavelength NIR LED is soldered to a 3-wire ribbon cable (b) which is then lead through the treated glass tube and the metal spring (b+c+d), (S1).
A custom 3D-printed holder (h) is glued to the bottom of the aluminum tube (e+h) and a printed stopper plug with a through-hole (f) is glued to the top of the tube. Another custom 3D-printed stopper plate (not in the picture) is glued to the acrylic tube directly behind the LED. The LED is then encased by a thick opaque tube made of cellular rubber (a) for stray light prevention and cushioning, and its acrylic tube, spring and ribbon wire (a+b+c+d) are slid through the aluminum tube with holder and stopper plug (e+f+g+h). Now, four of these constructions are fixed to the module body housing at its four corners (I, II, III, IV) with 1 mm diameter steel pivot pins (g) that are slid through the hubs of the aluminum tube holder (h) and the module body housing corners, creating rotary joints (R).

The springs S2 are then inserted between the module housing corners and the LED holders. Figure 3.36 shows the finished NIRS modules.
To minimize stray light influences and for cushioning purposes, the detector is encased by an opaque cell rubber tubing. Also, the NIRS module body housing is painted with

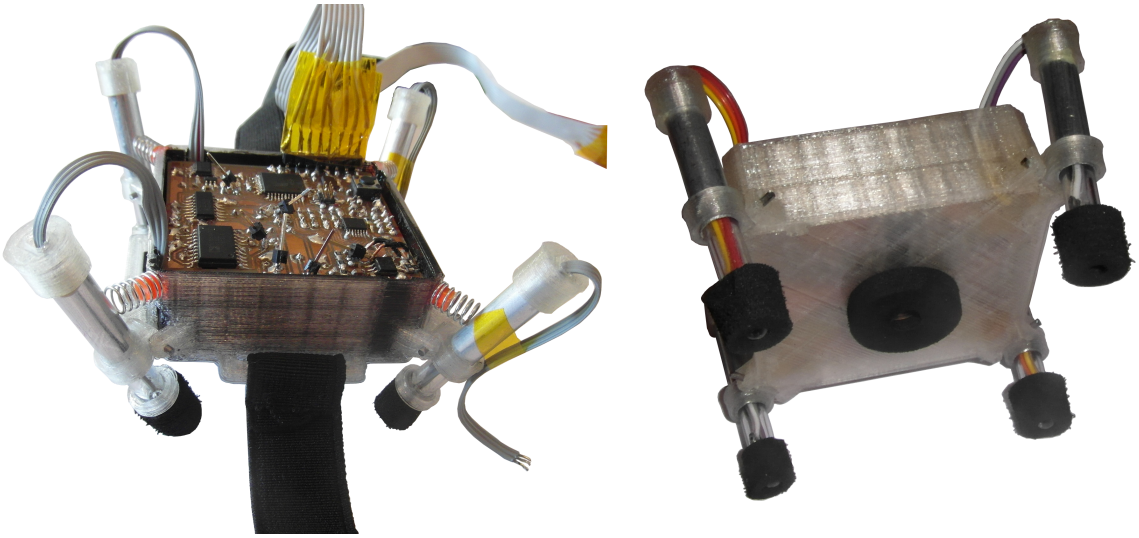

Figure 3.36: Complete mechanical spring-loaded NIRS module.

opaque black paint from the inside to minimize NIR light effects on the sensor from directions other than perpendicular to the sensing surface. For fixation to the head, a flexible ribbon with hook-and-loop fastener for length adaption is sewed to the module housing.

3.8.2 Mainboard and Batteries

Two fundamentally different approaches for the casing and wearability of the mainboard module and batteries were developed.
The first approach uses the mainboard prototype and will be only briefly discussed, as several improvements were made for the second approach using the final version of the mainboard. In the first approach, mainboard, on-board Bluetooth module and two 9V batteries are encased by a neck-worn case cushioned with cell rubber (see fig. 3.37).

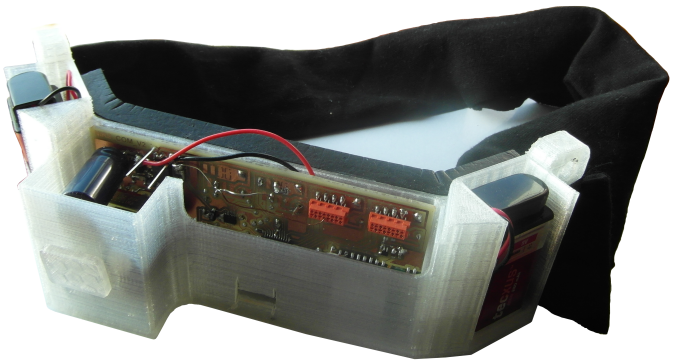

Figure 3.37: Neck-worn mainboard module.

As even low pressure on the throat during fixation of the module is instantly perceived as unpleasant, the case is worn like a necklace: With the cushioned mainboard housing

at the back of the neck, the module is counterbalanced by a weight fixed to a soft fabric sewn to the body housing hanging down the chest.

For the final design, a different approach was developed. Resulting from the necessity to physically separate the Bluetooth module from the rest of the mainboard (see subsection 3.5.3), to enable the use of bigger battery packs for prolonged instrument operation, and to maximize user mobility, a multi-module concept for the attachment to the upper arm was designed (see fig. 3.38).

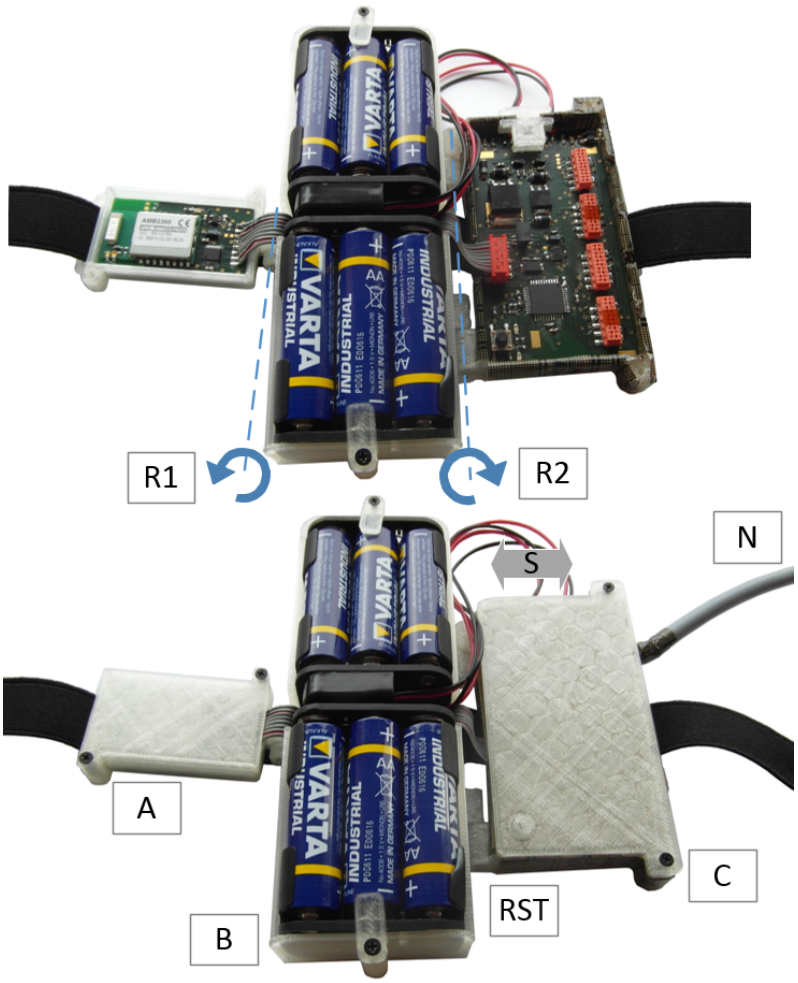

Figure 3.38: Mechanical concept for mainboard arm attachment.

The design is based on three main module cases that are interconnected via rotary joints (R1, R2): The Bluetooth module (A), the battery holder (B) and the NIRS mainboard (C).
The battery holder holds two 6 AA battery packages (9V) and allows easy battery replacement. The Bluetooth module case is placed as far as possible from the mainboard case and the module is connected via a ribbon cable connector.
The inside of the mainboard module case is lined with conductive shielding grid tape (Desco, type 81250). Custom on-off switch and reset push button adapters were designed

for access to the on-off switch (S) and microcontroller reset button (RST) when the case is closed.
To close the Bluetooth and mainboard module cases, the corresponding lids are screwed in place. Screwing the mainboard case and lid together also fixates the shielded NIRS cable (N).

For the attachment to the arm, a flexible ribbon is guided through fixation elements of the module cases. The unit can then easily be tied to the arm of a subject (see fig. 3.39): The rotary joint connections allow mechanical adaption to the shape of the arm and the flexible ribbon prevents slipping.

Figure 3.39: Mainboard and batteries: arm attachment.

4

Evaluation and Analysis

The NIRS instrument design process involved many evaluation and debugging steps that were often conducted iteratively. Results of these evaluation steps were integrated in successive versions of the instrument. Throughout the development phase, one evaluation board, 3 mainboard prototypes, 3 NIRS module prototypes and one respective final version were developed, each succeeding version gradually improving the instrument's design. The results of this process and the most important insights during design and evaluation of the functional elements are elaborated in the corresponding design sections in the previous chapter 3.
To characterize the whole system, however, particular characteristics were further evaluated and analyzed and will be discussed in the following section. After that, the results of physiological measurements and BCI trials for system verification and validation will be presented.

4.1 Evaluation of Hardware and Design

4.1.1 PWM Signal

The deviation of the 3.125 kHz PWM signal from an ideal square-wave reference for lock-in (de-)modulation was investigated. Fig. 4.1 shows the signal characteristics: The microcontroller's PWM module produces a stable square-wave signal with 27.2 ns rise and 19.6 ns fall times. Fourier power spectrum analysis reveals clean 3.125 kHz peaks and higher harmonics.

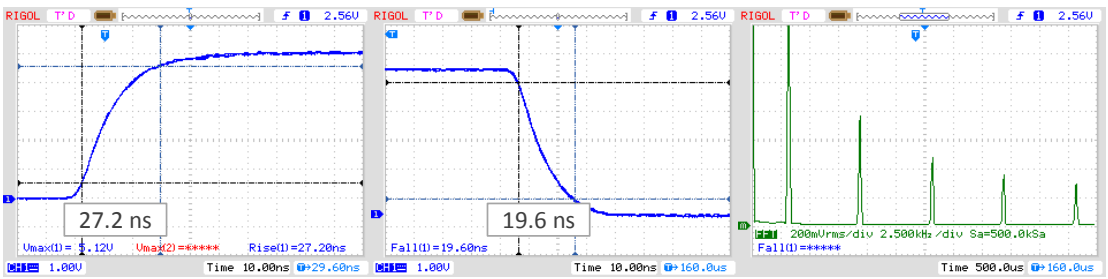

Figure 4.1: PWM signal characteristics at the microcontroller output.

As mentioned in subsection 3.4.3, the PWM signal is level shifted by a voltage divider for zero crossing detection in the lock-in demodulator. The RC network that results from the high-ohmic voltage divider resistors and PCB line capacities affects the PWM signal propagation: It creates an effective propagation delay of the signal's zero crossing of approximately $4\,\mu s$.
Even though this delay was not intended, it has a positive effect on the demodulation during lock-in detection: It compensates for $4\,\mu s$ of the phase shift between the microcontroller PWM reference for current modulation and the incoming pre-amplified photodetector signal that is to be demodulated. Thus, the attenuation resulting from demodulation (see subsection 4.1.4) is reduced.

4.1.2 Power Supply

For the power supply, two different characteristics were evaluated: DC supply voltage drifts during signal acquisition, and current modulation impacts on the supply voltage.

The DC supply voltage drift measurements yielded a stable supply voltage of $+4.959\,V$ and $-4.960\,V$ with $< 500\,\mu V$ drift in 20-minutes measurement periods. However, when the device was started after being inactive for several hours, a supply voltage stabilization period of several seconds was observed. Possibly due to battery voltage recovery during off-times, a voltage regulator output drop of up to $20\,mV$ in a period of $< 20\,s$ takes place until the output voltage reaches a stable level. Thus, prior to signal acquisition, a waiting cycle of $20\,s$ after initial instrument power-up is recommended.

To investigate the impacts of the $3.125\,kHz$ current modulation on the power supply and thereby on the photodetector and signal amplification components, their output signals were evaluated during active modulation but without optical input to the sensor. For this purpose, the active NIR LED was placed in an opaque metal box and the photodetector was covered with opaque sticky tape.
To evaluate the maximum impact of the current modulation on the signal, the LED was modulated using the maximum DAC current level ($100\,mA$, DAC level 4). To specify whether the current modulation effects can be minimized by using different voltage supplies, the measurements were done with two different sources for the LED current (for reference, see VCC in fig. 3.12): First, the mainboard's $+5\,V$ regulated voltage rail common for all hardware elements was used, then the LED current was supplied directly from the $+9\,V$ battery voltage. Figure 4.2 shows the resulting ouptut signals of the OPT101 photodetector and the PGA during current modulation without optical input to the sensor.
The current modulation flanks create a $\pm 2\,mV$ high-frequency noise around the sensor output baseline signal that is further amplified by the PGA to strong $\pm 100\,mV$ peaks. Supplying the current directly from the battery to minimize impacts on the regulated $+5\,V$ does not improve this.
However, an influence on the baseline of the signal could not be observed and high-frequency noise is effectively suppressed by the 3rd-order lock-in low-pass. Therefore, these effects are presently considered not crucial. Yet, in future power supply design approaches, high-frequency decoupling of the supply voltage is recommended.

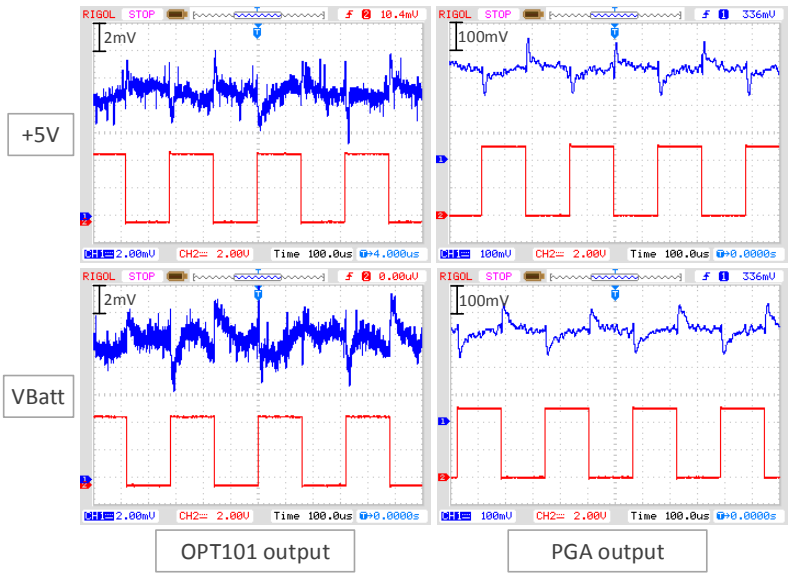

Figure 4.2: Current modulation impacts on signal detection and amplification path. Blue: output signals, red: PWM modulation reference.

4.1.3 Current Regulators

To optimize the current regulator performance, the selection of the operational amplifier was based on an evaluation of speed and oscillation characteristics of two high-precision types (LMC6064 and AD824A) that were considered for the design. As indicated by the slew rates specified by the manufacturer (LMC6064: $35\,V/ms$, AD824A: $2\,V/\mu s$), the AD824A enables a much faster current regulation than the LMC6064 (see fig. 4.3).

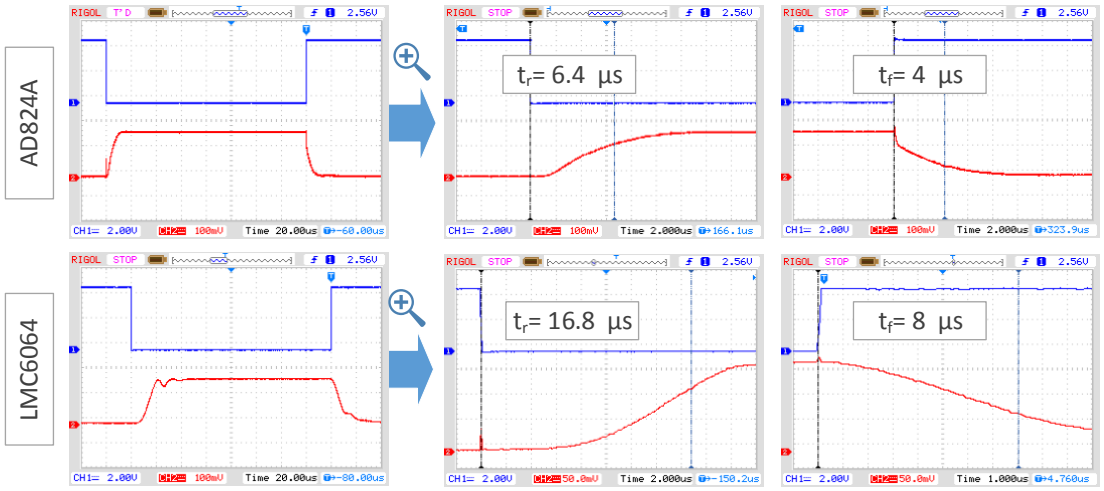

Figure 4.3: Evaluation of LMC6064 and AD824A speed. Blue: PWM reference, red: modulated LED current signal. Measured over 1Ω resistance with inverted analog switching logic using DAC level 4.

With a rise time of $t_r = 6.4\,\mu s$ and a fall time of $t_f = 4\,\mu s$, the AD824A provides more than twice the edge steepness of the square-wave current signal compared to the LMC6064 ($t_r = 16.8\,\mu s$, $t_f = 8\,\mu s$). Also, in the LMC6064, higher transient oscillation and settling were observed than in the AD824A. Thus, despite higher costs, the AD824A was selected for the current regulator design.

To minimize transient oscillation and settling times, a decoupling capacitor was introduced between operational amplifier negative input and output (see also subsection 3.4.4). To determine the optimal value of this capacitor, both LTSpice simulations and experiments were conducted. Fig. 4.4 shows an excerpt of a series of measurements that has been conducted for this purpose. For two current levels (DAC lvl 2 = $80\,mA$ and DAC lvl 4 = $100\,mA$) the shape of the regulated current signal was investigated with C= 0, $4.7\,pF$, $10\,pF$, $33\,pF$, $100\,pF$, $200\,pF$ and $330\,pF$ (see fig. A.14 for a comparison of all measurements).

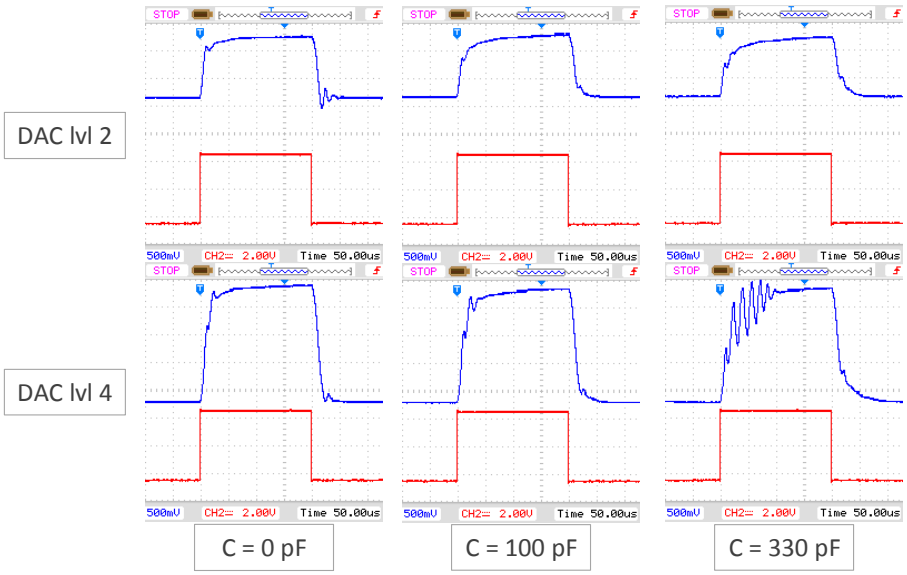

Figure 4.4: Evaluation of optimal current regulator decoupling capacitor value (excerpt). Blue: voltage (implying LED current) measured at LED cathode, red: PWM modulation reference.

The experimental results indicated that for lower current levels the use of low decoupling capacities intensifies oscillations during the settling of the signal. For higher current levels, higher decoupling capacities increase the transient oscillation of the signal. To optimize the signal for minimal oscillations and maximal edge steepness for all DAC levels, the decoupling capacitor value was chosen to be $100\,pF$.

Figure 4.5 shows the shape of a DAC lvl 4 regulated and $3.125\,kHz$ modulated square-wave current signal resulting from the final current regulator design.

4.1.4 Lock-In Detection

Using the mathematical description of lock-in modulation/demodulation from section 3.4.3, the effects of phase shifts between the PWM reference and the signal at the lock-in

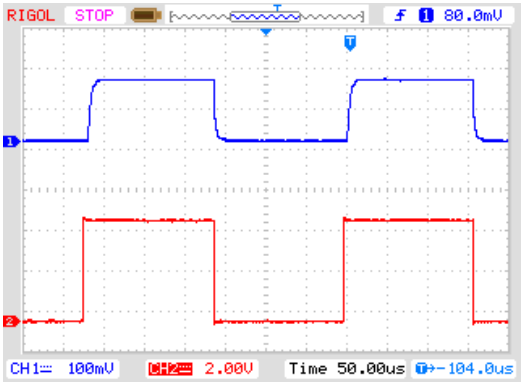

Figure 4.5: Shape of modulated current signal at DAC level 4. Blue: Current measured over 1Ω resistor, red: PWM reference.

demodulator input due to propagation delays were evaluated.

From equation 3.16 it is obvious that the signal's attenuation resulting from a phase shift is proportional to the cosine of this phase shift: $\cos(\Phi_S - \Phi_R)$. With

$$\Phi_S - \Phi_R = \frac{\Delta t}{T} \cdot 2\pi, \tag{4.1}$$

Δt being the total propagation delay of the signal and T being the cycle duration, the resulting attenuation A of the signal caused from lock-in demodulation can be estimated using

$$A = \cos\left(\frac{\Delta t}{T} \cdot 2\pi\right). \tag{4.2}$$

To minimize effects due to propagation delays, all hardware elements in the signal path were selected with respect to high-speed/low delay times. Figure 4.6 shows a measurement of the total resulting phase shift between the PWM reference and the demodulator input in the final hardware design.
For an approximation of the total effective phase shift, delays between the signals were measured at the 50% levels of both rising and falling edges respectively. The total phase shift effecting the attenuation by demodulation is the sum of times where signal and reference levels do not overlap, thus $\Delta t = t_{dr} + t_{df} = 18.5 + 7.2\,\mu\,s$. This phase shift results mainly from the total propagation delays from demultiplexer, analog switches, current regulator, photodetector and PGA. Using eq. 4.2, the attenuation factor A caused by non-phase-synchronous demodulation of the signal with a cycle duration of $T = 320\,\mu s$ is estimated as approximately 0.875.

Fig. 4.7 depicts the effect of the phase shift on the demodulated signal.
The pre-amplified signal from the photodetector (red) is multiplied with the sign of the square-wave reference (not in the picture). In the demodulated signal (blue), the phase shift results in an inversion of parts of the input signal carrying functional information to below-zero levels and parts of the noise and stray light signal to a positive level respectively.

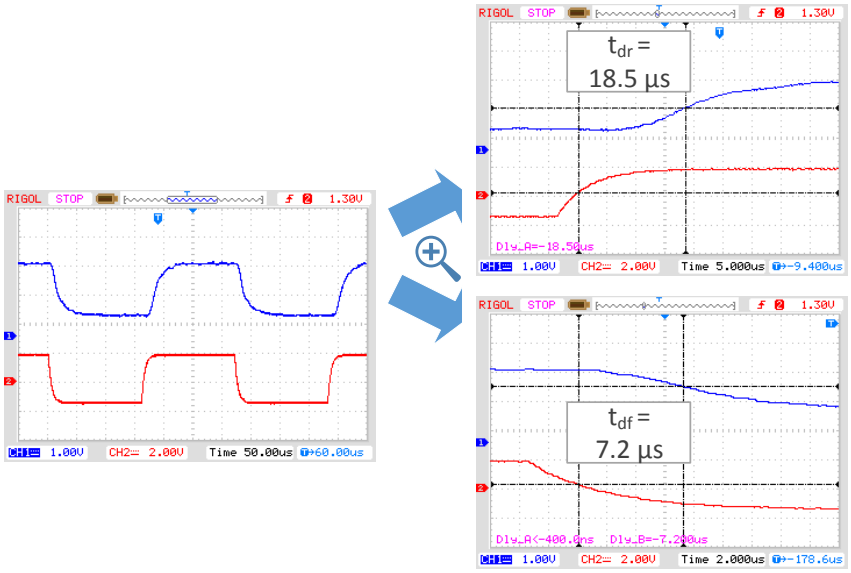

Figure 4.6: Measurement of total phase shift between PWM reference input and demodulator input. Blue: signal at demodulator input, red: PWM reference input.

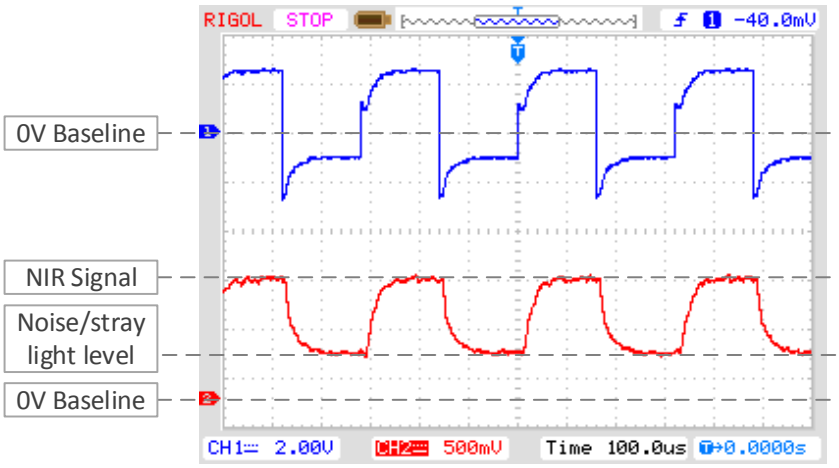

Figure 4.7: Attenuation effect of phase shift on demodulation. Blue: demodulated signal, red: lock-in input signal.

To further minimize the attenuation resulting from phase shift, four approaches are possible:

1. Using digital lock-in amplification,
2. Using two-phase quadrature amplification,
3. Using even faster hardware components in the signal path,
4. Adding an arbitrary shift in the reference signal path using elements for small delays.

The 3rd and 4th approaches offer a promising perspective, as only minor concept design adaption is necessary. Especially the programmable gain amplifier's (PGA) contribution

to the phase delay can be reduced significantly: It was measured as 7 μs and 4.5 μs for rising and falling edges respectively.

4.1.5 System Drift

Several factors were considered to be possible sources of system drift:

- Changes in the 1 Ω current regulation resistance due to temperature changes resulting in variations of the LED current.
- Changes in the total radiated power of the LEDs despite constant currents due to temperature changes in the semiconductor junction.
- Supply voltage variations.

Changes in stray light, amplifier and thermal resistor noise are strongly suppressed by the lock-in amplification process.
To minimize signal drifts resulting from changes in the 1 Ω current regulator resistance, Panasonic current sensing resistors with a low temperature coefficient of resistance ($TCR = \pm 50 \cdot 10^{-6}/°C$) were chosen.
To evaluate the effective overall system drift, the fNIRS module was placed in an opaque closed box to screen it from background radiation. With a fixed module position and thus fixed NIR light reflection intensity in the box, the signal of one DAC level 4 active channel in speed mode was constantly acquired for 10 minutes (see fig. 4.8).

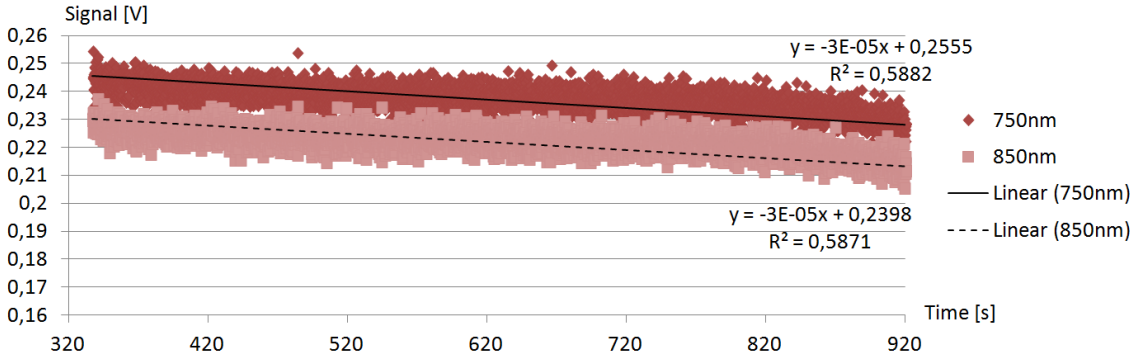

Figure 4.8: Overall system drift characterized by linear least squares approximation.

The drifts of both wavelength signals were approximated using a linear least squares regression method. The regression yielded a negative drift coefficient of $C_D = -3{\cdot}10^{-5}\, V/s$ for both channels when continuously active.
As a significant rise in temperature in the power supply was observed during longer acquisition times, the same experimental setup was repeated with the mainboard and power supply unit being cooled by a fan. The prevention of PCB heating and thus a significantly smaller temperature increase in the analog-to-digital converter was expected to improve the above-mentioned drift characteristics. Figure 4.9 shows the result for a 20-minutes acquisition period.
Using the same linear least squares regression method, the approximated function revealed significantly lower drift: With a resulting negative drift coefficient of $C_{Dc} = -1 \cdot 10^{-6}\, V/s$ for continuous acquisition of one active channel in speed mode, the system being cooled, the drift effects were reduced by more than one order.

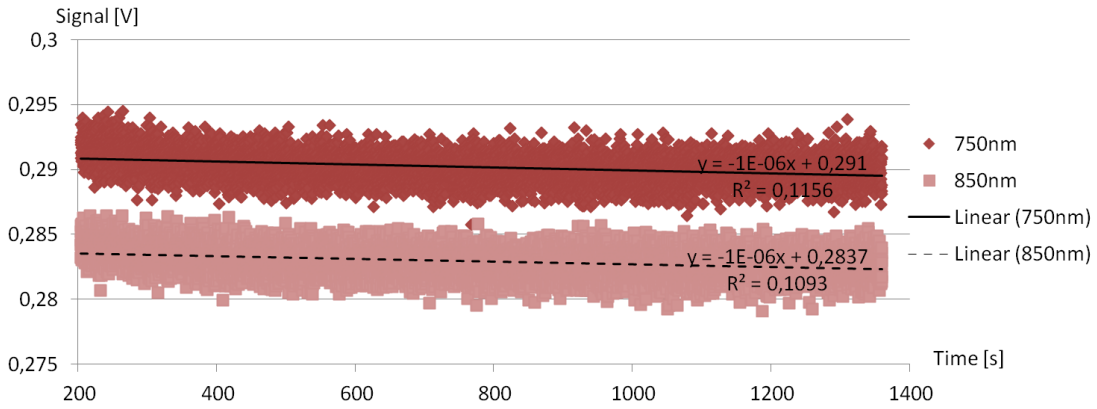

Figure 4.9: Overall system drift with fan cooled mainboard/power supply.

Comparing both measurements allows further discrimination of the main factors influencing the overall system drift: The strongest factor influencing drift performance seems to be the temperature increase of the ADC unit caused by power supply heating.
The NIRS module itself shows a very low drift of max. $-10^{-6}\,V/s$ which is in the order of the TCR of the $1\,\Omega$ current regulator sensing resistors. So far, the changes in the total radiated power of the LEDs resulting from temperature changes seem to be negligible or comparable to the influence of current sensing resistor heating effects.

4.2 Physiological Verification of the System

4.2.1 Qualitative Physiological Signals: Pulse and local Blood Pressure

To verify that the instrument's output NIRS signal contains physiological information of significant strength, simple qualitative experiments were conducted:

Fig. 4.10 depicts the effect of overall blood pressure in the head on the signal, leading, amongst others, to an increase in cerebral blood volume (CBV). To influence the blood pressure in the head, the short experimental protocol was as follows: First, the subject inhaled, followed by piping down together with contracting the diaphragm (Start) for a period of 5 seconds. This period was then followed by 10 seconds of relaxation (Relax) and normal breathing until the start of the next trial.
A strong fall of the optical signal strength resulting from increased blood volume in the head can be observed instantly after each starting period. During relaxation periods, the signal immediately recovers with about the same speed to the baseline of the experiment's start as the blood volume in the head normalizes.

The visibility and strength of pulse artifacts in the overall optical signal is an indicator for the signal quality and has been widely documented in NIRS literature, as the pulse artifact's strength is in the order of functional brain activity influences. Thus, a clear pulse artifact is a first indicator for sufficient signal quality to measure brain activation. Fig. 4.11 shows an example of the clearly visible pulse artifacts in the signal during a cognitive relaxation period.

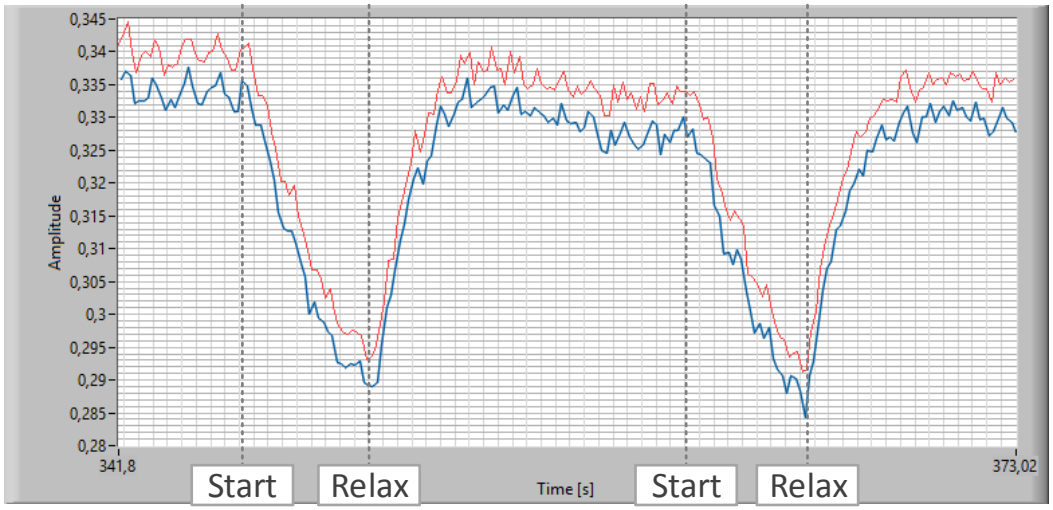

Figure 4.10: Influence of blood pressure variations in the head (cerebral blood volume (CBV)), raw signal.

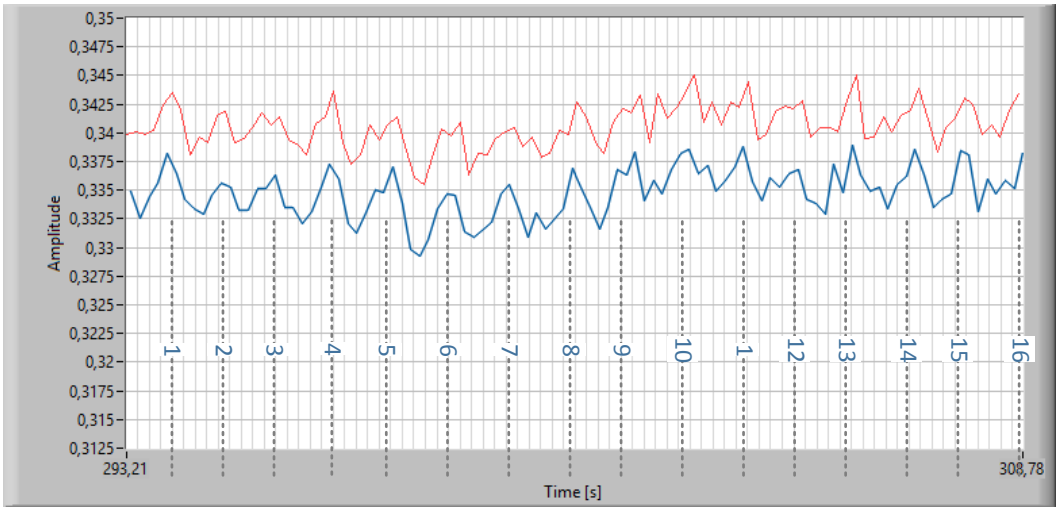

Figure 4.11: Pulse artifact in the raw signal.

The visible heart rate of approx. $\frac{16\,pulses}{15\,s} = 64\,pulses/min$ in the experiment was verified by a 60-second pulse measurement with a heart rate result of $65\,pulses/min$.

4.2.2 BCI Trials: Mental Arithmetics

For verification of the device's capability to measure functional brain activity, 32-trial BCI classification experiments were conducted both with the designed fNIRS instrument and an Oxymon Mk III reference fNIRS system from Artinis Medical systems. The Oxy-

mon Mk III uses laser diodes with 765 nm and 856 nm with fiber optical guided optodes and is a commercial tabletop system with two sensors and 4 emitters.

Both instrument's performances were evaluated on two subjects with mental arithmetics based experiments measuring brain activity at the prefrontal cortex:
The first experiment was conducted using a prototype version of the designed fNIRS instrument and single channel acquisition at 7 Hz and was repeated with a single channel 10 Hz acquisition using the Oxymon reference system.
The second experiment was conducted using the final fNIRS instrument with two channels sampled at 8 Hz each and repeated with a two-channel 10 Hz acquisition using the Oxymon system.

For all experiments, the following protocol was followed:
With an emitter-detector distance of 3.5 cm, the light emitting probes were placed approximately on the places of Fp1 & Fp2 of the international 10-20-system and the light detector placed approximately on AFz (see fig. 4.12). In the single channel experiment, only Fp1 versus AFz was measured.

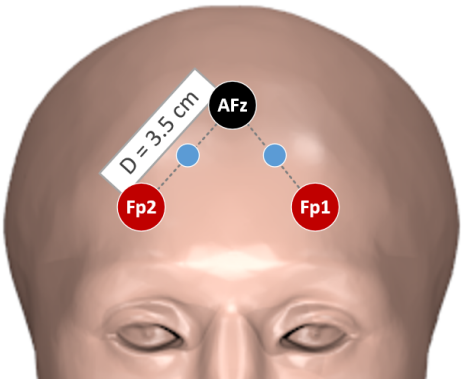

Figure 4.12: Optode placement for BCI experiments. Red: NIR light emitter placement, black: NIR detector placement, blue: approximate point of maximum sensitivity.

Using a Cognitive Systems Lab (CSL) BCI trial Matlab script, the fNIRS signal was recorded during 32 trials of 8 seconds each, with the subject alternately executing a mental arithmetic task (16 trials) and relaxing (16 trials). For the mental arithmetic tasks, the subject was given a random number between $100 - 9999$ at the beginning of each 8 second arithmetic trial and iteratively subtracted the number 17 until the end of the trial.

For evaluation of the data, a signal processing, a feature extraction and a classification step were performed.
In the signal processing step, biological artifacts, mainly the heartbeat (see section 2.2), were reduced using a digital filter. The signal was filtered by an elliptic IIR 0.7 Hz low-pass filter of the order 6 in both the forward and reverse directions.
For feature extraction, HbO and HbR were calculated from the raw data using the modified Beer-Lambert Law. Then, for each channel (and both HbO and HbR) of each trial, the slope of a least-squares-fitted line to the signal time series was calculated, resulting in a 4-dimensional feature vector per trial.

For classification, a Linear Discriminant Analysis (LDA) classifier using leave-one-out cross-validation was applied. To do so, one trial of the data of one subject was left out for evaluation in a round-robin manner, while the remaining data was used for training.

For the single-channel experiment, the classification results were a cross validation accuracy of 62.9% with a normalized standard deviation of $\sigma_N = \frac{0.492}{\sqrt{32}} = 0.087$ for the prototype fNIRS system and a cross validation accuracy of 69.23% with a normalized standard deviation of $\sigma_N = \frac{0.471}{\sqrt{32}} = 0.083$ for the Oxymon Mk III reference system.
For the two-channel experiment, the classification results were a cross validation accuracy of 75.0% with a normalized standard deviation of $\sigma_N = \frac{0.440}{\sqrt{32}} = 0.078$ for the final fNIRS system and a cross validation accuracy of 65.63% with a normalized standard deviation of $\sigma_N = \frac{0.483}{\sqrt{32}} = 0.085$ for the Oxymon Mk III reference system.
The presented accuracies are averaged over all folds.
Figure 4.13 shows the average signal responses (MBLL concentrations) of the trials for the two-channel experiment.

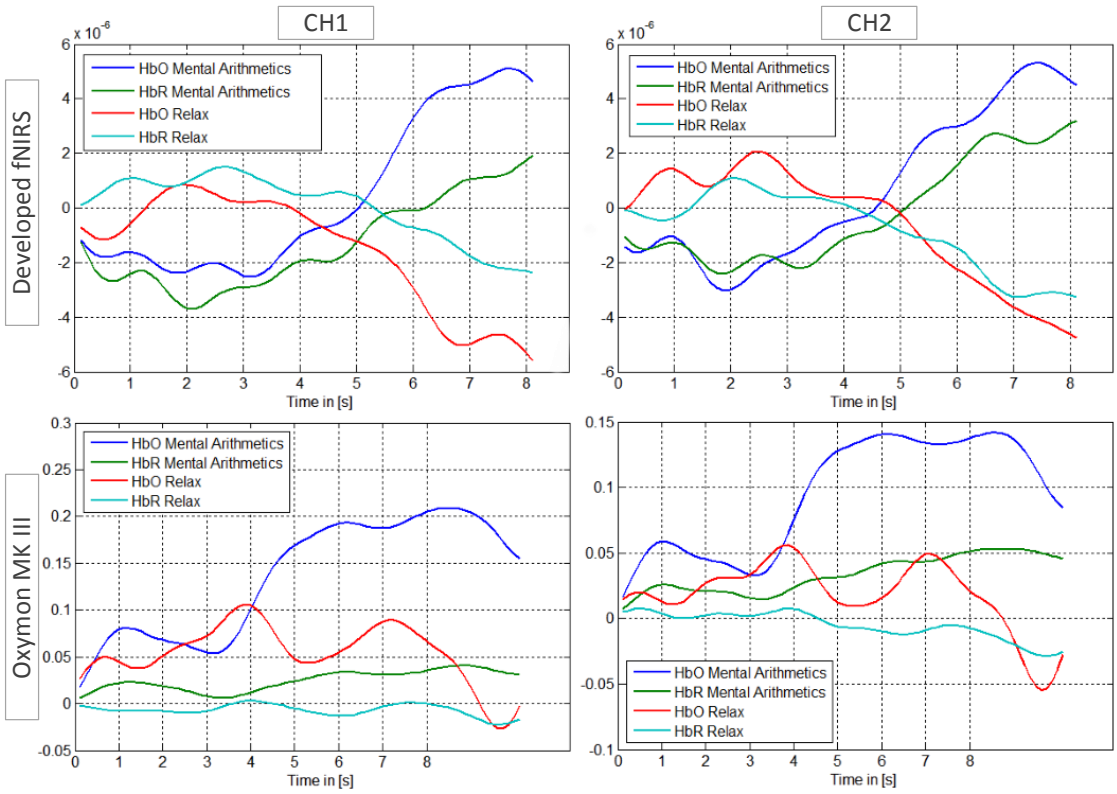

Figure 4.13: Average signal responses of the BCI trials for both channels and both instruments.

The experiments showed similar results for both systems regarding averaged signal trends and classification accuracy. While the commercial Oxymon system performed better in the single-channel experiment, the classification accuracy for the two-channel experiment using the developed fNIRS instrument was 10% higher than with the Oxymon instrument.

5

Results and Discussion

The following chapter will provide a brief system overview. Afterwards, the scope and limitations of the fNIRS instrument design will be discussed.

5.1 System Overview

In the course of this work, several prototypes and a final version of a modular multi-channel fNIRS system based on continuous wave technology were designed. Using lock-in detection, programmable amplification and adjustable regulated LED currents, the instrument is suitable for functional brain activity indication based on fNIRS signals.
Figure 5.1 shows the final fNIRS instrument that was implemented in this work.

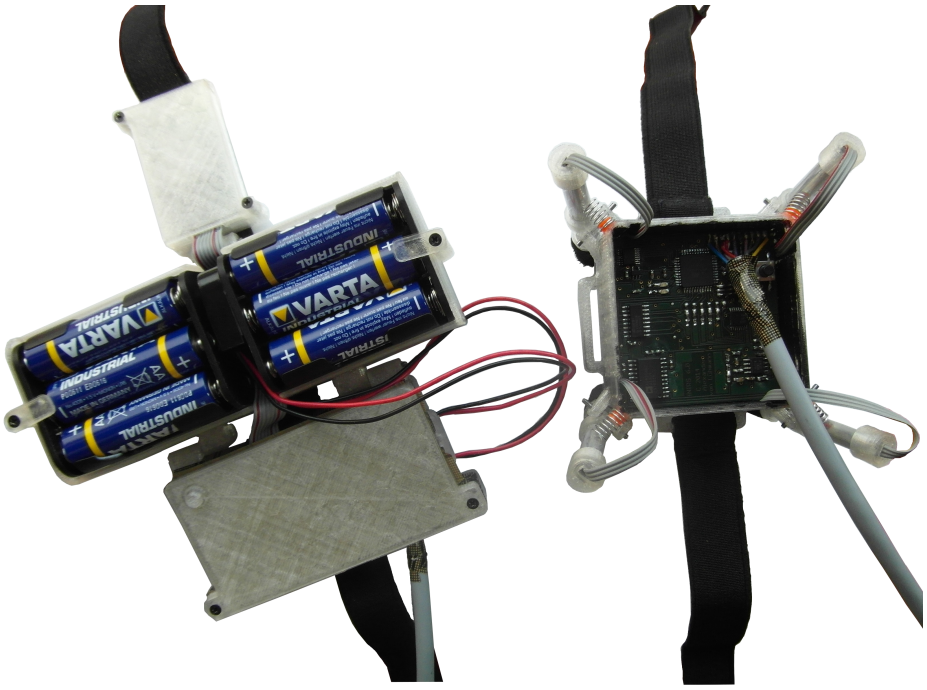

Figure 5.1: Finished NIRS instrument. Left: multi-unit mainboard module for upper arm, right: NIRS module.

The final version consists of a mainboard, a communication module and a battery package that are encapsulated by custom 3D-printed housing elements interconnected by rotary joints, and a 4-channel spring-loaded fNIRS module. Wearing the mainboard module on the upper arm and the fNIRS module on the head using flexible ribbons and hook-and-loop fastener, the user can move freely and is bothered as little as possible by the instrument.
The electrical and functional characteristics of the fNIRS instrument are summarized in tab. 5.1.

Power Charact.	Power Consumption	max: $200\,mA$, stand-by: $80\,mA$
	Battery Supply Voltage	max: $\pm 10\,V$, min: $\pm 7.5\,V$
Signal Charact.	Meas. Wavelengths:	$750\,nm$ & $850\,nm$
	LED Type	Epitex L750-850-04A
	Photodiode Type	Burr-Brown OPT101
	Max. Sampling Rate	$14\,Hz/7\,Hz$
	Conversion Depth	$16\,Bit$
	Signal Drift fNIRS module max.	approx. $-1 \cdot 10^{-6}\,V/s$
	Overall Signal Drift without cooling	approx. $-3 \cdot 10^{-5}\,V/s$
Instrument Charact.	Lock-In Amplification	
	Programmable Amplification	$G = 0.688 - 88$
	Time-Division Multiplex	
	Current Regulation	
	Current Adjustment	4 Levels: 25, 50, 80, $100\,mA$
Communic. Interfaces	Mainboard: UART	9600 bps, 8 data, 1 stop, no parity
	UART Access	Bluetooth (AMB2300)/Serial Cable
	8 Characters Control Set	”G”,”S”,”E”,”C”,”R”,”T”,”P”,”H”
	23 Bytes CSV Output Format	|M#;C#;L#;S#;ADC;Timer;CRLF|
	NIRS Module: 5 Bit parallel	Bit3:0 |RST|TRIG|CH1|CH0|

Table 5.1: Characteristics of NIRS instrument.

The instrument's hardware functionality was constantly evaluated and improved during the design process of evaluation, prototype and final versions. The main results of these iterative design and evaluation steps are

- A new stand-alone fNIRS system concept based on modularity and scalability
- An optimized adjustable current regulator and modulation circuit based on AD824A high-precision amplifiers with negative decoupling.
- A lock-in-based signal extraction module with programmable amplification and $2\,Hz$ 3rd-order low-pass filter
- An UART-based Bluetooth/Serial communication interface for instrument control, signal acquisition and data transmission
- A 4-channel spring-loaded mechanical concept for NIRS probe attachment for better robustness against movement artifacts and higher user comfort.

The overall system drift for the single fNIRS module was specified to be maximum $-1 \cdot 10^{-6}$. For the overall instrument without additional cooling, a significantly higher drift of approximately $-3 \cdot 10^{-5}$ was measured. The main influencing factor of system drift was determined as the temperature increase of the ADC caused by power supply heating.
The verification of the hardware functionality was done by acquiring qualitative physiological data (pulse, blood pressure/cerebral blood volume) and quantitative BCI experiments with a commercial laser-diode-based reference system (Artinis Medical Systems Oxymon Mk III) were conducted. In two 32-trial mental arithmetic experiments with two subjects, similar signal trends and classification accuracy (mobile fNIRS: 62.9% and 75.0%, Oxymon: 69.23% and 65.63%) indicated comparable performance and the instrument's capability of measuring functional brain activity.

5.2 Scope and Limitations

While the hardware evaluation and physiological verification of the designed fNIRS instrument indicates a sufficient signal quality and hardware functionality, there are still several elements in the design that can be further optimized for better instrument performance:

- As this work focused on the system concept and signal generation and extraction elements, the design of the **power supply** was secondary and can be further optimized. Even though the implemented linear-voltage-regulator-based symmetric supply appears to be sufficient at this point, several improvements are suggested for later versions of the instrument:
  A new design for a next-generation power supply should include additional high-frequency filters against noise pickup from external sources and enhanced stabilization to minimize LED current modulation influences on the rest of the system. Also, the use of more efficient voltage regulators would be desirable to further enhance battery life and decrease heating effects, which would minimize the system drift influences resulting from ADC temperature rise. Either active or passive cooling of the power supply unit or a physical/thermal separation of the power supply and ADC unit could further reduce system drifts.
- A considerable improvement of the instrument's performance can be achieved by enhancing the mainboard's **analog-to-digital converter** functionality. As became apparent during the iterative design process, the currently implemented ADC (LTC2486) offers high conversion depth but significantly limits the maximum time resolution that can be used for the instrument's channels. As the maximum sampling rate of $14\,Hz$ has to be shared by all active channels, the time resolution of each signal significantly decreases with each additional channel that is used. Especially, when the Nyquist theorem is to be applied with respect to the $2\,Hz$ 3rd-order low-pass filter, not all 4 channels can be used simultaneously with the $16\,Bit$ ADC.
  However, this big disadvantage can be easily eradicated by simply improving the current mainboard design to a next-generation design with either several parallel ADCs or a new fast ADC with sufficient quantization depth. The only reasons this was not done in the final instrument were the limited time and expenses that exceeded the scope of this Master's thesis.

In a first step, however, the $10\,Bit$ $150\,ksps$ ADC module of the mainboard's microcontroller was additionally implemented for a higher sampling rate in trade-off with lower quantization depth. BCI trials showed sufficient system performance despite the low quantization depth, probably based on the high pre-amplification of the detected optical signal before analog-to-digital conversion.
This reveals a positive aspect of the instrument's design concept: With the NIRS module being designed for stand-alone usage, any control and acquisition equipment can be used and the performance is adaptable to user requirements.

- As the evaluation of the **lock-in detector** revealed, the attenuation of the detected signal due to a phase shift is acceptable but can be further minimized. To improve the lock-in performance, an analog adjustment of the PWM reference phase could be implemented. This would enable overall phase shift compensation.
  Alternatively, a potentially superior approach for a next-generation design could be developed using the microcontroller for digital lock-in demodulation. This bears several advantages: reduced cost of hardware components, reduced power consumption and an adjustable phase shift correction and thus higher precision.

In the course of the experiments, some advantages of the instrument regarding user comfort and usability were noticed: The use of the commercial reference system required longer preparation times for optode fixation and was often uncomfortable and static because of the weight of the optical fiber guides and the lack of cushioning of the optodes. In contrast, the wearable system designed in this work could be applied within several seconds and was generally perceived less cumbersome during the experiments.

6

Summary and Outlook

Functional Near-Infrared Spectroscopy is an emerging technology that provides a new modality for brain activity measurements. With advantages such as hazard-free application, motion artifact robustness and the possibility to miniaturize hardware, fNIRS may enable new applications in the BCI context, in clinical tools and diagnosis and further contribute to new insights in brain research and neuroscience.

In this work, a modular, multichannel, wireless fNIRS instrument using continuous wave methodology was designed and evaluated. Consisting of a NIRS module and a control and acquisition mainboard, the instrument provides stand-alone fNIRS functionality. Using UART interface Bluetooth data transmission and a battery power supply, the system is suitable for mobile applications.

The hardware design of the instrument focused on a lock-in detection approach with programmable amplification and a silicon NIR light detector with integrated trans-impedance amplifier for noise reduction. For optimal signal performance, two NIR light wavelengths ($750 + 850\,nm$) were chosen in accordance with the current state of research with regard to optimal NIRS wavelength selection. For lock-in modulation, current adjustment and regulation, a high-precision current regulator concept was iteratively designed and improved.
Complementary to the fNIRS module concept that provides stand-alone usage via a custom $4\,Bit$ parallel interface, a mainboard for module control and acquisition of the analog fNIRS signal was designed. Providing the fNIRS module supply voltages from a symmetric regulated voltage supply, the mainboard also serves as acquisition unit (using a 4-channel $16\,Bit$ ADC) and communication interface. With the implemented set of 8 ASCII control bytes, the instrument can be used via any serial UART communication interface such as an operating system's HyperTerminal, the MathWorks Matlab serial interface or a stand-alone executable LabView graphical user interface that was designed in this work.

The software design is based on two Atmel Corp. AVR microcontrollers. On the NIRS module, the first microcontroller controls the PGA, current adjustment, and channel multiplexer, creates a $3.125\,kHz$ modulation PWM square-wave reference and processes the incoming control signals based on an interrupt routine design.
On the mainboard, the second microcontroller provides SPI and UART interfaces for ADC data acquisition and user communication, processes user controls and generates control signals for the fNIRS modules.

For data communication, logging and processing, the LabView graphical user interface was developed. It provides simple instrument control, graphical display of the acquired fNIRS data and a data saving routine for file generation including a header carrying instrument configuration information and the acquired data for further post-processing and documentation.

Mechanical designs were done using 3D printing technology and CAD software.
The fNIRS module body housing is based on a double spring-loaded quad-probe design for good mechanical adaption to the surface of the head while ensuring irradiation and detection perpendicular to the surface and maximizing user comfort.
The body housing of the mainboard unit consists of three parts that are connected via rotary joints and carry the Bluetooth module, the mainboard and battery packs. Using flexible ribbon and hook-and-loop fastener, the mainboard unit can easily be fixated on the upper arm of a subject wearing the fNIRS instrument.

The instrument's hardware was evaluated for signal and noise performance and verified by acquisition of physiological data.
Hardware evaluation indicated that there is still room for improvement in the lock-in amplification module, power supply design, signal acquisition and drift properties of the instrument.
To improve the lock-in performance, attenuation effects resulting from phase shifts between modulation reference and detected signal can further be minimized, e.g. by using digital lock-in demodulation or analog phase correction. The power supply design can further be improved by better decoupling from the high-frequency current modulation impacts and external electrical interference. To use several fNIRS modules/many active channels at the same time, a larger number or faster ADCs have to be implemented on a next-level mainboard design. For static solutions, any number of stand-alone fNIRS modules can be used and controlled, e.g. with LabView DAQ equipment or any other data acquisition equipment that allows customized parallel control of the modules interface.
The overall system's signal drift for continuous use of one channel in speed mode was evaluated and linearly approximated as $-3 \cdot 10^5\, V/s$. The main factor causing this drift was determined to be the ADC's temperature increase caused by power supply heating on the mainboard. The drift of the stand-alone fNIRS module was evaluated as approx. $-1 \cdot 10^{-6}\, V/s$, which is in the order of the current regulator sensing resistance's TCRs. To further reduce the overall drift, thermal decoupling (physical separation) of the ADC from the power supply or power supply cooling techniques such as passive heat conduction elements or a mini fan integrated in the body housing could be applied.

For verification of the physiological value of the fNIRS instrument's signals, qualitative examination of the effects of heart rate and head blood pressure on the signals were conducted and confirmed the basic functionality of the instrument. To compare the designed instrument with commercially available fNIRS instrumentation, brain computer interface experiments for brain activity acquisition during mental arithmetic were conducted. The results showed comparable system performance, the classification results showing a better cross validation accuracy (CVA) of 69.23% (Oxymon) vs. 62.9% (mobile fNIRS) for the commercial reference system in single-channel trials and a better performance of the designed mobile fNIRS system in two-channel trials (CVA of 75.0% (mobile fNIRS) vs. 65.63% (Oxymon)).

The evaluation of the fNIRS instrument for mobile, modular, stand-alone brain activity measurements makes the design approach promising for future applications.

A

Appendix A

Overview of NIRS-systems from research

Type	**Lock-In**	**TDM**	**# CH**	λ **[nm]**	**LS Type**	**DET Type**	**d [cm]**	**Portable**	**Wireless**	**Attachment**	**ADC**	**Ref.**
CW	No	Yes	32	735 850	32 LED	1 APD	4	Yes	No	neoprene hood	20 Hz 16 Bit	Lareau 2011 [38]
CW	Yes	No	22	754 830	8 LD	8 APD	3	Yes	No	600g headset		Kiguchi 2012 [48]
CW	Yes	Yes		760 850	8 LED	8 PD	..3..	Yes	No	EEG-Cap	6.25 Hz	Piper 2013 [49]
CW	No	Yes	32+	760 850	32 LED	4 PD	2/4	No	Yes	EEG-NIRS-plastic chain	8 Hz 16 Bit	Safaie 2013 [15]
CW	No		16	730 805 850	4 LED	10 PD	2.5	No	No	Flex. PCB with cushioning	2 Hz	Bunce 2006 [14]
CW	Yes		1	670 890	1 LED	1 APD	3	No	No	Flex. Strap	250 Hz	Bauernfeind 2008 [50]
CW	Yes		288	780 830	18 LD	16 PD	4-8	No	No		0.25 Hz 16 Bit	Siegel 1999 [44]
CW	No	Yes	3	780 810 830	3 LD	1 PD						Benni 1995 [32]

Table A.1: NIRS-Systems overview (I): CW = Continuous Wave, TD = Time Domain, FD = Frequency Domain, TDM = Time-Division Multiplex, # CH = Number of Channels, LS Type = Light Source Type: LED = Laser Emitting Diode, LD = Laser Diode, VCEL = Vertical-cavity surface-emitting laser, DET Type = Detector Type: APD = Avalanche Photodiode, PD = Silicium Photodiode, PMT = Photo Multiplier Tube, PIN = Positive intrinsic negative photodiode, d = source - detector distance: ..x.. variable, ADC = Sampling rate and quantization depth.

Type	**Lock-In**	**TDM**	**# CH**	**λ [nm]**	**LS Type**	**DET Type**	**d [cm]**	**Portable**	**Wireless**	**Attachment**	**ADC**	**Ref.**
FD	Yes		3	775 810 850 905	1 LD	3 PMT	5	No	No			Rolfe 2000 [30]
FD	Yes		2	780 850	2 LD	1 PIN		No	No			Rolfe 2001 [51]
CW			56	780 880	48 LED	14 PD	..1..	No	No	Flex. PCB with cushioning	3 Hz	Vaithianathan 2004 [58]
CW	Yes	Yes	22	790 850	16 VCEL	8 PD	3	Yes	No			Atsumori 2007 [52]
CW	Yes			700 880	LED	APD	3-4	No	No		100 Hz 16 Bit	Coyle 2004 [18]
CW				735 850	LED	8 PD	3	Yes	Yes			Chang 2011 [56]
CW	No	Yes	2	730 850	1 LED	2 PD	2	Yes	No	Flexible PCB with sticky tape	10 Hz 12 Bit	Bozkurt 2005 [53]
CW	Yes			760 880	LED	APD	3-4	No	No	Seat fixation	100 Hz 16 Bit	Coyle 2007 [20]
CW	No			778 813 867 904	LD	PMT		No	No			Cope 1988, 1991[3], [21]
CW	No	Yes	1	730 804 850	LED	PD	3,5	Yes	No	Velco straps	23 Hz 18 Bit	Chenier 2007 [54]
CW			16		8 LED	2 PD	1 + 0.5x	Yes	No	embedded silicon patch	2 Hz 16 Bit	Rajkumar 2012 [59]
CW	Yes	Yes	32+	785 830	32 LD	32 APD		No	No			Boas 2001 [45]
CW	Yes		12	760 880	24 LED	3 APD	3	No	No		10 Hz 24 Bit	Soraghan 2008 [19]
CW		Yes		760 850	LED	PD		Yes	No		40 Hz	Zhang 2009 [55]

Table A.2: NIRS-Systems overview (II): CW = Continuous Wave, TD = Time Domain, FD = Frequency Domain, TDM = Time-Division Multiplex, # CH = Number of Channels, LS Type = Light Source Type: LED = Laser Emitting Diode, LD = Laser Diode, VCEL = Vertical-cavity surface-emitting laser, DET Type = Detector Type: APD = Avalanche Photodiode, PD = Silicium Photodiode, PMT = Photo Multiplier Tube, PIN = Positive intrinsic negative photodiode, d = source - detector distance: ..x.. variable, ADC = Sampling rate and quantization depth.

	Device	(Manufacturer), country	Time-res. [Hz]	#Emitter	#Detector	MUX	SDS [mm]	E-tech	Wavelengths [nm]	D-tech	Data	Wear	CE
D1	OXYMON MkIII[a]	(Artinis), Netherlands	250	32	16	t	a	Laser	760, 850*	APD	Raw	n	y
D2	PortaLite	(Artinis), Netherlands	50	3	1	t	20 + 25 / 30 + 35 + 40	LED	760, 850*	PD	Raw	y	y
D3	fNIR100	(fNIR Devices), USA	2	1/1/4	2/4/10	t	20/25/25	LED	730, 850		Hb	n	n
D4	fNIR100w	(fNIR Devices), USA	2	1	2/4	t	20/25	LED	730, 850		Hb	y	n
D5	ETG-4000	(Hitachi), Japan	10	18	8	f	20/30	Laser	695, 830	APD	Raw	n	y
D6	ETG-7100	(Hitachi), Japan	10	40	40	f	20/30	Laser	695, 830	APD	Raw	n	y
D7	WOT[b]	(Hitachi), Japan	5	8	8	t + f	30	Laser	705, 830	PD	Raw	y	n*
D8	Genie	(MRRA), USA	5.02	4 to16	8 to 32	c	a	LED	700, 830	PD	Raw	y	n
D9	NIRScout	(NIRx), USA	6.25 to 62.5	8 or 16	4 to 24	t + f	a	LED	760, 850	PD	Raw	n	y
D10	NIRScoutX	(NIRx), USA	6.25 to 62.5	48	32	t + f	a	LED	760, 850	PD	Raw	n	y
D11	NIRSport	(NIRx), USA	6.25 to 62.5	8	8	t + f	a	LED	760, 850	PD	Raw	y	y
D12	Brainsight NIRS	(Rogue Research), Canada	100	4 to16	8 to 32	f	a	Laser	685, 830, (808)*	APD	Raw	n	n*
D13	FOIRE-3000	(Shimadzu), Japan	7.5 to 40	4 to 16	4 to 16	t	a	Laser	780, 805, 830	PMT	OD	n	n
D14	OEG-SpO2	(Spectratech), Japan	1.52/12.2	6	6	c	30/25/15–40	LED	770, 840	PD	Raw	y*	n*
D15	CW6	(TechEn), USA	10 to 50	4 to 48	8 to 32	f	a	Laser	690, 830*	APD	Raw	n	y
D16	UCL Optical Topography System[c]	(University College London), UK	10 to 160	16	16	f	a	Laser	780, 850	APD	Raw	n	n
D17	Imagent	(ISS), USA	16 to 60	16 or 32	4 or 8	t	a	Laser	690, 830	PMT	Raw	n	y

[a] van der Sluijs et al. (1998).
[b] Atsumori et al. (2009).
[c] Everdell et al. (2005).

Figure A.1: Overview of commercial NIRS-Devices, taken from [11].

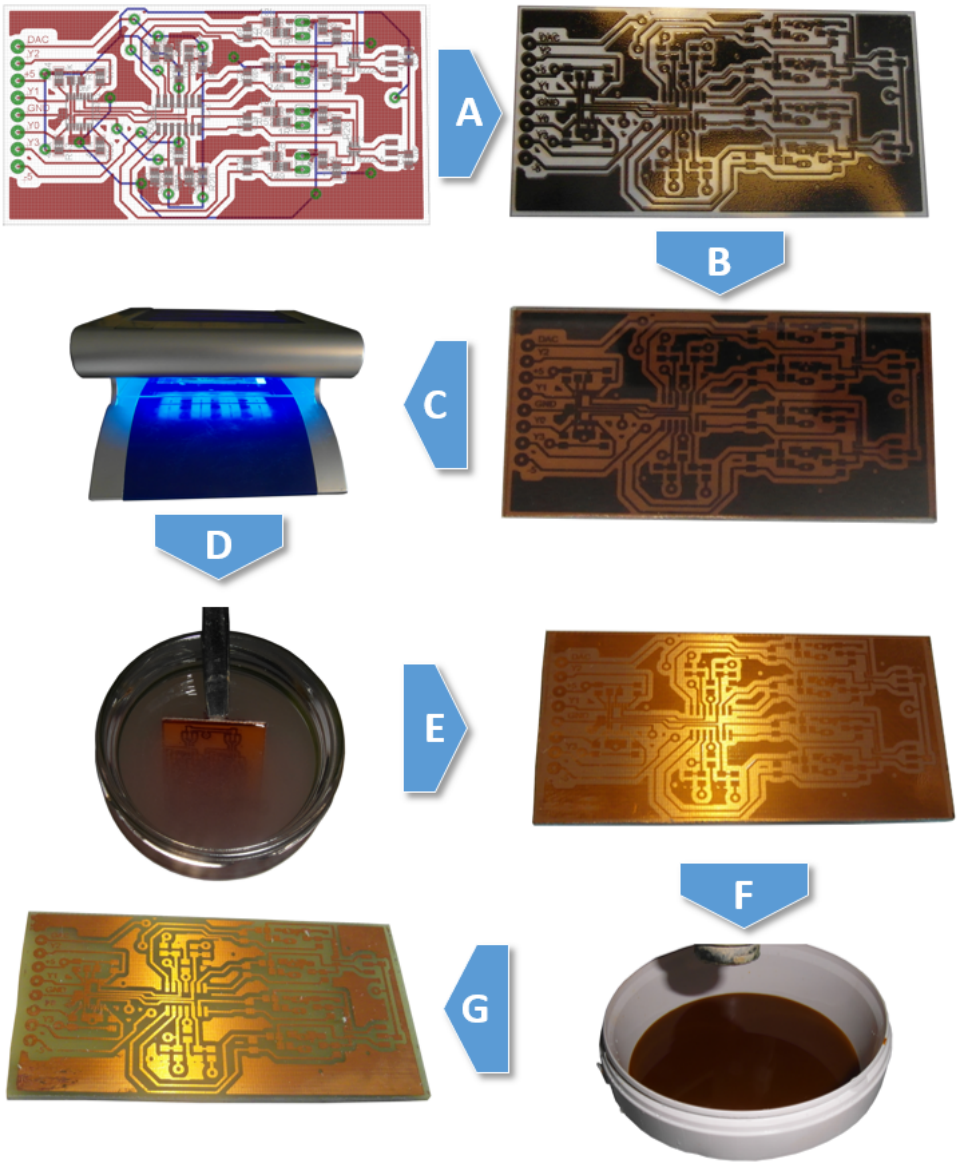

Figure A.2: PCB prototyping process. A: printing layout on plastic film, B: covering copper PCB, C: UV-light exposure, D: etching in diluted sodium hydroxide, E: exposed UV-lacquer is removed, F: etching in iron (III) chloride solution, G: removing lacquer with ethanol and drilling vias.

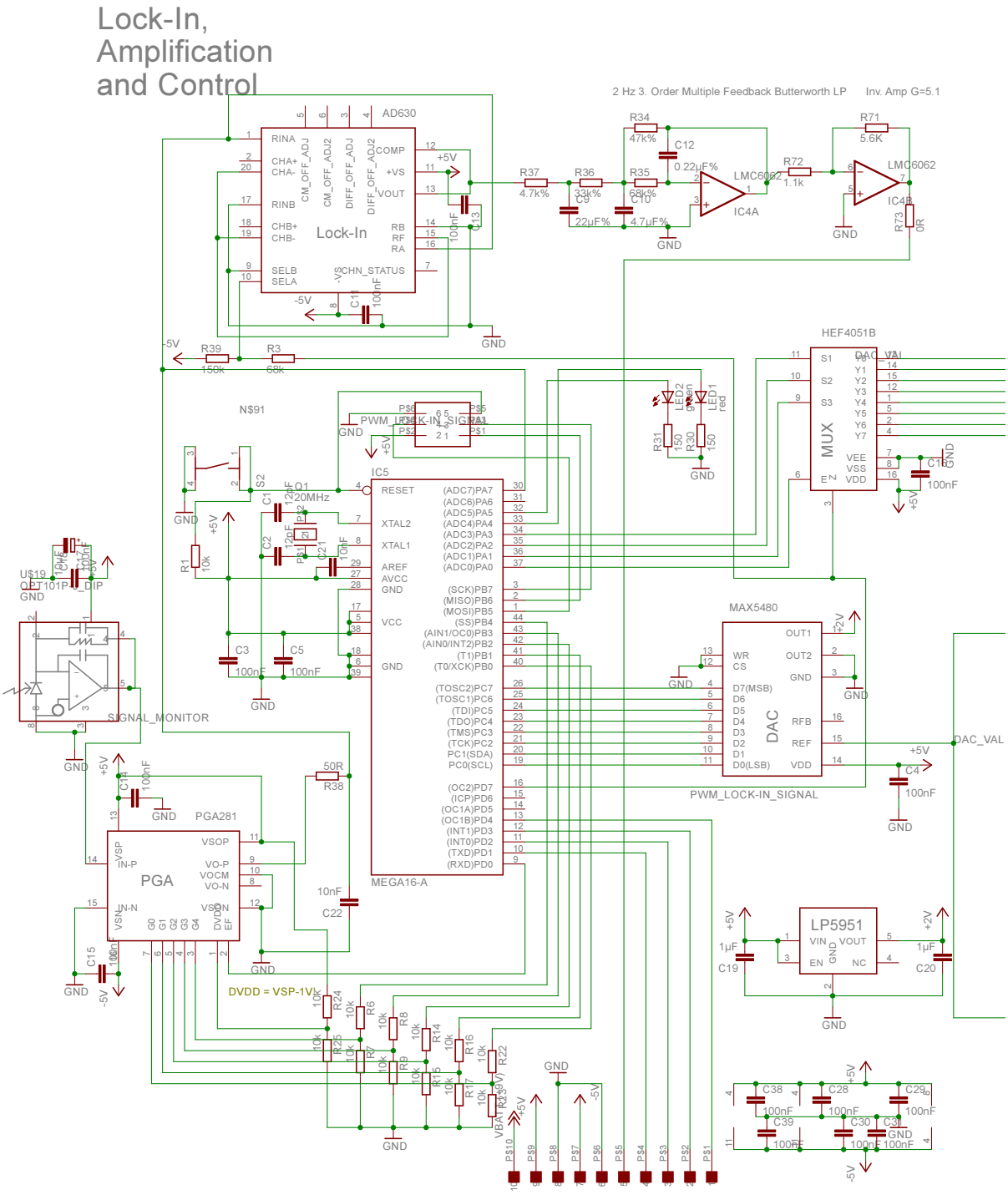

Figure A.3: fNIRS module full schematics part a.

Author	**>650**	**>675**	**>700**	**>725**	**>750**	**>775**	**>800**	**>825**	**>850**	**>875**	**>900**
Piper2013 [49]					760				850		
Safaie2013 [15]					760				850		
Kiguchi2012 [48]					754			830			
Chang2011 [56]				735					850		
Lareau2011 [38]				735					850		
Kanoh2009 [62]						780		830			
Zhang2009 [55]					760				850		
Bauernfeind2008 [50]	670									890	
Soraghan2008 [19]					760					880	
Kawaguchi2008		680						830			
Atsumori2007 [52]						790			850		
Coyle2007 [20]						760				880	
Chenier2007 [54]				730					850		
Bunce2006 [14]				730					850		
Bozkurt2005 [53]				730					850		
Vaithianathan2004 [58]						780				880	
Coyle2004 [18]			700							880	
Sato2004 [69]		680						830			
Strangman2003 [66]					760			830			
Rolfe2001 [51]						780			850		
Boas2001 [45]						785		830			
Yamashita2001 [68]	660							830			
Rolfe2000 [30]					775				850		
Siegel1999 [44]						780		830			
Benni1995 [32]						780		830			
Cope1991 [21]						778			867		
Okui2005 [70]		690	...	...	750			830			
Funane2009		690	...	...	..775			825..	...	...	900
Correia2010 [72]			704							887	
Yamashita2001 [68]	...	...	...	...	...	780		830			
OXYMON Mk III, Artinis					760				850		
PortaLite, Artinis					760				850		
fNIR1100, fNIR Devices				730					850		
ETG-4000, Hitachi		695							850		
ETG-7100, Hitachi		695							850		
WOT, Hitachi			705					830			
Genie, MRRA			700					830			
NIRScout(X), NIRx					760				850		
Brainsight NIRS, R. Research		685						830			
FOIRE-3000, Shimadzu						780		830			
OEG-SpO2, Spectratech					770			840			
CW6, TechEn		690						830			
UCL Optical Topography, UCL						780			850		
Imagent, ISS		690						830			
	>650	**>675**	**>700**	**>725**	**>750**	**>775**	**>800**	**>825**	**>850**	**>875**	**>900**

Table A.3: Overview of wavelength pairs and selection optimization in fNIRS systems.

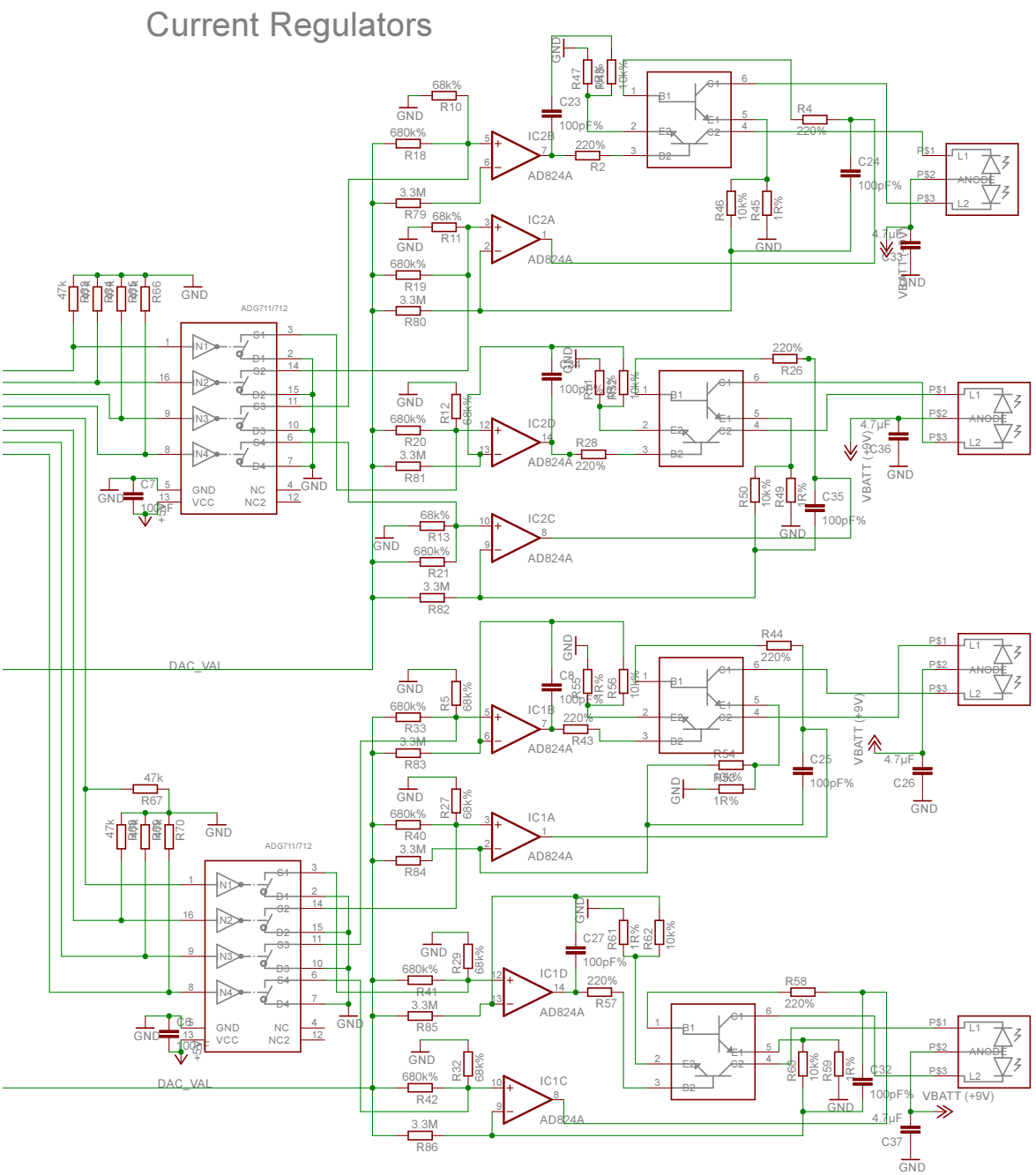

Figure A.4: fNIRS module full schematics part b.

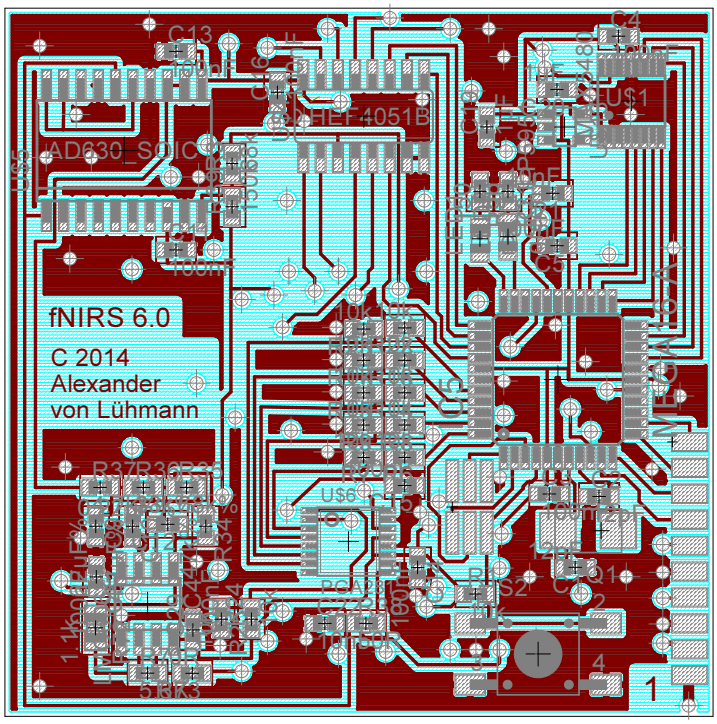

Figure A.5: fNIRS module layout, layers 1 & 2 (top).

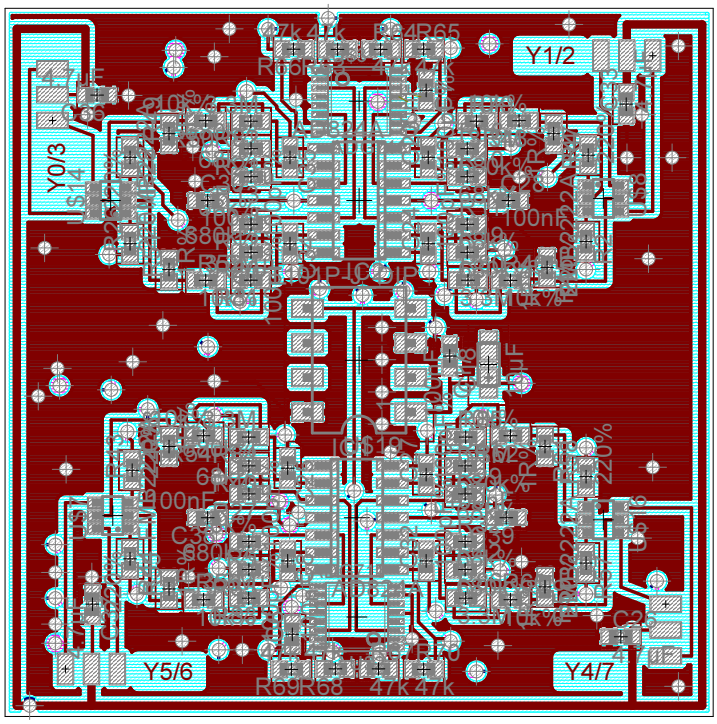

Figure A.6: fNIRS module layout, layers 3 & 4 (bottom).

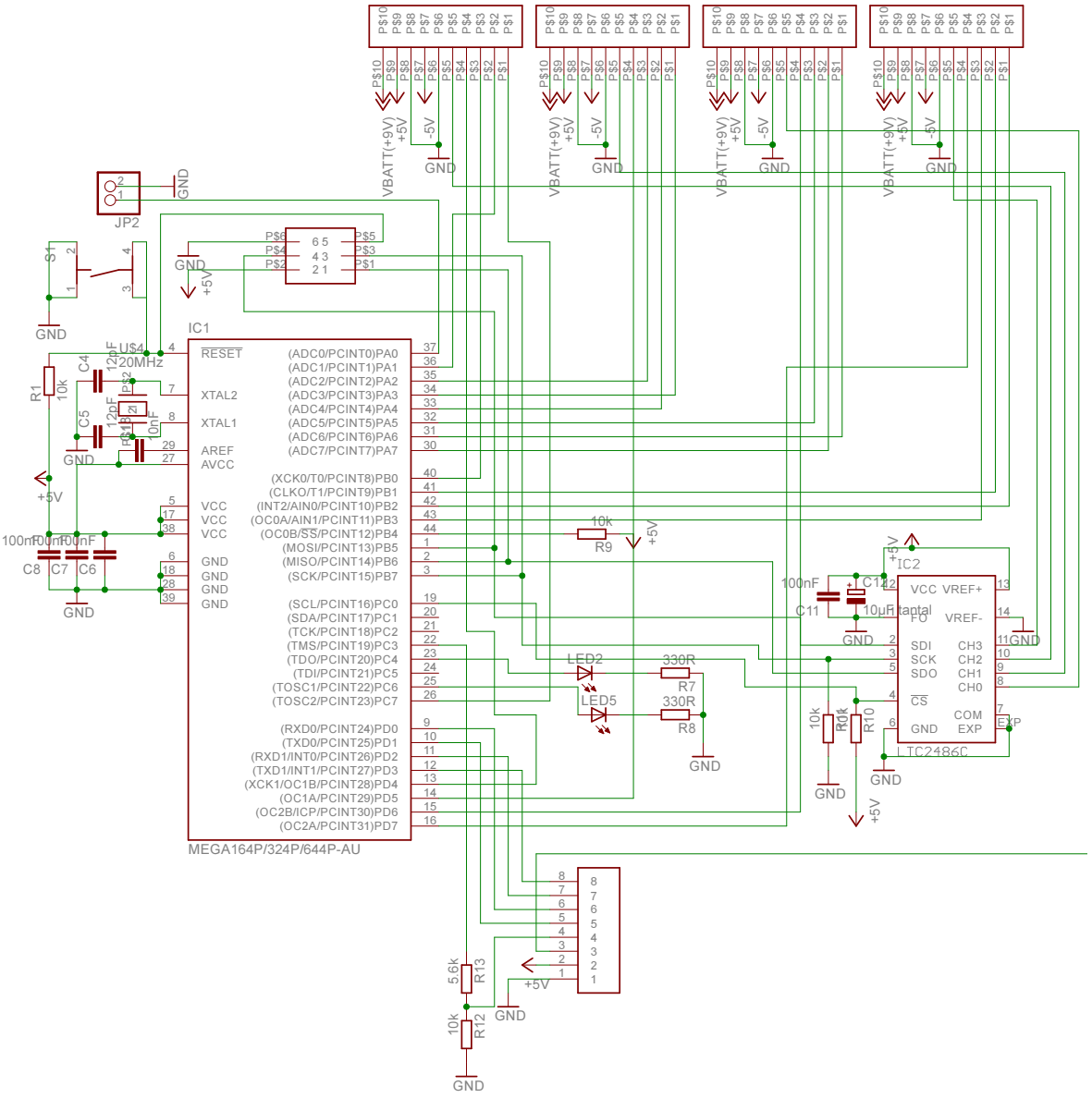

Figure A.7: fNIRS mainboard full schematics part a.

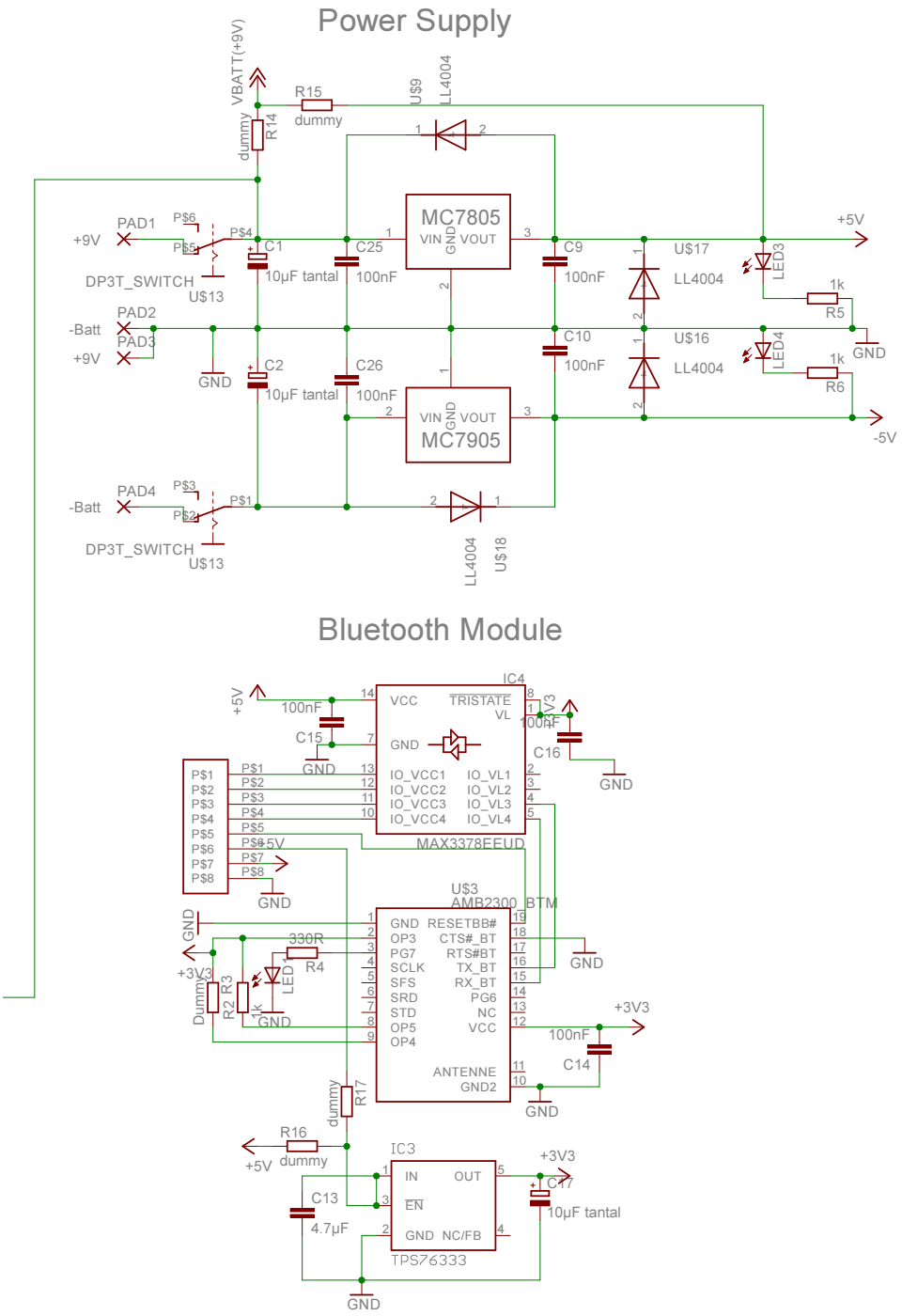

Figure A.8: fNIRS mainboard full schematics part b.

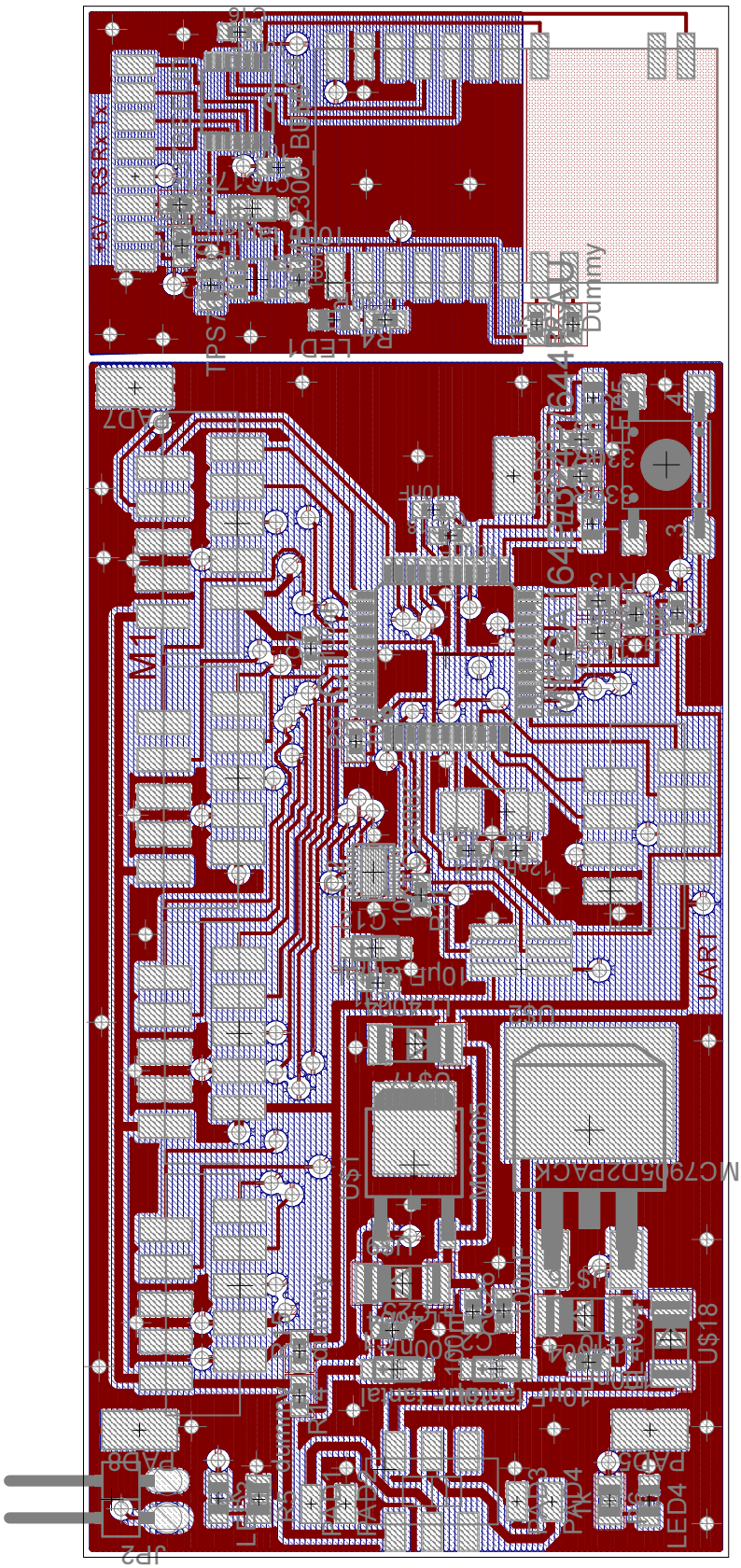

Figure A.9: fNIRS mainboard layout.

Model	Wave-lengths λ1	λ2	Max I_F [mA]		Max pulse I_p [mA]		Typ. Total rad. Power [mW]		Half width Δλ [nm]		View. Half angle [deg]	Type [mm]
L760/850-04A	760	850	100	100			15	18	30	35	+-20	5 Mold
L760/850-38	760	850	75	75			16	18	30	35	+-40	3 Mold
L770/840-40D59	770	840	100	100	500	500	12	9	28	32	+-55	4.65 Stem
SMT735/850	735	850	75	75	300	300	10	18	20	35	+-55	2.7 SMD
L750/850-04A	750	850	100	100			15	18	30	35	+-20	5 Mold
L760/840-05A	760	840	100	100			15	18	30	35	+-40	5.4 Stem
L760/850-05A	760	850	100	100			15	18	30	35	+-40	5.4 Mold

Figure A.10: Comparison of available LED alternatives.

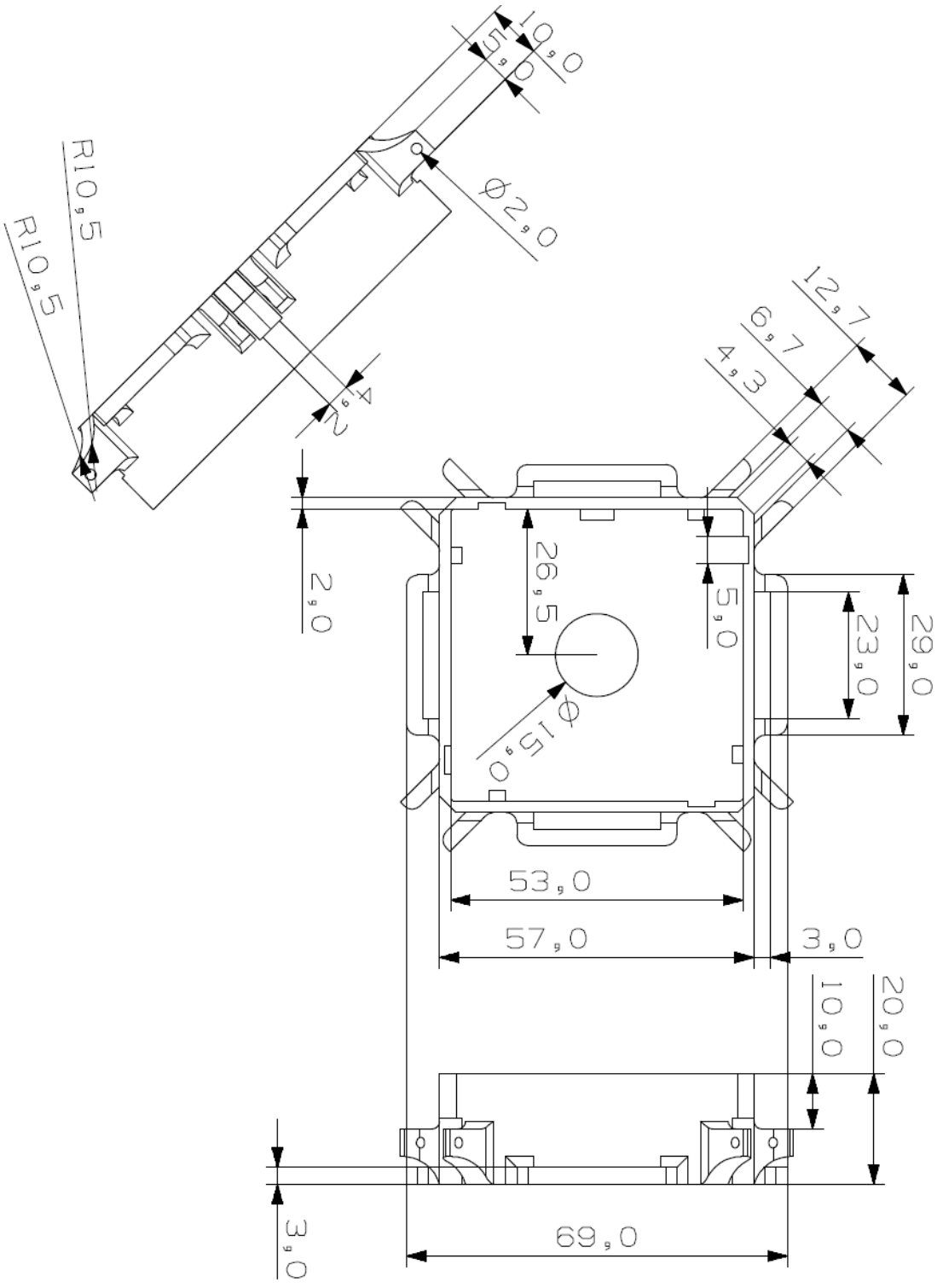

Figure A.11: Technical drawing NIRS module body housing. Units are [mm].

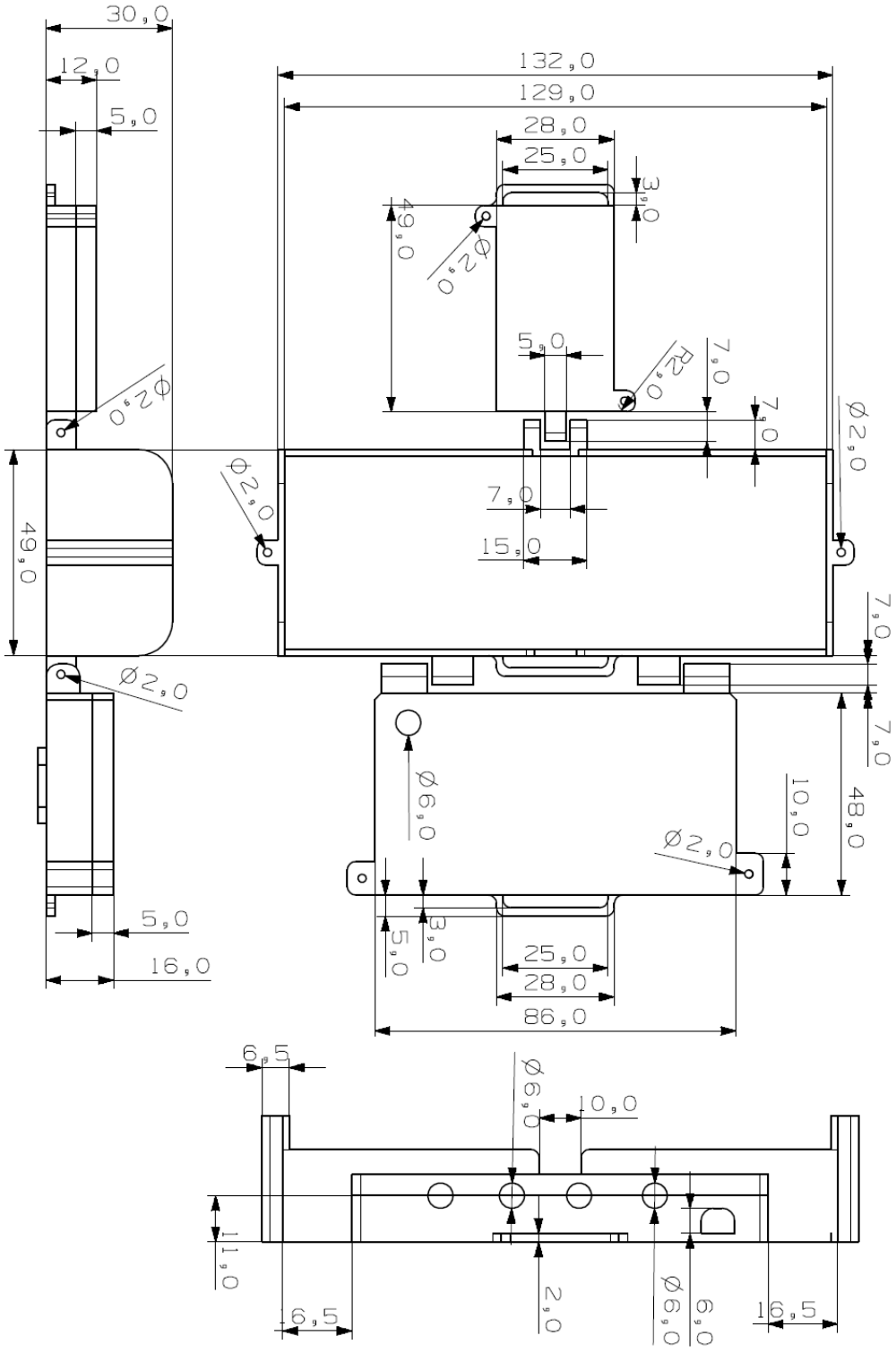

Figure A.12: Technical drawing NIRS mainboard body housings. Units are [mm].

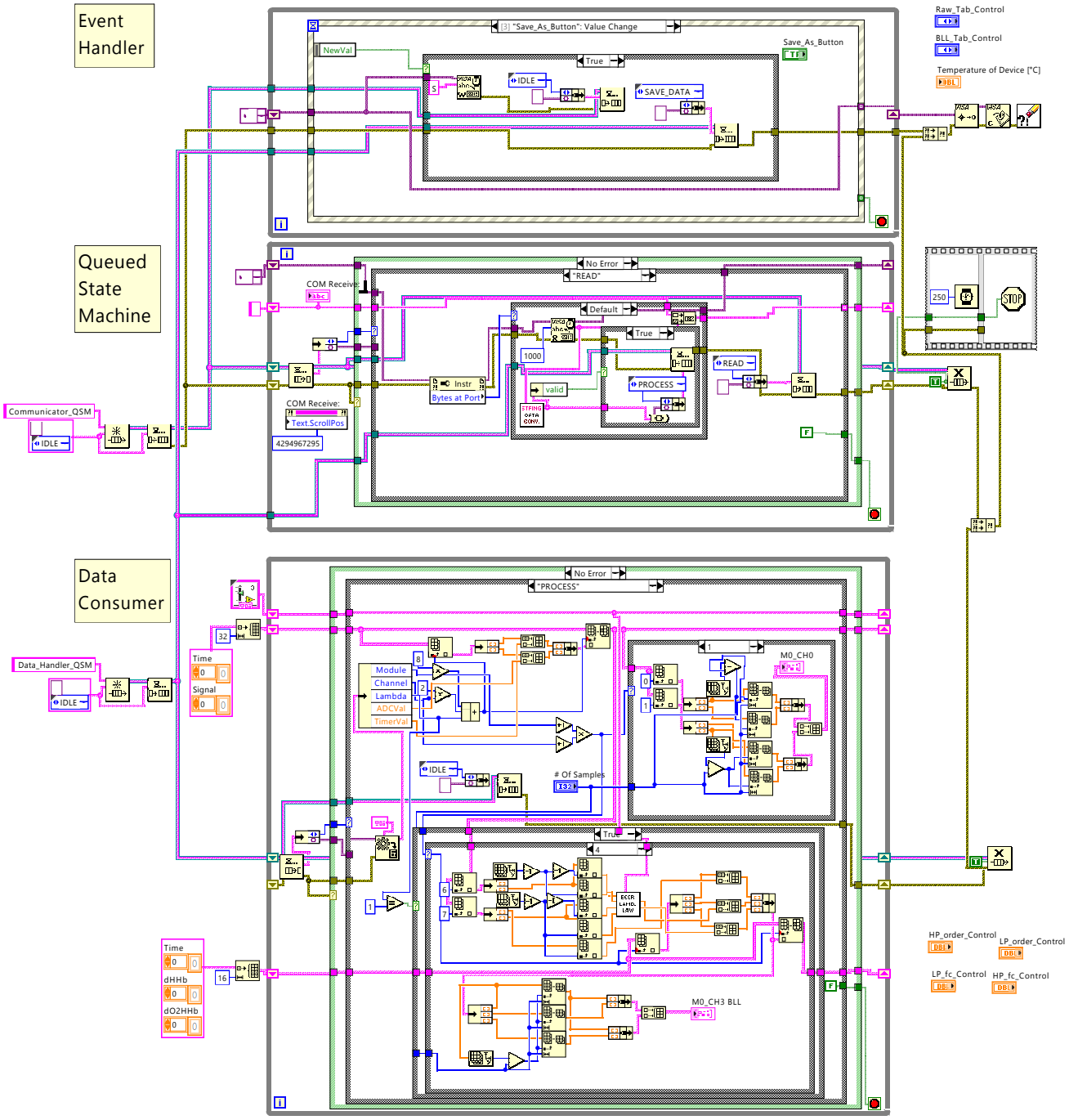

Figure A.13: LabView eQSM block diagram overview.

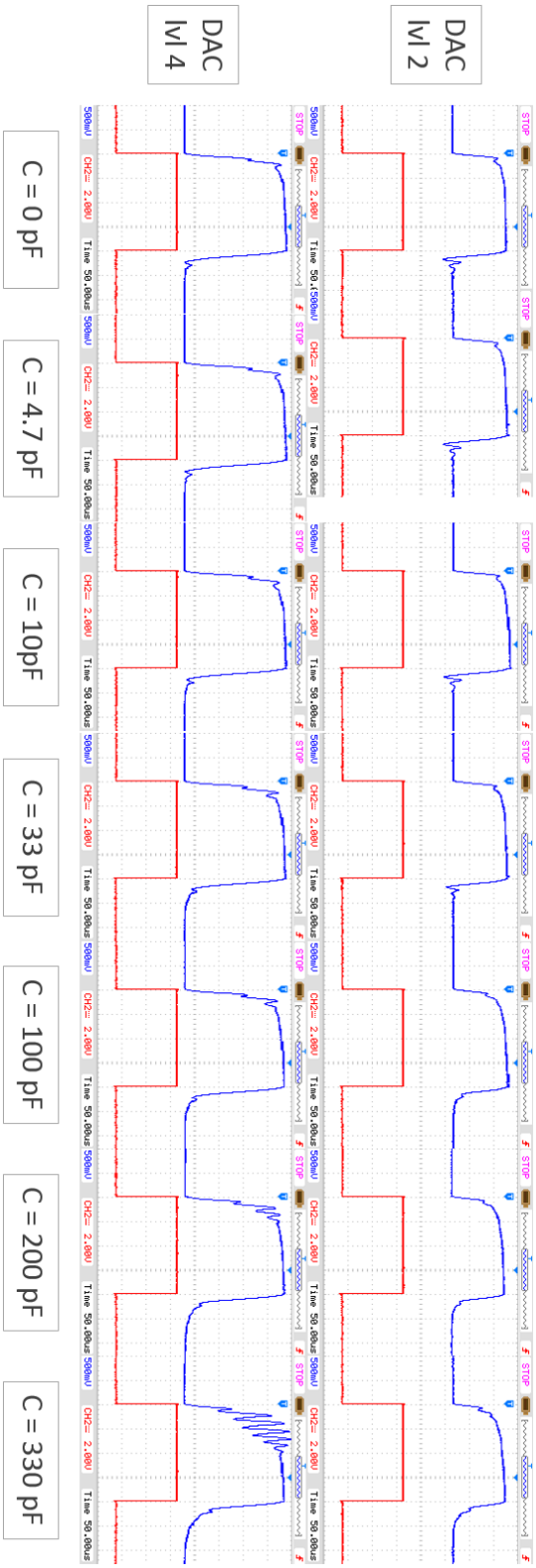

Figure A.14: Evaluation of optimal current regulator decoupling capacitor value.

List of Figures

List of Tables

References

[1] F. Jöbsis, "Noninvasive, infrared monitoring of cerebral and myocardial oxygen sufficiency and circulatory parameters.," *Science*, vol. 198 no. 4323, pp. 1264–1267, 1977.

[2] D. T. Delpy, M. Cope, P. van der Zee, S. Arridge, S. Wray, and J. Wyatt, "Estimation of optical pathlength through tissue from direct time of flight measurement," *Physics in Medicine and Biology*, vol. 33, no. 12, p. 1433, 1988.

[3] M. Cope and D. Delpy, "System for long-term measurement of cerebral blood and tissue oxygenation on newborn infants by near infra-red transillumination," *Medical and Biological Engineering and Computing*, vol. 26, no. 3, pp. 289–294, 1988.

[4] A. Edwards and J. W. W. Pogue, "Cotside measurement of cerebral blood frlow in ill newborn infants by near infrared spectroscopy.," *The Lancet*, vol. 2 (8614), pp. 770–771, 1988.

[5] J. Wyatt, Cope, and D. Delpy, "Quantification of ccerebral blood volume in human infants by near-infrared spectroscopy.," *J. Appl. Physiol.*, vol. 68 (3), pp. 1086–1091, 1990.

[6] M. Wolf, P. Evans, and H. Bucher, "Measurement of absolute cerebral haemoglobin concentration in adult and neonates.," *ADv. Exp. Med. Biol.*, vol. 428, pp. 219–227, 1997.

[7] B. Chance and Z. Zhuang, "Cognition-activated low-frequency modulation of light absorption in human brain.," *Proc. Natrl. Acad. Sci. USA*, vol. 90 (8), pp. 3770–3774, 1993.

[8] Y. Hoshi and M. Tamura, "Detection of dynamic changes in cerebral oxygenation coupled to neuronal funfunction during mental work in man.," *Neurosci. Lett.*, vol. 150 (1), pp. 5–8, 1993.

[9] T. Kato, A. Kamei, and S. Takashima, "Human visual cortical function during photic stimulation monitoring by means of near-infrared spectroscopy.," *J. Cereb. Blood Flow Metab.*, vol. 13 (3), pp. 516–520, 1993.

[10] A. Villringer, J. Planck, and J. Hock, "Near infrared spectroscopy (NIRS): a new tool to study hemodynamic changes during activation of brain function in human adult.," *Neurosci. Lett.*, vol. 154 (1-2), pp. 101–104, 1993.

[11] F. Scholkmann, S. Kleiser, A. J. Metz, R. Zimmermann, J. M. Pavia, U. Wolf, and M. Wolf, "A review on continuous wave functional near-infrared spectroscopy and imaging instrumentation and methodology," *NeuroImage*, no. 0, pp. –, 2013.

[12] I.-Y. Son and B. Yazici, *Near Infrared Imaging and Spectroscopy for Brain Activity Monitoring*, ch. Advances in Sensing with Security Applications, pp. 341–372. NATO Security through Science Series-A: Chemistry and Biology, Springer, 2006.

[13] G. Strangman, D. A. Boas, and J. P. Sutton, "Non-invasive neuroimaging using near-infrared light," *Biological Psychiatry*, vol. 52, no. 7, pp. 679 – 693, 2002.

[14] S. Bunce, M. Izzetoglu, K. Izzetoglu, B. Onaral, and K. Pourrezaei, "Functional near-infrared spectroscopy," *Engineering in Medicine and Biology Magazine, IEEE*, vol. 25, no. 4, pp. 54–62, 2006.

[15] J. Safaie, R. Grebe, H. A. Moghaddam, and F. Wallois, "Toward a fully integrated wireless wearable EEG-NIRS bimodal acquisition system," *Journal of Neural Engineering*, vol. 10, no. 5, p. 056001, 2013.

[16] G. Pfurtscheller, B. Z. Allison, G. Bauernfeind, C. Brunner, T. Solis Escalante, R. Scherer, T. O. Zander, G. Mueller-Putz, C. Neuper, and N. Birbaumer, "The hybrid BCI," *Frontiers in Neuroscience*, vol. 4, no. 3, 2010.

[17] K. Yanagisawa, K. Asaka, H. Sawai, H. Tsunashima, T. Nagaoka, T. Tsujii, and K. Sakatani, "Brain-computer interface using near-infrared spectroscopy for rehabilitation," in *Control Automation and Systems (ICCAS), 2010 International Conference on*, pp. 2248–2253, 2010.

[18] S. Coyle, T. Ward, and C. Markham, "Physiological noise in near-infrared spectroscopy: implications for optical brain computer interfacing," in *Engineering in Medicine and Biology Society, 2004. IEMBS '04. 26th Annual International Conference of the IEEE*, vol. 2, pp. 4540–4543, 2004.

[19] C. Soraghan, F. Matthews, C. Markham, B. Pearlmutter, R. O'Neill, and T. Ward, "A 12-Channel, real-time near-infrared spectroscopy instrument for brain-computer interface applications," in *Engineering in Medicine and Biology Society, 2008. EMBS 2008. 30th Annual International Conference of the IEEE*, pp. 5648–5651, 2008.

[20] S. Coyle, T. Ward, and C. Markham, "Brain-computer interface using a simplified functional near-infrared spectroscopy system.," *J Neural Eng.*, vol. 4(3), pp. 219–226, 2007.

[21] M. Cope, *The application of near infrared spectroscopy to non invasive monitoring of cerebral oxygenation in the newborn infant.* PhD thesis, Department of Medical Physics and Bioengineering, University College London, 1991.

[22] M. Cutler, "Transillumination as an aid in the diagnosis of breast lesions.," *Surg. Gynecol. Obstet.*, vol. 48, pp. 721–729, 1929.

[23] T. Curling, W. Gobrecht, and P. Goddard, *A Practical Treatise on the Diseases of the Testis, and of the Spermatic Cord and Scrotum.* https://archive.org/details/101504825.nlm.nih.gov: Blanchard and Lea, Philadelphia, 1856.

[24] A. Beer, "Bestimmung der Absorption des rothen Lichts in farbigen Flüssigkeiten," *Annalen der Physik*, vol. 162, pp. 78–88, 1852.

[25] K. Matthes and F. Gross, "Fortlaufende Registrierung der Lichtabsorption des Blutes in zwei verschiedenen Spektralbezirken.," *Naunyn-Schmiedeberg's Archives of Pharmacology*, vol. 191, pp. 381–390, 1938.

[26] K. Matthes and F. Gross, "Untersuchung Ãijber die Absorption von rotem und ultrarotem Licht durch kohlenoxygesÃd'ttigtes, sauerstoffgesÃd'ttigtes und reduziertes Blut.," *Naunyn-Schmiedeberg's Archives of Pharmacology*, vol. 191, pp. 369–380, 1938.

[27] K. Matthes and F. Gross, "Zur Methode der fortlaufende Registrierung der Farbe des menschlichen Blutes.," *Naunyn-Schmiedeberg's Archives of Pharmacology*, vol. 191, pp. 523–528, 1938.

[28] E. Merrick and T. Hayes, "Continuous non-invasive measurements of arterial oxgen levels.," *Hewlett-Packard J.*, vol. 28, pp. 2–9, 1976.
[29] T. Aoyagi, T. Kishi, K. Yamaguchi, and S. Watanabe, "Improvement of ear-piece oximeter," *Proc. Jpn. Med. Elect. Biol. Eng. Conf.*, vol. 13th, p. 90, 1974.
[30] P. Rolfe, "In Vivo Near Infra-Red Spectrophotometry," *Annual Review in Biomedical Engineering*, vol. 2, pp. 315–354, 2000.
[31] E. Okada, M. Firbank, M. Schweiger, S. Arridge, M. Cope, and D. Delpy, "Theoretical and experimental investigation of near-infrared light propagation in a model of the adult head," *Applie*, vol. 36, Issue 1, pp. 21–31, 1997.
[32] P. Benni, B. Chen, D. Amory, and J. K. J. Li, "A novel near-infrared spectroscopy (NIRS) system for measuring regional oxygen saturation," in *Bioengineering Conference, 1995., Proceedings of the 1995 IEEE 21st Annual Northeast*, pp. 105–107, 1995.
[33] M. W. W. Wolf and V. Toronov, "Different time evolution of oxyhemoglobin and deoxyhemoglobin concentration changes in visual and motor cortices during functional stimulation: a near-infrared spectroscopy study.," *Neuoimage*, vol. 16, pp. 704–712, 2002.
[34] P. Fox and M. Raichle, "Focal physiological uncoupling of cerebral blood low and oxidative metabolism during somatosensory stimulation in human subjects.," *Proc. Natrl. Acad. Sci. USA*, vol. 83, pp. 1140–1144, 1986.
[35] H. Obrig and A. Villringer, "Beyond the visible - imaging the human brain with light," *Journal of Cerebral Blood Flow and Metabolism*, vol. 12, pp. 1–18, 2003.
[36] G. Strangman, G. Culver, J. Thompson, and D. Boas, "A quantitative comparison of simultaneous bold fmri and nirs recordings during functional brain activation.," *Neuroimage*, vol. 17, pp. 719–731, 2002.
[37] G. Gratton, M. Fabiani, T. Elbert, and B. Rockstroh, "Seeing right through you: Applications of optical imaging to the study of the human brain.," *Psychophysiology*, vol. 40 (4), pp. 487–491, 2003.
[38] E. Lareau, G. Simard, F. Lesage, D. Nguyen, and M. Sawan, "Near infrared spectrometer combined with multichannel EEG for functional brain imaging," in *Medical Information Communication Technology (ISMICT), 2011 5th International Symposium on*, pp. 122–126, 2011.
[39] C. Elwell, R. Springett, and E. Hillman, "Oscillations in cerebral haemodynamics - implications for functional activation studies.," *Adv. Exp. Med. Biol.*, vol. 471, pp. 57–65, 1999.
[40] Y. Zhang, M. A. Franceschini, D. A. Boas, and D. H. Brooks, "Eigenvector-based spatial filtering for reduction of physiological interference in diffuse optical imaging," *Journal of Biomedical Optics*, vol. 10, no. 1, pp. 011014–011014–11, 2005.
[41] K. Izzetoglu, S. Bunce, M. Izzetoglu, B. Onaral, and K. Pourrezaei, "Functional near-infrared neuroimaging," in *Engineering in Medicine and Biology Society, 2004. IEMBS '04. 26th Annual International Conference of the IEEE*, vol. 2, pp. 5333–5336, 2004.
[42] H. Ayaz, M. Izzetoglu, P. Shewokis, and B. Onaral, "Sliding-window motion artifact rejection for Functional Near-Infrared Spectroscopy," in *Engineering in Medicine and Biology Society (EMBC), 2010 Annual International Conference of the IEEE*, pp. 6567–6570, 2010.
[43] E. Gratton, W. Mantulin, M. vandeVen, J. Fishkin, M. Maris, and B. Chance, "The possibility of a near-infrared optical imaging system using frequency-domain

methods.," in *Proceedings of the 3rd International Converence on Peace through Mind/Brain Science*, pp. 183–189, 1990.

[44] A. Siegel, J. Marota, and D. Boas, "Design and evaluation of a continuous-wave diffuse optical tomography system," *Optics Express*, vol. 4, pp. 287–298, 1999.

[45] D. A. Boas, T. Gaudette, G. Strangman, X. Cheng, J. J. Marota, and J. B. Mandeville, "The Accuracy of Near Infrared Spectroscopy and Imaging during Focal Changes in Cerebral Hemodynamics," *NeuroImage*, vol. 13, no. 1, pp. 76 – 90, 2001.

[46] A. Duncan, J. H. Meek, M. Clemence, C. E. Elwell, L. Tyszczuk, M. Cope, and D. T. Delpy, "Optical pathlength measurements on adult head, calf and forearm and the head of the newborn infant using phase resolved optical spectroscopy," *Physics in Medicine and Biology*, vol. 40, pp. 295–304, 1995.

[47] M. Essenpreis, C. Elwell, M. Cope, P. Van der Zee, S. Arridge, and D. Delpy, "Spectral dependence of temporal point spread functions in human tissues," *Applied Optics*, vol. 32, no. 4, pp. 418–425, 1993.

[48] M. Kiguchi, H. Atsumori, I. Fukasaku, Y. Kumagai, T. Funane, A. Maki, Y. Kasai, and A. Ninomiya, "Note: Wearable near-infrared spectroscopy imager for haired region," *Review of Scientific Instruments*, vol. 83, p. 056101, 2012.

[49] S. K. Piper, A. Krueger, S. P. Koch, J. Mehnert, C. Habermehl, J. Steinbrink, H. Obrig, and C. H. Schmitz, "A wearable multi-channel fNIRS system for brain imaging in freely moving subjects," *NeuroImage*, no. 0, pp. –, 2013.

[50] G. Bauernfeind, R. Leeb, S. C. Wriessnegger, and G. Pfurtscheller, "Development, set-up and first results for a one-channel near-infrared spectroscopy system," *Biomed Tech*, vol. 53, pp. 36–43, 2008.

[51] P. Rolfe, G. Mondo, F. Bottini, D. Repetto, and C. Ruggiero, "Near infra-red spectroscopy: a low cost device," in *Engineering in Medicine and Biology Society, 2001. Proceedings of the 23rd Annual International Conference of the IEEE*, vol. 3, pp. 3147–3149 vol.3, 2001.

[52] H. Atsumori, M. Kiguchi, A. Obata, H. Sato, T. Katura, K. Utsugi, T. Funane, and A. Maki, "Development of a Multi-channel, Portable Optical Topography System," in *Engineering in Medicine and Biology Society, 2007. EMBS 2007. 29th Annual International Conference of the IEEE*, pp. 3362–3364, 2007.

[53] A. Bozkurt, A. Rosen, H. Rosen, and B. Onaral, "A portable near infrared spectroscopy system for bedside monitoring of newborn brain," *BioMedical Engineering OnLine*, vol. 4, no. 1, p. 29, 2005.

[54] F. Chenier and M. Sawan, "A New Brain Imaging Device Based on fNIRS," in *Biomedical Circuits and Systems Conference, 2007. BIOCAS 2007. IEEE*, pp. 1–4, 2007.

[55] Y. Zhang, J. Sun, G. Wei, F. Scopesi, G. Serra, and P. Rolfe, "Design of a Portable Near Infra-Red Spectroscopy System for Tissue Oxygenation Measurement," in *Bioinformatics and Biomedical Engineering , 2009. ICBBE 2009. 3rd International Conference on*, pp. 1–4, 2009.

[56] M.-H. Chang, C.-L. Cheng, H.-M. Huang, J.-R. Kuo, and B.-S. Lin, "Wireless multi-channel near-infrared spectroscopy for monitoring middle cerebral artery occlusion," in *System Integration (SII), 2011 IEEE/SICE International Symposium on*, pp. 1072–1077, 2011.

[57] A. Bozkurt and B. Onaral, "Safety assessment of near infrared light emitting diodes for diffuse optical measurements," *BioMedical Engineering OnLine*, vol. 3:9, 2004.

[58] T. Vaithianathan, I. D. C. Tullis, N. Everdell, T. Leung, and A. Gibson, "Design of a portable near infrared system for topographic imaging of the brain in babies," *Review of Scientific Instruments*, vol. 75, pp. 3276–3283, 2004.

[59] E. R. Rajkumar, J. Safaie, R. Gupta, D. Pattnaik, H. AbrishamiMoghaddam, R. Grebe, and F. Wallois, "Development of an autonomic portable single-board computer based high resolution NIRS device for microcirculation analysis," in *Engineering in Medicine and Biology Society (EMBC), 2012 Annual International Conference of the IEEE*, pp. 3235–3238, 2012.

[60] K. Izzetoglu, S. Bunce, M. Izzetoglu, B. Onaral, and K. Pourrezaei, "fNIR spectroscopy as a measure of cognitive task load," in *Engineering in Medicine and Biology Society, 2003. Proceedings of the 25th Annual International Conference of the IEEE*, vol. 4, pp. 3431–3434 Vol.4, 2003.

[61] S. Coyle, T. Ward, C. Markham, and G. McDarby, "On the suitability of near-infrared systems for next generation brain computer interfaces.," *Physiol. Meas.*, vol. 25, pp. 815–822, 2004.

[62] S. Kanoh, Y.-m. Murayama, K.-I. Miyamoto, T. Yoshinobu, and R. Kawashima, "A NIRS-based brain-computer interface system during motor imagery: System development and online feedback training," in *Engineering in Medicine and Biology Society, 2009. EMBC 2009. Annual International Conference of the IEEE*, pp. 594–597, 2009.

[63] T. Ito, T. Hirano, Y. Mitsui, H. Akiyama, S. Ohgi, and C. Mizuike, "Design of brain machine interface using portable Near-InfraRed Spectroscopy," in *Micro-NanoMechatronics and Human Science (MHS), 2012 International Symposium on*, pp. 415–420, 2012.

[64] B. Z. Allison, R. Leeb, C. Brunner, G. R. MÃČÂijller-Putz, G. Bauernfeind, J. W. Kelly, and C. Neuper, "Toward smarter BCIs: extending BCIs through hybridization and intelligent control," *Journal of Neural Engineering*, vol. 9, no. 1, p. 013001, 2012.

[65] N. Birbaumer, "Breaking the silence: brain-computer interfaces (BCI) for communication and motor control.," *Psychophyiology*, vol. 43(6), pp. 517–32, 2006.

[66] G. Strangman, M. A. Franceschini, and D. A. Boas, "Factors affecting the accuracy of near-infrared spectroscopy concentration calculations for focal changes in oxygenation parameters," *NeuroImage*, vol. 18, no. 4, pp. 865 – 879, 2003.

[67] D. A. Boas, A. M. Dale, and M. A. Franceschini, "Diffuse optical imaging of brain activation: approaches to optimizing image sensitivity, resolution, and accuracy," *NeuroImage*, vol. 23, Supplement 1, no. 0, pp. S275 – S288, 2004. <ce:title>Mathematics in Brain Imaging</ce:title>.

[68] Y. Yamashita, A. Maki, and H. Koizumi, "Wavelength dependence of the precision of noninvasive optical measurement of oxy-, deoxy-, and total-hemoglobin," *Medical Physics*, vol. 28, pp. 1108–14, 2001.

[69] H. Sato, M. Kiguchi, and F. Kawaguchi, "Practicality of wavelength selection to improve signal-to-noise ratio in near-infrared spectroscopy.," *Neuroimage*, vol. 21 (4), pp. 1544–1562, 2004.

[70] N. Okui and E. Okada, "Wavelength dependence of crosstalk in dual-wavelength measurement of oxy- and deoxy-hemoglobin," *Journal of Biomedical Optics*, vol. 10, pp. 011015–1–0111015–8, 2005.

[71] K. Uludag, J. Steinbring, A. Villringer, and H. Obrig, "Separability and cross talk: optimizing dual wavelength combinations for near-infrared spectroscopy of the adult head," *Neuroimage*, vol. 22, pp. 583–9, 2004.

[72] T. Correia and A. G. G. Hebden, "Identification of the optimal wavelengths for optical topography: a photon measurement density function analysis.," *J Biomed. Opt.*, vol. 15 (5), p. 056002, 2010.
[73] M. L. Meade, *Lock-in amplifiers: principles and applications*. Peter Peregrinus Ltd., London UK, 1983.
[74] M. L. Meade, "Advances in lock-in amplifiers," *Journal of Physics E: Scientific Instruments*, vol. 15, no. 4, p. 395, 1982.
[75] D. Blair and P. Sydenham, "Phase sensitive detection as a means to recover signals buried in noise," *Journal of Physics E: Scientific Instruments*, vol. 8, no. 8, p. 621, 1975.
[76] S. K. Sengupta, J. M. Farnham, and J. E. Whitten, "A simple low-cost lock-in amplifier for the laboratory," *Journal of chemical education*, vol. 82, no. 9, p. 1399, 2005.
[77] S. Salvatori and M. Girolami, "Compact, four-quadrant lock-in amplifier generates two analog outputs," *DesignIdeas*, vol. 45, pp. 45–46, 2009.
[78] microcontroller.net, "Quarze und avr." http://www.mikrocontroller.net/articles/, December 2013.
[79] P. Fleury, "Avr-gcc uart library." http://homepage.hispeed.ch/peterfleury/avr-software.html, January 2014.
[80] T. D. C. for Life Science, "Bodyparts3d." http://dbarchive.biosciencedbc.jp/, September 2011.